

January 2012

# Surface Mass Transfer in Large Eddy Simulation (LES) of Langmuir Turbulence

Cigdem Akan

University of South Florida, [cakan@mail.usf.edu](mailto:cakan@mail.usf.edu)

Follow this and additional works at: <http://scholarcommons.usf.edu/etd>

 Part of the [American Studies Commons](#), [Environmental Engineering Commons](#), and the [Oceanography Commons](#)

---

## Scholar Commons Citation

Akan, Cigdem, "Surface Mass Transfer in Large Eddy Simulation (LES) of Langmuir Turbulence" (2012). *Graduate Theses and Dissertations*.

<http://scholarcommons.usf.edu/etd/3944>

This Dissertation is brought to you for free and open access by the Graduate School at Scholar Commons. It has been accepted for inclusion in Graduate Theses and Dissertations by an authorized administrator of Scholar Commons. For more information, please contact [scholarcommons@usf.edu](mailto:scholarcommons@usf.edu).

Surface Mass Transfer in Large Eddy Simulation (LES) of Langmuir Turbulence

by

Cigdem Akan

A dissertation submitted in partial fulfillment  
of the requirements for the degree of  
Doctor of Philosophy  
Department of Civil & Environmental Engineering  
College of Engineering  
University of South Florida

Major Professor: Andrés E. Tejada-Martínez, Ph.D.  
Jeffrey A. Cunningham, Ph.D.  
Boris Galperin, Ph.D.  
Muhammad M. Rahman, Ph.D.  
Daniel C. Simkins, Jr., Ph.D.

Date of Approval:  
May 3, 2012

Keywords: Langmuir circulation, surface renewal theory, Stokes drift velocity, mass flux,  
numerical simulation

Copyright © 2012, Cigdem Akan

## **Dedication**

I dedicate my dissertation work to my family and many friends. A special feeling of gratitude to my loving parents, Murat and Günser Akan. It is their encouragement and support from the very beginning of my life that made it possible for me to reach this stage. My wonderful brother Bilhan Bilge Akan, thank you for always supporting me, you are very special. I could not have done it without you.

I also dedicate this work and give special thanks to my friend Hale Altunbilek who was my roommate for two of my years here. Thank you for always believing in me. You have been my best friend and cheerleader.

I would like to offer special thanks my friends at Istanbul Technical University who have supported me throughout the process even though they are thousands of miles away: Sevil Deniz Yakan-Doruk, Deniz Bayraktar-Ersan, Emre Peşman and Burak Karacık. I love you and will always appreciate all you have done.

I am also grateful to Mario Juha, Paola Guzman, Seçkin & Pavla Özkul who have been my very close friends throughout my doctorate program. Thanks a lot for everything.

## **Acknowledgments**

First and foremost I want to thank my advisor Dr. Andrés E. Tejada-Martínez. It has been a honor to be his first Ph.D. student. Throughout my doctorate program, he provided encouragement, sound advice, good teaching, and lots of good ideas. The joy and enthusiasm he has for his research was contagious and motivational for me, even during tough times in the Ph.D. pursuit. In every sense, none of this work would have been possible without him.

I am also very grateful to my committee members: Dr. Jeffrey A. Cunningham, Dr. Boris Galperin, Prof. Muhammad M. Rahman, & Dr. Daniel C. Simkins, Jr. for their time, interest, helpful comments and insightful questions.

I would also like to sincerely thank to Dr. Safak Nur Erturk-Bozkurtoglu for her assistance and guidance in getting my graduate career started on the right foot.

It was a pleasure to share doctoral studies with wonderful people in our Environmental Computational Fluid Dynamics group like Nityanand Sinha, Roozbeh Golshan, Rachel Walker and Jie Zhang.

I gratefully acknowledge the funding sources that made my Ph.D. work possible. I was funded by my advisor's grant from National Science Foundation. I was also partially supported by Department of Civil & Environmental Engineering by a teaching assistant position for my first two years.

Special thanks are also given to rest of my friends and colleagues especially Semiha Çalışkan, Derviş Emre Demirocak and Onursal Önen at University of South Florida for their positive support.

## Table of Contents

List of Tables	iv
List of Figures	v
List of Symbols	ix
Abstract	xiii
Chapter 1: Introduction	1
1.1 Context and Motivation	1
1.2 Objectives	8
1.3 Organization of the Dissertation	13
Chapter 2: Literature Review	15
2.1 Turbulence	15
2.1.1 Physical Description of Turbulence	16
2.1.2 Mathematical Description of Turbulence	18
2.1.3 Numerical Approach to Turbulence	19
2.1.3.1 Scales of Turbulence	19
2.1.3.2 Direct Numerical Simulation (DNS)	21
2.1.3.3 Reynolds-Averaged Navier-Stokes Simulation	23
2.1.3.4 Large Eddy Simulation (LES)	25
2.2 Turbulence in the Upper Ocean	30
2.3 Chapter Summary	33
Chapter 3: Boundary Exchange at the Interface	34
3.1 Stagnant Film Model	34
3.2 Exchange into a Turbulent Water Body	36
3.3 Mass Transfer and Turbulence	37
3.3.1 Review of Mass Transfer Computation	38
3.3.2 Review of Mass Transfer Theories	39
3.4 Chapter Summary	43
Chapter 4: Turbulent Mass Transport: Computational Methodology	44
4.1 Governing LES Equations	44
4.1.1 Time Filtered N-S Equations (C-L Equations)	45
4.1.2 Spatially Filtered (LES) Equations	47
4.2 Subgrid Scale (SGS) Modeling	47

4.2.1	SGS Stress for Momentum Equation	47
4.2.2	SGS Flux for Scalar Equation	49
4.3	Geometry of the Flows	50
4.4	Chapter Summary	53
Chapter 5:	LC Structure and Turbulence Statistics of the Velocity Field	54
5.1	LC Structure	54
5.2	Mean Profiles	60
5.2.1	Budgets of $\langle \bar{u}'_i \bar{u}'_i \rangle$	64
5.3	Chapter Summary	67
Chapter 6:	Scalar Transport	69
6.1	LC Structure and Scalar Transport	69
6.2	Near Surface Scalar Transport	74
6.3	Mean Scalar Concentration and Transfer Velocity	81
6.3.1	Bulk concentration	81
6.4	Chapter Summary	88
Chapter 7:	Mass Transfer Through Air-Water Interfaces	91
7.1	Surface Renewal Theory	91
7.1.1	Stokes Drift Shear Model	93
7.1.2	Large Eddy Model	94
7.1.3	Small Eddy Model	99
7.1.4	Surface Divergence Model	102
7.1.5	Errors	105
7.2	Chapter Summary	106
Chapter 8:	Conclusions	108
8.1	Future Work	112
References		114
Appendices		123
Appendix A:	Numerical Method	124
A.1	Temporal Discretization	124
A.1.1	Momentum Equation	124
A.1.2	Scalar Equation	127
A.2	Spatial Discretization	127
A.3	Grid Stretching	129
A.4	Accuracy of the Numerical Method	131
Appendix B:	Momentum and Scalar Balances	136
B.1	Momentum Balance	136
B.2	Scalar Balance	140
Appendix C:	Resolved Turbulent Kinetic Energy	144
Appendix D:	Budgets of $\langle \bar{C}'^2 \rangle$	145
Appendix E:	Budgets of $\langle \bar{C}' u'_3 \rangle$	149

Appendix F: Schmidt Number Dependence	154
Appendix G: Reynolds Number Dependence	157
Appendix H: Rights and Permissions	160
H.1 Permissions to Use the Figures in Chapter 1	160
H.1.1 Permission to Use Figure 1.2	160
H.1.2 Permission to Use Figure 1.4	164
H.2 Permissions to Use the Figures in Chapter 2	170
H.2.1 Permission to Use Figure 2.1	170
H.2.2 Permission to Use Figure 2.2	173
H.2.3 Permission to Use Figure 2.3	174
H.3 Permission to Use the Figure in Chapter 3	177
H.3.1 Permission to Use Figure 3.1	177
H.4 Permissions to Use the Figures in Appendix A	178
H.4.1 Permission to Use Figure A.1	178
H.4.2 Permission to Use Figure A.2	183



## List of Tables

Table 4.1:	Variables obtained from field measurements (See [28]).	52
Table 6.1:	Comparison of $K_{LES}$ , $C_{\text{bulk}}$ , $\Delta C$ and vertical gradient of concentration at the surface for all flows; $C_{\text{bulk}}$ is the mean concentration at the shallowest depth of the bulk region based on the definitions described earlier.	84
Table 6.2:	Comparison of $K_{LES}$ , $C_{\text{bulk}}$ , $\Delta C$ and vertical gradient of concentration at the surface for all flows; $C_{\text{bulk}}$ is the mean concentration at the middle of the water column.	84
Table 7.1:	Comparison of values of maximum dimensionless partially averaged vertical velocity fluctuations and $F_r$ for different flows.	97
Table 7.2:	Comparison of values of dimensionless turbulent kinetic energy dissipation, $\varepsilon$ for different flows.	101
Table 7.3:	Values of surface divergence at the surface for different flows.	104
Table C.1:	Budgets of turbulent kinetic energy	144
Table D.1:	Budgets of $\langle \bar{C}'\bar{C}' \rangle$	145
Table E.1:	Budgets of $\langle \bar{C}'\bar{u}'_3 \rangle$	149
Table G.1:	Comparison of $K_{LES}$ , $C_{\text{bulk}}$ , $\Delta C$ and vertical gradient of concentration at the surface for in flows with and without LC at different Reynolds numbers scaled by $C_{\text{ref}}$ .	158

## List of Figures

Figure 1.1:	Schematic of the mass concentration diffusion sublayer at the surface of a water body where $\delta_c$ denotes thickness of the concentration boundary layer and $C$ denotes the mean concentration.	2
Figure 1.2:	Climatological mean annual sea-air CO <sub>2</sub> flux ( $g-Cm^{-2} yr^{-1}$ ) for the reference year 2000 (non-ElNino conditions). [84]	3
Figure 1.3:	Sketch showing the cellular structure of Langmuir circulation (LC) characterizing the turbulence advected by the wind-driven mean flow.	9
Figure 1.4:	Airborne infrared imagery over Tampa Bay. [57]	10
Figure 2.1:	Structures in a turbulent flow. [17]	17
Figure 2.2:	Comparison of DNS, LES and RANSS of an interfacial flow. [71]	25
Figure 2.3:	Sketch of function $f(x)$ and its filtered component $\bar{f}(x)$ where the filter width is $\Delta_f$ . [85]	26
Figure 2.4:	A depiction of the observed energy cascade.	28
Figure 2.5:	Schematized Langmuir circulation patterns.	31
Figure 3.1:	Schematic for the boundary exchange for a dissolving substance into a stagnant water body. [81]	35
Figure 4.1:	Model domain.	50
Figure 4.2:	(a) Stokes drift velocity and (b) Stokes drift velocity shear.	52
Figure 5.1:	Turbulent velocity at a point in a statistically steady flow.	55
Figure 5.2:	Color maps of partially averaged fluctuating velocity components on the $(x_2, x_3)$ - plane for wind driven flow with LC ( $La_t = 0.4, \lambda = 6H$ ).	56

Figure 5.3:	Color maps of partially averaged fluctuating velocity components on the $(x_2, x_3)$ - plane for wind driven flow with LC ( $La_t = 0.7, \lambda = 6H$ ).	57
Figure 5.4:	Color maps of partially averaged fluctuating velocity components on the $(x_2, x_3)$ - plane for wind driven flow with LC ( $La_t = 0.7, \lambda = 4H/3$ ).	57
Figure 5.5:	Color maps of partially averaged fluctuating velocity components on the $(x_2, x_3)$ - plane for wind driven flow with LC ( $La_t = 1.0, \lambda = 6H$ ).	58
Figure 5.6:	Color maps of partially averaged fluctuating velocity components on the $(x_2, x_3)$ - plane for wind driven flow without LC ( $La_t = \infty$ ).	58
Figure 5.7:	Color maps of partially averaged fluctuating velocity components on the $(x_2, x_3)$ - plane for pressure gradient-driven flow.	59
Figure 5.8:	Mean downwind velocity (a) and mean downwind velocity deficit in the upper half of the water column (b) in flows with and without LC.	61
Figure 5.9:	Root mean square (r.m.s.) of downwind (a), crosswind (b) and vertical (c) velocity fluctuations.	62
Figure 5.10:	Normal components of the resolved Reynolds stress in flows with LC (c-f) and without LC (c-f).	63
Figure 5.11:	Production-to-dissipation ratio in the surface log-layer.	65
Figure 5.12:	Budgets of turbulent kinetic energy scaled by $u_\tau^2$ in the surface log-layer.	66
Figure 6.1:	Color maps of partially averaged fluctuating vertical velocity components ( $\langle \bar{u}'_3 \rangle_{x_1} / u_\tau$ ) on the left and concentration fluctuations ( $\langle \bar{C}' \rangle_{x_1} / C_{\text{ref}}$ ) on the right on $(x_2, x_3)$ -plane for all flows simulated.	70
Figure 6.2:	(a) Resolved turbulent vertical scalar flux, (b) contribution to resolved turbulent vertical scalar flux from full-depth large-scale stream-wise vortices (i.e. full-depth LC in wind driven flows with LC).	72
Figure 6.3:	(a) Root mean square of (a) resolved scalar concentration and (b) resolved vertical velocity.	73
Figure 6.4:	Instantaneous snapshots of vertical velocity fluctuations at $x_1 = L_1/2$ , where $L_1$ is the downwind length of the domain in wind-driven flows.	75

Figure 6.5:	Instantaneous snapshots of vertical velocity fluctuations and scalar concentration fluctuations in the uppermost one-eighth portion of the water column at $x_1 = L_1/2$ where $L_1$ is the downwind length of the computational domain.	76
Figure 6.6:	Instantaneous snapshots of downwind velocity fluctuations and scalar concentration fluctuations on a horizontal plane close to the surface within the buffer layer ( $x_3/\delta = 0.96$ ).	76
Figure 6.7:	Near surface budgets of Reynolds averaged scalar transport equation in (a) wind driven flow without LC and (b) in wind driven flow with LC (with $La_t = 0.7$ )	78
Figure 6.8:	Instantaneous velocity vectors superimposed with color contour of (a) concentration fluctuation $\bar{C}'$ and (b) crosswind transport defined as $-\bar{u}'_2 \partial \bar{C}' / \partial x_2$ , in wind-driven flow without LC.	79
Figure 6.9:	Conditionally averaged velocity fluctuation vectors superimposed with color contour of (a) conditionally averaged concentration fluctuation $\langle \bar{C}' \rangle_{\text{conditional}}$ and (b) conditionally averaged crosswind transport, $T_2$ , in wind-driven flow without LC.	80
Figure 6.10:	Components of root mean square of velocity in pressure gradient-driven flow.	85
Figure 6.11:	Mean concentration (a) and mean concentration deficit in the upper half of the water column (b) in flows with and without LC.	87
Figure 7.1:	Comparison of dimensionless vertical gradient of dimensionless Stokes drift velocity shear for different flows with LC.	94
Figure 7.2:	Comparison of transfer velocity evaluated through Stokes drift shear model based on surface renewal theory with LES results.	95
Figure 7.3:	Time/downwind averaged vertical velocity fluctuations, $\langle \bar{u}_3 \rangle_{t,x_1} / u_\tau$ .	96
Figure 7.4:	Comparison of transfer velocity evaluated through large eddy model based on surface renewal theory with LES results.	98
Figure 7.5:	TKE dissipation (a) for pressure gradient-driven flow, (b) for wind driven flows with and without LC	100
Figure 7.6:	Comparison of transfer velocity evaluated through small eddy model based on surface renewal theory with LES results.	101
Figure 7.7:	$\langle \beta^2 \rangle^{1/2}$ for different flows.	103

Figure 7.8:	Comparison of transfer velocity evaluated through surface divergence model based on surface renewal theory with LES results.	104
Figure 8.1:	Comparison of transfer velocity evaluated through models based on surface renewal theory with LES results where cyan down triangle shows pressure gradient driven flow, black diamond shows $La_t = \infty$ , magenta circle shows $La_t = 1.0$ , $\lambda = 6H$ , blue up triangle shows $La_t = 0.7$ , $\lambda = 6H$ , green square shows $La_t = 0.7$ , $\lambda = 4H/3$ and red star shows $La_t = 0.4$ , $\lambda = 6H$ .	110
Figure A.1:	Downwind 1D energy spectra in LES of turbulent channel flow. [87]	132
Figure A.2:	Downwind 1D energy spectra in LES of a turbulent channel flow close to channel walls. [61]	134
Figure B.1:	Momentum balance for (a) pressure driven flow (b) wind driven flows with and without LC where $\langle \bar{u}'_i \bar{u}'_3 \rangle$ is the Reynolds stress; $\langle \tau_{13}^{SGS} \rangle$ is the SGS stress and is the $\langle \tau_{13}^V \rangle$ is the viscous stress	138
Figure B.2:	Scalar balance for (a) pressure driven flow (b) wind driven flows with and without LC where $\langle \bar{u}'_3 \bar{C}' \rangle$ is the Reynolds stress; $\langle q_3 \rangle$ is the SGS stress and $\frac{\partial \langle C \rangle}{\partial x_3}$ is the vertical diffusive flux	142
Figure D.1:	Dimensionless budgets of $\langle \bar{C}' \bar{C}' \rangle$ within surface diffusive and buffer regions.	147
Figure D.2:	Dimensionless budgets of $\langle \bar{C}' \bar{C}' \rangle$ within surface log-layer.	148
Figure E.1:	Dimensionless budgets of $\langle \bar{C}' \bar{u}'_3 \rangle$ within surface diffusive and buffer regions.	152
Figure E.2:	Dimensionless budgets of $\langle \bar{C}' \bar{u}'_3 \rangle$ within surface log-layer.	153
Figure F.1:	Mean concentration in flows with and without LC at different Schmidt numbers.	154
Figure F.2:	Transfer velocity, $K_{LES}/u_\tau$ at different $Sc$ numbers.	155
Figure G.1:	Mean concentration in flows with and without LC at different Reynolds numbers.	157
Figure G.2:	Comparison transfer velocity ( $K$ ) at different Reynolds numbers in flows with ( $La_t = 0.7$ , $\lambda = 6H$ ) and without LC.	158

## List of Symbols

$C_{\text{bulk}}$	Mean concentration at the bulk
$C_{\text{surface}}$	Mean concentration at the surface
$\delta_c$	Thickness of concentration boundary layer
$F$	Air-sea flux
$K$	Transfer velocity
$Sc$	Schmidt number
$u_{10}$	Wind speed at 10 <i>m</i> above the water surface
$\varepsilon$	Turbulent kinetic energy (TKE) dissipation rate
$\nu$	Kinematic viscosity
$K_H$	Heat transfer velocity
$Pr$	Prandtl number
$D$	Molecular diffusivity of the scalar in water
$\Delta C$	Difference in concentration between the surface and the bulk of the flow
$\lambda$	Dominant wavelength of surface waves
$La_t$	Turbulent Langmuir number
$Re$	Reynolds number ( $UL/\nu$ )
$u_i$	<i>i</i> th component of the non-dimensional time-filtered velocity
$x_i$	<i>i</i> th component of position vector

$p$	Pressure
$\rho_0$	Constant density
$L$	Characteristic length of large scales
$U$	Characteristic velocity
$t$	Time
$k$	turbulent kinetic energy
$Re_t$	Turbulent Reynolds number ( $UL/\nu$ )
$\eta$	Characteristic length scale of small scales
$N$	Number of grid points
$\psi$	Flow property
$\tau_{ij}$	Reynolds stress tensor
$q_j$	Reynolds fluxes
$G$	Filter function
$\Delta_f$	Filter function
$\tau_{ij}^{\text{SGS}}$	Sub-grid scale (SGS) stresses
$q_j^{\text{SGS}}$	Sub-grid scale (SGS) fluxes
$\tau_r$	Surface renewal time scale
$\bar{F}$	Mean vertical mass flux
$\bar{K}$	Mean transfer velocity
$\Pi$	Resolved pressure
$\varepsilon_{ijk}$	Totally antisymmetric third-rank tensor
$\omega_i$	$i$ th component of the non-dimensional time-filtered vorticity

$\phi^s$	Non-dimensional Stokes drift velocity
$C$	Passive scalar concentration
$Re_\tau$	Reynolds number
$\delta$	Channel half depth
$u_\tau$	Friction velocity associated with wind stress
$\tau_w$	Wind stress
$\rho$	Density
$u_s$	Stokes drift velocity
$\omega$	Dominant frequency
$\kappa$	Dominant surface gravity wave wavenumber
$a$	Amplitude of surface gravity waves
$\bar{u}_i$	$i$ th component of the non-dimensional space-filtered velocity
$\bar{\omega}_i$	$i$ th component of the non-dimensional space-filtered vorticity
$\bar{\Pi}$	Space-filtered pressure
$\nu_T$	Eddy viscosity
$C_s$	Dimensionless Smagorinsky coefficient for momentum equation
$\bar{\Delta}$	Low-pass filter width
$ \bar{S} $	Norm of the filtered strain-rate tensor
$\bar{S}_{ij}$	Filtered strain-rate tensor
$D_T$	Eddy (turbulent) diffusivity
$C_c$	Dimensionless Smagorinsky coefficient for scalar equation
$x_1$	Downwind direction



$x_2$	Crosswind direction
$x_3$	Vertical direction
$u_1$	Velocity in the downwind direction
$u_2$	Velocity in the crosswind direction
$u_3$	Velocity in the vertical direction
$H$	Total depth
$\langle \bar{u}_i \rangle$	$i$ th component of velocity averaged in time & in horizontal directions
$\bar{u}'_i$	$i$ th component of the fluctuation of the resolved velocity
$\langle \bar{u}'_i \rangle$	Partially averaged $i$ th component of the velocity fluctuation
$\langle \bar{u}_{\text{surface}} \rangle$	Downwind velocity evaluated at the surface
$x_3^+$	Distance to the surface in plus units
$C_\delta$	Concentration at the top
$C_{-\delta}$	Concentration at the bottom
$U_s$	Stokes drift velocity
$w_s$	Maximum vertical velocity associated with large scale eddies
$h$	Depth of the water column
$k_f$	Constant showing that average renewal is a fraction of that caused by $w_s$
$F_r$	Portion of an eddy consisting of an upwelling

## Abstract

Over the past century the study of gas exchange rates between the atmosphere and the ocean has received increased attention because of concern about the fate of greenhouse gases such as CO<sub>2</sub> released into the atmosphere. Of interest is the oceanic uptake of CO<sub>2</sub> in shallow water coastal regions as biological productivity in these regions is on average about three times larger than in the open ocean. It is well-known that in the absence of breaking surface waves, the water side turbulence controls gas transfer of sparingly soluble gases such as CO<sub>2</sub> from the air to the water. The dependence of gas transfer on wind-driven shear turbulence and convection turbulence generated by surface cooling has been investigated previously by others. However, the effect of Langmuir turbulence generated by wave-current interaction has not been investigated before. More specifically, Langmuir turbulence is generated by the interaction of the wind-driven shear current with the Stokes drift velocity induced by surface gravity waves.

In this dissertation, large-eddy simulations (LES) of wind-driven shallow water flows with Langmuir turbulence have been conducted and scalar transport and surface scalar transfer dynamics analyzed. The scalar represents the concentration of a dissolved gas such as CO<sub>2</sub> in the water. In flows with Langmuir turbulence, the largest scales of the turbulence consist of full-depth Langmuir circulation (LC), parallel downwind-elongated, counter-rotating vortices acting as a secondary structure to the mean flow.

LES guided by the full-depth LC field measurements of Gargett & Wells [27] shows that Langmuir turbulence plays a major role in determining scalar transport throughout the entire water column and scalar transfer at the surface. Langmuir turbulence affects scalar transport and its surface transfer through 1. the full-depth homogenizing action of the large-scale LC and 2. the near-surface vertical turbulence intensity induced by the Stokes drift velocity shear. Two key parameters controlling the extent of these two mechanisms are the dominant wavelength ( $\lambda$ ) of the surface waves generating the turbulence and the turbulent Langmuir number,  $La_t$ , which is inversely proportional to wave forcing relative to wind forcing.

Furthermore, LES representative of the field measurements of Gargett et al. [28] shows that Langmuir turbulence increases transfer velocity (a measure of mass transfer efficiency across the air-water interface) dramatically with respect to shear-dominated turbulence.

Finally, direct resolution of the surface mass transfer boundary layer allows for the LES to serve as a testing ground for bulk parameterizations of transfer velocity. Several well-established parameterizations are tested and a new parameterization based on Stokes drift velocity shear is proposed leading to encouraging results.

# Chapter 1:

## Introduction

### 1.1 Context and Motivation

Scalar exchange between the atmosphere and the ocean has a significant impact on environmental systems. There has been a growing interest in the transfer of sparingly soluble greenhouse gases such as CO<sub>2</sub> because of the fact that approximately 30-40% of man-made CO<sub>2</sub> is taken up by the oceans [18]. Moreover, due to the increasing trend of atmospheric CO<sub>2</sub> concentration, estimates of net global CO<sub>2</sub> ocean uptake have become more critical. According to numerous studies, estimates of net global CO<sub>2</sub> ocean uptake may vary from about 0.8  $Gt C yr^{-1}$  to about 2.2  $Gt C yr^{-1}$  [7, 97]. In the carbon cycle, carbon is exchanged among main regions of the Earth and the greatest exchange occurs between the atmosphere and the oceans and other water ways. Balance of CO<sub>2</sub> cycle is dominated by mass exchange across air-water interface which makes understanding of the mechanisms behind this process essential.

Mass flux across the air-water interface can be expressed as a product of transfer velocity and concentration difference across the interface. Transfer velocity is a measure of transfer efficiency and in general depends on the turbulence characteristics of the air flow above the air water interface and the water flow below. For sparingly soluble gases (such as CO<sub>2</sub>) water side controls the mass transfer. This is due to the fact that the transfer velocity

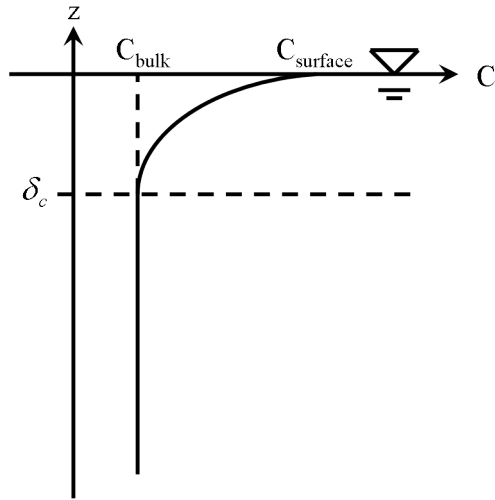


Figure 1.1: Schematic of the mass concentration diffusion sublayer at the surface of a water body where  $\delta_c$  denotes thickness of the concentration boundary layer and  $C$  denotes the mean concentration.

depends on the molecular diffusivity and molecular diffusivity of sparingly soluble gases in air is much larger than in water [4, 18, 99]. In the water-side, surface mass transfer occurs across a very thin turbulent boundary layer which tends to be a few millimeters thick (Fig. 1.1) [19]. As a result of this, it is very challenging to analyze concentration and transfer velocity across this boundary layer through field measurements or experiments. Thus, the scarce data coming from field measurements or experiments is often used to develop parameterizations of mass transfer that are linked to bulk (commonly measured) quantities such as wind speed [55, 96, 100]. For example, Fig. 1.2 shows the climatological annual mean of sea-air  $\text{CO}_2$  flux ( $\text{g-Cm}^{-2} \text{yr}^{-1}$ ) for the reference year 2000 calculated using wind speed parameterization [84]. Note that positive values (yellow-orange-red) indicate sea-to-air fluxes and negative values (blue-magenta) indicate air-to-sea fluxes.

As mentioned earlier, about one third of man-made  $\text{CO}_2$  is transferred across the sea surface into the oceans. Once  $\text{CO}_2$  enters seawater and dissolves, it reacts with water ( $\text{H}_2\text{O}$ )

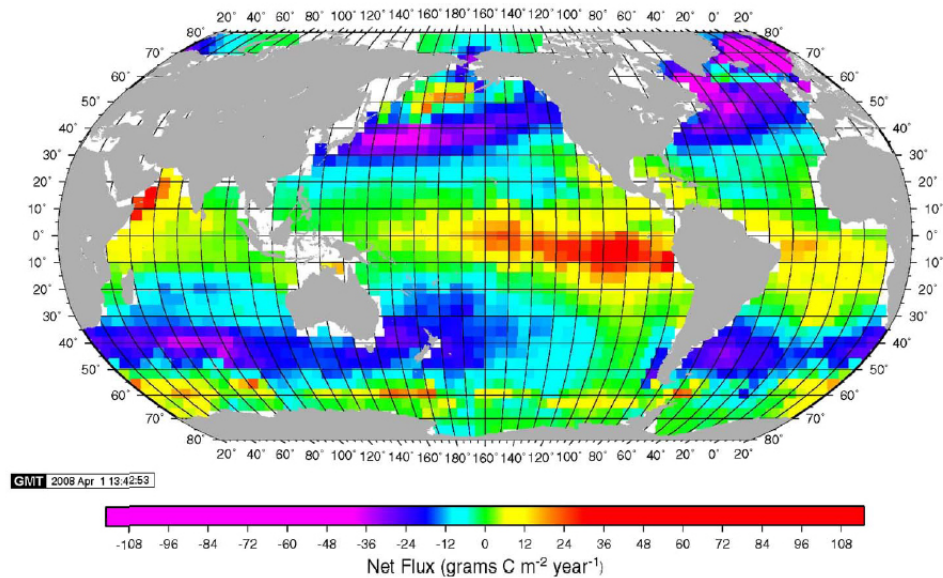


Figure 1.2: Climatological mean annual sea-air CO<sub>2</sub> flux ( $g-Cm^{-2} yr^{-1}$ ) for the reference year 2000 (non-ElNino conditions). [84] Reprinted with permission from Deep Sea Research Part II: Topical Studies in Oceanography, 56(8-10), T. Takahashi, S.C. Sutherland, R. Wanninkhof, C. Sweeney, R.A. Feely, D.W. Chipman, B. Hales, Friederich. G., Chavez F., C. Sabine, A. Watson, D.C.E. Bakker, U. Schuster, N. Metzl, H. Yoshikawa-Inoue, M. Ishii, T. Midorikawa, Y. Nojiri, A. Körtzinger, T. Steinhoff, Hoppema. M., J. Olafsson, T.S. Arnarson, B. Tilbrook, T. Johannessen, A. Olsen, R. Bellerby, C.S. Wong, B. Delille, N.R. Bates, and H.J.W. de Baar., Climatological mean and decadal change in surface ocean pCO<sub>2</sub>, and net sea-air CO<sub>2</sub> flux over the global oceans, 554-577, Copyright (2009), with permission from Elsevier.

and forms carbonic acid (H<sub>2</sub>CO<sub>3</sub>). Then carbonic acid dissociates into hydrogen ions (H<sup>+</sup>) and bicarbonate ions (HCO<sub>3</sub><sup>-</sup>), acidifying the ocean. Ocean acidification could be expected to have major negative impacts on corals and other marine organisms that build calcium carbonate shells and skeletons [21].

There is also a concern about the transfer of gases from the sea to the air. Gases such as dimethyl sulphide (DMS) and methyl iodide (CH<sub>3</sub>I) are produced in the oceans and they can influence climate once they get into the atmosphere [95]. In conclusion, improved understanding of air-water exchange is vital.

The equation widely used in the oceanography community to parameterize air-sea flux,  $F$  ( $\text{mol m}^{-2} \text{s}^{-1}$ ), of a sparingly soluble, nonreactive gas is given by

$$F = K(C_{\text{bulk}} - C_{\text{surface}}) \quad (1.1)$$

where  $K$  ( $\text{m s}^{-1}$ ) is the gas transfer velocity,  $C_{\text{bulk}}$  ( $\text{mol m}^{-3}$ ) is the concentration of the gas in the bulk flow and  $C_{\text{surface}}$  ( $\text{mol m}^{-3}$ ) is the concentration of the gas at the water surface. For example, Ward et al. (2004) [97] used Eqn. 1.1 to measure  $\text{CO}_2$  flux across the air-sea interface during a 14-day study in the equatorial Pacific Ocean.

Quoting Zappa et al. (2007) [100], "*since field measurements of the concentration difference are usually straightforward to obtain in almost any type of aqueous system, the major challenge for modeling accurate fluxes has been to develop a quantitative model of  $K$* ".

The transfer velocity  $K$  incorporates (1) the diffusivity of the gas in water which varies with temperature and between different gases and (2) the effect of vertical turbulent mixing near the surface (see [2, 97, 100] among others). Accordingly, popular models or parameterizations of  $K$  depend on the Schmidt number ( $Sc$ ; the ratio of molecular viscosity to molecular diffusivity of gas in water) and bulk characterizations of the turbulence. Note that these parameterizations do not consider effects such as possible dissociation of the gas in water.

A popular model for  $K$  is the model of Wanninkhof (1992) [94] given by

$$K = 0.31u_{10}^2 \quad (1.2)$$

where  $u_{10}$  is the wind speed at 10 m above the water surface. Here  $K$  and  $u_{10}$  are in units of  $m s^{-1}$ . The proportionality dimensional 0.31 factor was determined using  $CO_2$  flux data, thus  $K$  in Eqn. 1.2 corresponds to the transfer velocity of  $CO_2$ . In this model  $u_{10}$  serves as an indicator of the water-side, near-surface turbulent mixing intensity because the wind is responsible for driving a surface current characterized by shear which produces turbulence.

The model in Eqn. 1.2 is used for gases other than  $CO_2$  via the following expression relating the transfer velocities and Schmidt numbers of two gases ([40, 72]):

$$\frac{K_1}{K_2} = \left( \frac{Sc_2}{Sc_1} \right)^{1/2} \quad (1.3)$$

Inserting the relation in Eqn. 1.3 into Eqn. 1.2 (with  $K_1$  and  $Sc_1$  corresponding to the transfer velocity and Schmidt number for  $CO_2$  ( $Sc = 660$  in seawater) and  $K_2$  and  $Sc_2$  being the transfer velocity and Schmidt number of a gas of interest) one can get

$$K = 0.31u_{10}^2(Sc/660)^{-1/2} \quad (1.4)$$

where the subscript 2 has been dropped from  $K$  and  $Sc$ .

A more sophisticated model for  $K$  is the small eddy model described and tested in the dissertation. This model is based on surface renewal theory and (as the name suggests) takes the surface renewal time scale to be the time scale characteristic of small-scale, near-surface turbulent eddies on the water-side of the air-water interface. As a result,  $K$  is parameterized as

$$K \propto (\epsilon v)^{1/4} Sc^{-1/2} \quad (1.5)$$



where  $\nu$  is kinematic viscosity of sea water and  $\varepsilon$  is the dissipation rate of turbulent kinetic energy (TKE) of the water-side turbulence at the surface.

Zappa et al. (2007) [100] has tested models of  $K$  using field measurements rather than computations as we intend to do. They compared  $K$  measured directly in the field versus  $K$  modeled with the small eddy model in Eqn. 1.5 and the wind speed parameterization in Eqn. 1.4, respectively (See Figs 3a and 3b of the paper by [100]). Note that the direct field measurements of  $K$  were made concurrently with measurements of  $\varepsilon$  needed for the small eddy model prediction in 1.5. Their analysis shows that that the small eddy model performs better than the wind speed model in predicting  $K$  for a wide range of near-surface turbulent mixing conditions, including turbulence generated by rain, tides and wind.

An interesting aspect of the Zappa et al. (2007) [100] analysis is the fact that heat may be used as a proxy tracer for gas. Since both heat and gas are scalars, the heat transfer velocity,  $K_H$ , is assumed to scale directly to the gas transfer velocity,  $K$ , as

$$K = K_H \left( \frac{Sc}{Pr} \right)^{-1/2} \quad (1.6)$$

where the ratio  $Sc/Pr$  is often referred to as the Lewis number and  $Pr$  is the Prandtl number (the ratio of molecular viscosity to thermal diffusivity in water). The expression in Eqn. 1.6 is consistent with Eqn. 1.3. Although the difference between  $Pr$  for heat and  $Sc$  for a typical gas is large (e.g.  $Pr = 7$ ,  $Sc = 660$  for  $\text{CO}_2$  in seawater at  $20^\circ\text{C}$ ), measurements of Jahne et al. (1989) [40] have shown that this extrapolation is correct to within 10% if the uncertainty of the diffusivity of the gas in the water is less than 5%.

The reader should note that the analysis made in this dissertation does not include chemistry effects, and strictly speaking it is valid only for non-reactive chemicals which would then exclude CO<sub>2</sub>. However, the author argues that diffusivity and turbulent mixing are dominant factors over chemistry effects, thus the analysis can still be approximately applied to gases such as CO<sub>2</sub>. The reasons why this argument is valid can be summarized as follows:

- In transfer velocity models such as the previously explained small eddy model, transfer velocity ( $K$ ) is taken to depend on diffusivity and turbulent mixing only, and chemistry effects are excluded.
- Models such as the small eddy model have been shown to predict the  $K$  for CO<sub>2</sub> transfer into the ocean up to some level of accuracy.
- Given that  $K$  models such as the small eddy model can predict  $K$  for CO<sub>2</sub> across the air-water interface up to some level of accuracy, this implies that the original assumption of the model (i.e. that  $K$  depends primarily on diffusivity and turbulence only without considering chemistry effects) is reasonable.
- If  $K$  for CO<sub>2</sub> is primarily dependent on diffusivity and turbulent mixing, then the present analysis performed (i.e. using transport equations resolving turbulence effects and diffusivity via highly resolved computations in the form of large-eddy simulation (LES) while excluding chemistry in order to compute  $K$ ) should then be applicable up to some level of accuracy.

Furthermore, quoting from Marine Chemistry lecture notes of Massachusetts Institute of Technology [20] "*it is possible that chemical reactions within the thin boundary layer may serve to sharpen gradients of some gases, thereby increasing the fluxes of those gases. This kind of enhancement certainly occurs for extremely reactive compounds, particularly photo-reactive species. This might also be the case for CO<sub>2</sub> since it converts to bicarbonate and carbonate. It is possible to assess the significance of this by comparing the time constant of this reaction, which is of the order of a minute, with the time it takes for a molecule to transit the boundary layer via molecular diffusion, which is related to  $T \approx L^2/D$  and using typical values ( $L = 40 \times 10^{-6}$  m and  $D = 2 \times 10^{-9}$  m<sup>2</sup> s<sup>-1</sup>) which yields  $T \approx 1$  second. Thus, a CO<sub>2</sub> molecule spends far too little time in the boundary layer to be affected by chemical reaction while it is there.*"

## **1.2 Objectives**

Parameterizations of mass transfer mentioned in Section 1.1 are generally based on a theory called *surface renewal theory*. Chapter 7 of this study focuses on the accuracy of parameterizations of transfer velocity based on surface renewal theory. Testing of these parameterizations is performed via highly resolved computations of shallow water, homogeneous, wind-driven flow with and without surface wave effects. These computations are able to resolve scalar (mass) concentration across the mass transfer boundary layer (depicted in Fig. 1.1). Thus, these computations present the opportunity to compare transfer velocity computed via parameterizations with transfer velocity obtained directly in the

computations. The computations also include wave effects which lead to the formation of full-depth Langmuir circulation (LC) [49].

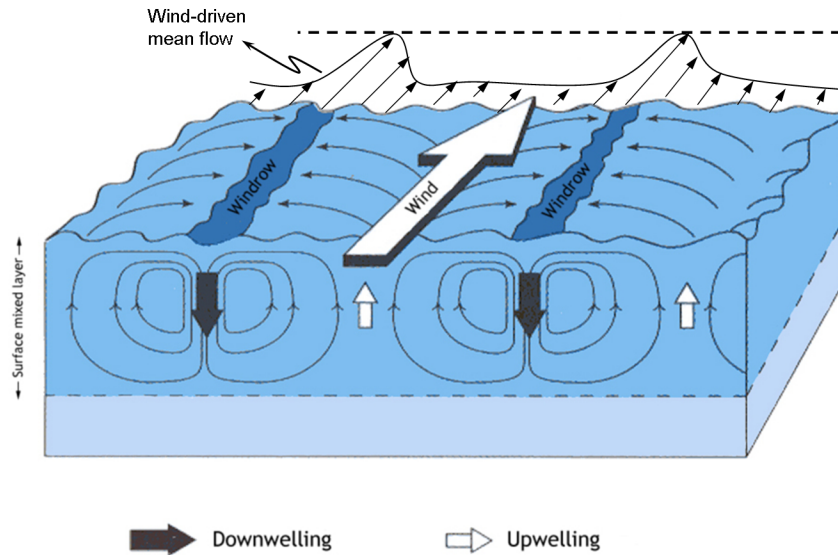


Figure 1.3: Sketch showing the cellular structure of Langmuir circulation (LC) characterizing the turbulence advected by the wind-driven mean flow.

First observed by Langmuir [49], LC consists of parallel counter-rotating vortices roughly aligned in the direction of the wind as seen in Fig. 1.3. These vortices are characteristic of the turbulence (i.e. the Langmuir turbulence) advected by the mean flow. At the surface convergence of the vortices there is the tendency for the accumulation of lines of foam often referred to as windrows (see Fig. 1.3). LC can be observed on any body of water including oceans, seas, lakes, estuaries, and rivers under wind speeds greater than  $3 \text{ m s}^{-1}$ . Wind speeds exceeding  $3 \text{ m s}^{-1}$  are generally sufficient for the interaction between the shear current and Stokes drift velocity induced by the surface waves [14], which results in generation of LC. LC often occurs in deep water within the upper ocean mixed layer (i.e. the surface mixed layer) far from the bottom. However recently, Gargett and collaborators

[26–28] have made measurements of full-depth LC in shallow water regions. Full-depth LC in coastal shelf regions is believed to be associated with sediment transport and has an important effect on bottom-dwelling biological systems [27, 28]. Here we propose and test new surface renewal based parameterizations able to capture the influence of full-depth LC on mass boundary layer, transfer velocity and overall scalar transport throughout the water column.

The highly resolved computations presented here consist of large-eddy simulation (LES). LES is a computation that highly resolves the turbulent scales of the flow. In LES the large scale motions of the flow are resolved explicitly, while the effect of the smaller unresolved scales (also called subgrid scales) is modeled using a subgrid-scale (SGS) model. A brief description of LES will be given in Chapter 4.

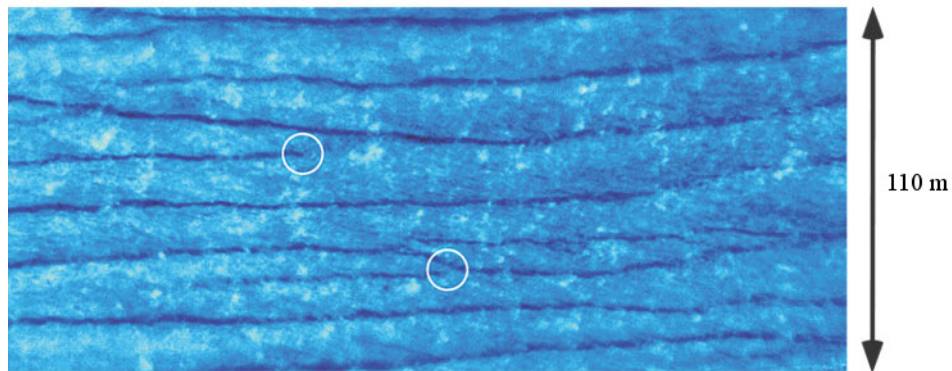


Figure 1.4: Airborne infrared imagery over Tampa Bay. [57] Reprinted with permission from Continental Shelf Research, 25, G. O. Marmorino, G. B. Smith, and G. J. Lindemann, Infrared imagery of large-aspect-ratio Langmuir circulation, 1-6, Copyright (2004), with permission from Elsevier.

Our work is motivated by airborne infrared imagery over Tampa Bay suggesting that LC can affect mass transfer through stretching and compression of the mass boundary layer below the air-sea interface [57]. Fig. 1.4 shows high altitude imagery made near the mouth

of Tampa Bay [57]. Note that surface convergence of LC coincides with the dark streaks which are about  $0.2^{\circ}\text{C}$  cooler than the ambient surface water implying a stretching and compression of the surface thermal boundary layer. We hypothesize a similar stretching and compression mechanism should also impact the surface mass concentration boundary layer and thus mass transfer across the air water-interface.

According to Marmorino et al. (2004) [57], the individual streaks in Fig. 1.4 extend over about  $1\text{ km}$  in the downwind direction. Furthermore, the spacing between streaks is about 20 meters, or about 10 times the mean water depth of  $\approx 2.1\text{ m}$ . Hunter and Hill (1980) [38] have also reported similar Langmuir cells (streaks) in shallow water region in the Texas shelf (water depths 6-14  $m$ ). Further evidence that LC is possible under very shallow conditions is given by Faller and Caponi (1978) [24] who have reported Langmuir cells in the laboratory at depths between 2.5 and 7.5  $cm$ .

At high wind speeds ( $> 8\text{ m s}^{-1}$ ) wave-breaking plays a major role in mass transfer at the air-sea interface through air entrainment. However, at low to moderate wind speeds (3-8  $\text{m s}^{-1}$ ), as in our simulations, micro-breaking (i.e. breaking of small-scale waves without entrainment of air) takes place (white spots seen in Fig. 1.4). Effect of micro-breaking waves is small on LC compared to the effect of breaking waves. As a consequence, our simulations will not resolve wave-breaking events, thus we concentrate on mass transfer through diffusion and the impact of water-side turbulence including LC on this process. This study marks the first time that the impact of LC on mass transfer has been investigated experimentally or computationally.

In our LES, transfer velocity,  $K$ , can be computed directly as follows

$$K = \frac{D}{\Delta C} \frac{\partial C}{\partial x_3} \Big|_{x_3=\delta} \quad (1.7)$$

where  $D$  is the molecular diffusivity of the scalar in water and  $\Delta C$  is the difference in concentration between the surface and the bulk region of the flow ( $\Delta C = (C_{\text{surface}} - C_{\text{bulk}})$ , see Fig. 1.1), and  $(\partial C/\partial x_3)|_{x_3=\delta}$  is the vertical gradient of the mean concentration computed at the surface.

As pointed out before, previous studies have focused on the impact of turbulent processes such as winds, wave breaking etc. on mass transfer across the air-water interface. The impact of Langmuir turbulence characterized by LC generated via the interaction between wind and waves remains unknown. Therefore, the main goal of this dissertation is to determine the importance of LC for near-surface mass transfer and scalar transport in the water column. Towards this goal, I will address two sub-objectives.

First, I will identify the physical mechanism(s) by which Langmuir turbulence and associated LC affects scalar transport throughout the entire water column and mass transfer at the surface. The dependence of scalar transport and surface mass transfer on Langmuir turbulence will be investigated as a function of wind and wave forcing parameters characterizing the intensity of the turbulence and LC. Wind and wave forcing parameters consist of the wavelength ( $\lambda$ ) of the surface waves generating LC and the turbulent Langmuir number ( $La_t$ ). The latter is inversely proportional to wind forcing relative to wave forcing. Simulations will be performed at relatively low but turbulent Reynolds numbers ( $Re$ ) and at low Schmidt numbers ( $Sc$ ) due to computational constraints. We hypothesize that transfer

velocity,  $K$ , in wind-driven shear flow increases in the presence of Langmuir turbulence (i.e. LC) relative to  $K$  in a similar flow without wave-current interaction (i.e. without LC). We seek to determine/ understand the dependence of this increase in  $K$  on wind/wave forcing parameters  $\lambda$  and  $La_t$ . Such understanding will enable improved parameterizations of  $K$  that take into account the impact of LC.

As for the second sub-objective, three commonly used parameterizations (based on surface renewal theory) and a new parameterization for estimation of  $K$  will be compared to the  $K$  computed directly in LES through Eqn. 1.7. The new parameterization, introduced here for the first time, explicitly accounts for the presence of large-scale (full-depth) LC. I will quantify how well predictions of  $K$  from those parameterizations agree with the values of  $K$  determined from large-eddy simulations. I will also examine how well each of the four parameterizations captures the observed dependence of  $K$  upon wind and wave forcing (i.e. LC) parameters  $\lambda$  and  $La_t$ . I hypothesize that traditional models such as the small eddy model [100] do not capture the dependence of  $K$  upon  $\lambda$  and  $La_t$  because they assume that  $K$  depends solely on near-surface, small-scale turbulence. However, as noted earlier, we hypothesize that large-scale eddies, namely full-depth LC, also play an important role in determining  $K$ .

### **1.3 Organization of the Dissertation**

Chapter 2 presents literature reviews on turbulence from physical and mathematical perspectives and on mass transfer models. In Chapter 3 a brief description of the boundary exchange at the air-water interface is presented. Computational methodology will be ex-



plained in detail in Chapter 4. Following that, statistics of the turbulence are presented in order to understand how LC and its associated Langmuir turbulence affect scalar transport throughout the water column (Chapters 5 and 6). Predictions of transfer velocity from surface renewal parameterizations are compared to the transfer velocity measured directly in the LES in Chapter 7. Finally, Chapter 8 presents the conclusions reached by the current research together with recommendations for future work.

## **Chapter 2:**

### **Literature Review**

#### **2.1 Turbulence**

In this chapter we first discuss the importance of turbulence as a physical phenomenon and describe the main features of turbulent flow that are easily recognized. Following that, we explain turbulence in a mathematical sense and finally discuss the numerical approaches to turbulence.

Most flows in nature and technical applications are turbulent: atmosphere and ocean currents, the flow around aircraft wing tips, the flow through pumps and turbines etc. Because of this, scientists and engineers are interested in understanding and modeling turbulence.

The Navier-Stokes equations are used to describe Newtonian incompressible fluid flows (laminar or turbulent) through momentum balances in all spatial dimensions. Turbulent flows contain a wide range of temporal and spatial scales which are admitted by the Navier-Stokes equations. Solution of Navier-Stokes equations for a turbulent flow in most applications requires intractable, expensive grid resolutions in order to resolve all of the scales of the turbulence. Alternative to direct approach of solving Navier-Stokes equations is statistical approach. Both of the approaches will be discussed in Section 2.1.3.

### 2.1.1 Physical Description of Turbulence

Although turbulence is an ubiquitous phenomena, it is difficult to give a concise physical definition for it. First known description of turbulence was given by Leonardo da Vinci who observed a water jet coming from a square hole. There are also numerous other descriptions and collection of images of turbulence (e.g. Album of Fluid Motion by van Dyke [93]). Yet they still do not sufficiently define turbulent flow with all of its aspects.

Turbulent flow has some special features that separates it from laminar flow. These special features are described in many turbulence books including the ones by Pope [68], Tennekes and Lumley [88], and Pozrikidis [69]. Below is a list of some characteristics of turbulent flows:

- **Randomness (i.e. irregularity)** - The properties of the fluid at any given point can not be predicted. But statistical properties (time and space averages, correlation functions, and probability density functions) show regular behavior.
- **Diffusivity** - Turbulence is associated with strong mixing and high rates of momentum, heat and mass transfer.
- **Large Reynolds numbers** - Turbulent flows always occur at high Reynolds numbers. They are caused by the complex interaction between the viscous terms and the inertia terms in the momentum equations.
- **Three dimensional vorticity fluctuations** - Turbulent flows are rotational; that is, they have non-zero vorticity. Mechanisms such as the stretching of three-dimensional vortices play a key role in turbulence. *"Typically energy gets transferred from the*

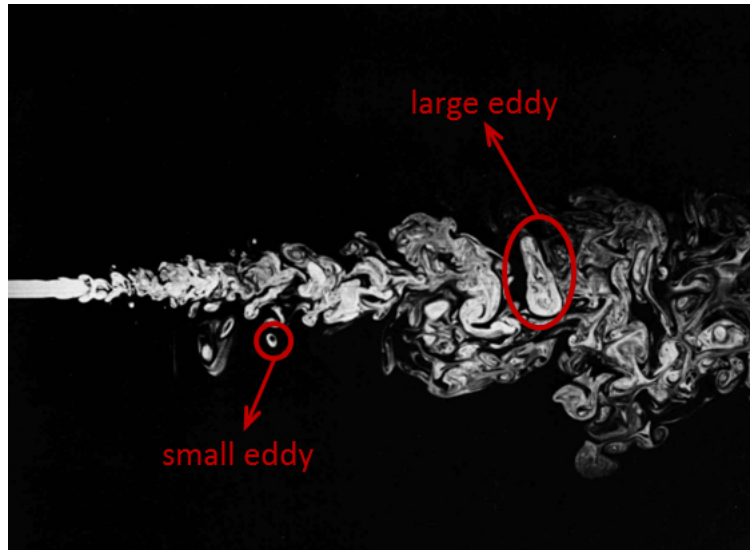


Figure 2.1: Structures in a turbulent flow. [17] Reprinted with permission from P. E. Dimotakis, R. C. Miake-Lye, and D. A. Papantoniou, Structure and dynamics of round turbulent jets, Phys. Fluids, 26:3185-3192, 1983. Copyright 1983, American Institute of Physics.

*large vortices to the smaller vortices via vortex stretching. Vortex stretching is a deformation of the vortices making them smaller and adding kinetic energy to them"*  
[8].

- **Dissipation** - Kinetic energy gets converted into heat due to viscous shear stresses. Turbulent flows die out quickly when no energy is supplied. Random motions that have insignificant viscous losses, such as random sound waves, are not turbulent.
- **Continuum** - Turbulence is a continuum process. The smallest scale of turbulence is much larger than the molecular scales in most applications of interest.
- **Broadband spectrum in space and time** - Turbulent flows are characterized by structures on a broad range of spatial and temporal scales. Often these structures are seen in terms of eddies ranging from very large (of size on the order of the flow region) to small (of width on the order of millimeters) (See Fig. 2.1). Eddies are

packets of fluid elements jostling each other and rapidly breaking down to smaller eddies. In a turbulent flow large eddies contain most of the turbulent kinetic energy. This energy is passed down from the largest eddies to the smallest eddies through a process called the energy cascade. At the smallest scales, the energy is dissipated to heat by viscous effects (See Figure 2.1).

- **Turbulent flows are flows** - Turbulence is not a feature of the fluid but of the fluid flow.

### 2.1.2 Mathematical Description of Turbulence

The Navier-Stokes equations for an incompressible Newtonian fluid are given as

$$\frac{\partial u_i}{\partial t} + \frac{\partial (u_i u_j)}{\partial x_j} = -\frac{1}{\rho_0} \frac{\partial p}{\partial x_i} + \nu \frac{\partial^2 u_i}{\partial x_j \partial x_j} \quad (2.1a)$$

$$\frac{\partial u_i}{\partial x_i} = 0 \quad (2.1b)$$

where  $\nu$  is the kinematic viscosity and  $\rho_0$  is the constant density.

For convenience, let us consider non-dimensional form of Navier-Stokes equations. For this purpose we introduce a characteristic length scale  $L$  and a characteristic velocity scale  $U$  and we set

$$x_i = Lx'_i, \quad u_i = Uu'_i, \quad t = \frac{L}{U}t', \quad \text{and} \quad p = \rho_0 U^2 p'$$

where prime ( $\cdot'$ ) denotes non-dimensional quantities. Using the scales above, we can re-write Eqn. 2.1a as

$$\frac{U^2}{L} \frac{\partial u'_i}{\partial t'} + \frac{U^2}{L} \frac{\partial (u'_i u'_j)}{\partial x'_j} = -\frac{U^2}{L} \frac{\partial p'}{\partial x'_i} + \nu \frac{U}{L^2} \frac{\partial^2 u'_i}{\partial x'_j \partial x'_j} \quad (2.2)$$

Dividing both sides of Eqn. 2.2 by  $\frac{U^2}{L}$ , one can obtain

$$\frac{\partial u'_i}{\partial t'} + \frac{\partial u'_i u'_j}{\partial x'_j} = -\frac{\partial p'}{\partial x'_i} + \frac{1}{Re} \frac{\partial^2 u'_i}{\partial x'_j \partial x'_j} \quad (2.3)$$

where  $Re$  is the Reynolds number which is defined as  $Re = UL/\nu$ .

### 2.1.3 Numerical Approach to Turbulence

To give the reader an idea of the computational cost for the numerical approaches that will be discussed, we first introduce the scales of turbulence.

#### 2.1.3.1 Scales of Turbulence

As explained briefly in Section 2.1.1, motions in a turbulent flow exist over a broad range of length and time scales. Large eddies contain most of the turbulent kinetic energy and small eddies dissipate the energy they receive from larger eddies in the spectrum. This rises the question: How do we determine "large" and "small"? We can determine the characteristic length scale of large eddies by using definition below (See Durbin & Reif [23] for derivation):

$$L = k^{3/2}/\varepsilon \quad (2.4)$$

where  $k$  is the turbulent kinetic energy ( $k \equiv \frac{1}{2}(u_1^2 + u_2^2 + u_3^2)$ ) and  $\varepsilon$  is the energy dissipation rate ( $\varepsilon \approx u^3/L$  which is a representation due to Kolmogorov). Using this length scale we can also define a Reynolds number,  $Re_t$ , associated with large eddies as

$$Re_t = \frac{UL}{\nu} \quad (2.5)$$

For instance, for the earth's planetary boundary layer with characteristic velocity scale  $U \sim 1 \text{ m/s}$ , characteristic length scale is  $L \sim 1 \text{ km}$  and the Reynolds number is  $Re_t \sim 10^8$ . Note that Reynolds number gives a measure of inertial forces to viscous forces. When  $Re_t$  is large, viscosity has a negligible effect on the large eddies with scales  $U$  and  $L$ . The small eddies, however, are controlled by viscosity. In 1941, Kolmogorov proposed a theory based on three important hypotheses combined with dimensional arguments and experimental observations. According to his first similarity hypothesis, for very high  $Re_t$ , the statistics of the small eddy motions, being independent of the larger scales, are universally and uniquely determined by the viscosity  $\nu$  and the rate of energy dissipation  $\varepsilon$  (See [23, 68]). Thus, using these two quantities, we can define a length scale that is characteristic of small eddy motions as

$$\eta = (\nu^3/\varepsilon)^{1/4} \quad (2.6)$$

Moreover, the ratio between large and small eddies can be calculated using the relationship below

$$\frac{\eta}{L} = Re_t^{-3/4} \quad (2.7)$$

Thus, number of grid points  $N$  in one direction needed to resolve the small scales is

$$N_{1D} \approx \frac{L}{\eta} = Re_t^{3/4} \quad (2.8)$$

This is true for all three directions [23]. Thus, for a three-dimensional computation, number of grid points required would be

$$N_{3D} \sim N_{1D}^3 \sim Re_t^{9/4} \quad (2.9)$$

As mentioned previously, for the earth's planetary boundary layer example,  $Re_t \approx 10^8$ . Then, the number of grid points for this example becomes  $N_{3D} \sim 10^{18}$  which is astronomical.

### 2.1.3.2 Direct Numerical Simulation (DNS)

DNS is the most accurate approach for simulating turbulence since it does not introduce any averaging or approximation of Navier-Stokes equations other than numerical discretization [29, 73, 74, 98]. DNS resolves all scales of turbulent flow explicitly and to ensure this, the grid spacing and the time step must be small enough to capture the dynamics of the smallest eddies. However, as explained in the previous section, smallest eddies of a flow might be on the order of millimeters whereas the size of the large eddies might be on



the order of kilometers. As a result, resolving all the scales from smallest to largest scales is computationally prohibitive. The number of grid points needed for a 3D DNS simulation is  $N_{3D} = Re_t^{9/4}$ . The overall cost, including time step, of the computational effort is proportional to  $Re_t^3$ . Due to this, DNS is restricted to problems with low Reynolds numbers and simple geometries. DNS requires higher order numerical schemes to resolve the smallest scales and in complex geometries some specific areas such as corners, curvatures etc. are very unfeasible to handle with this method [13].

In addition to the cost of resolving all of the scales in the flow, DNS of scalar transport also needs to resolve the molecular mass boundary layer, of interest here. In those cases the number of grid point goes as  $Sc^3 Re_t^{9/4}$ . Due to the high cost DNS is also limited to low Schmidt numbers ( $Sc$ ).

Advantages of DNS can be summarized as follows:

- The flow field is numerically solved directly from the N-S equations.
- All the spatial scales of the turbulence are resolved by the computational mesh, from the smallest dissipative scales (Kolmogorov scales), up to the largest scales (usually on the order of the domain size).
- DNS does not require any model or parameterization, i.e. all scales of turbulence are resolved.

Disadvantages of DNS can be summarized as follows:

- In DNS, the computational grid must be dense (or fine) enough. Otherwise the smallest features of turbulence will not be described correctly.

- Computational cost of DNS is very high, even at low Reynolds numbers. Consequently, DNS is restricted to moderately turbulent flows. As a result, most of turbulent flows of interest cannot be simulated via DNS.

### 2.1.3.3 Reynolds-Averaged Navier-Stokes Simulation

Instead of solving the Navier-Stokes equations via DNS, one can use statistical methods by applying averaging or filtering procedures to N-S equations. In Reynolds-averaged Navier-Stokes simulation (RANS) of statistically steady flows, time-averaging is used where all the flow properties are separated into their time-averaged and fluctuation components. Therefore, we can decompose flow property  $\psi$  into its mean (average) and fluctuation components as follows

$$\psi = \langle \psi \rangle + \psi' \quad (2.10)$$

where  $\langle \psi \rangle$  is the mean value and  $\psi'$  is the fluctuation.

Time-averaged mean  $\langle \psi \rangle$  is defined as

$$\langle \psi \rangle = \frac{1}{T} \int_t^{t+T} \psi dt. \quad (2.11)$$

where  $T$  must be large compared to time scale of the turbulent fluctuations and much less than the time scale relative to the mean flow. The following rules apply to Reynolds time averaging:

$$\langle \psi' \rangle = 0$$

$$\langle \langle \psi \rangle \rangle = \langle \psi \rangle$$

$$\langle \nabla \cdot \psi \rangle = \nabla \cdot \langle \psi \rangle \quad (2.12)$$

$$\langle \nabla \cdot \nabla \psi \rangle = \nabla \cdot \nabla \langle \psi \rangle$$

$$\langle \int \psi dV \rangle = \int \langle \psi \rangle dV$$

Applying the above averaging rules to continuity, Navier-Stokes, and scalar transport equations, we obtain Reynolds-averaged Navier-Stokes equations. The Reynolds-averaged continuity equation is basically the same as the unaveraged equation in that there are no new terms. However, additional terms arise in the momentum and scalar equations which are known as *Reynolds stresses* and *Reynolds (or turbulent) fluxes*, respectively.

Reynolds stresses are defined as:

$$\tau_{ij} = -\langle u'_i u'_j \rangle \quad (2.13)$$

and Reynolds fluxes are defined as:

$$q_j = \langle \phi' u'_j \rangle \quad (2.14)$$

where  $\phi'$  are fluctuations of the scalar.

We can not compute neither the Reynolds stresses nor the Reynolds fluxes since  $u'_i$  and  $\phi'$  are unknown entities. This is because in the process of Reynolds averaging, these additional terms have been generated but no new equations were obtained to account for these new unknowns. To overcome this closure problem, Reynolds stress tensor and Reynolds fluxes must be modeled in terms of the variables in the Reynolds averaged equations.

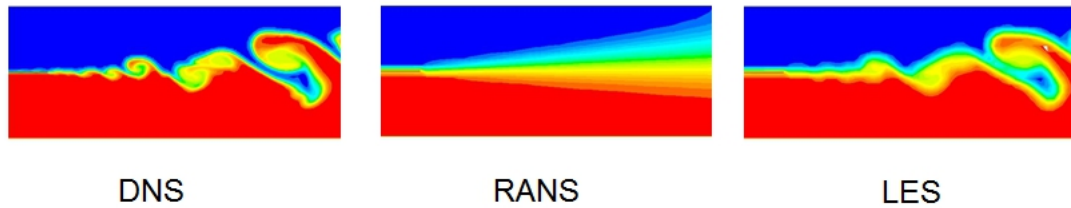


Figure 2.2: Comparison of DNS, LES and RANSS of an interfacial flow. [71] Reprinted with permission from A. Rasheed. Turbulence modeling: Large eddy simulation, web, May 2011. Copyright 2011, A. Rasheed.

Advantages RANSS can be summarized like below:

- RANSS is much cheaper and faster than DNS because we only resolve the largest scales.

Disadvantages RANSS can be summarized like below:

- RANSS is only able to resolve the mean component (i.e. the largest scales) of the flow. The unresolved components are accounted for via a turbulence parameterization or model for the Reynolds stresses and fluxes.
- RANSS is not suitable for detailed turbulence studies. The level of detail is low compared to other methodologies like large eddy simulation (LES) and DNS (See Fig. 2.2).

#### 2.1.3.4 Large Eddy Simulation (LES)

Turbulent flows are characterized by fluctuating velocity fields (See Fig. 2.3). Since these fluctuations can be of small scale and high frequency, they are too computationally expensive to simulate directly. Instead, the governing equations can be manipulated to

remove the smaller scales, resulting in a modified set of equations that are computationally less expensive to solve.

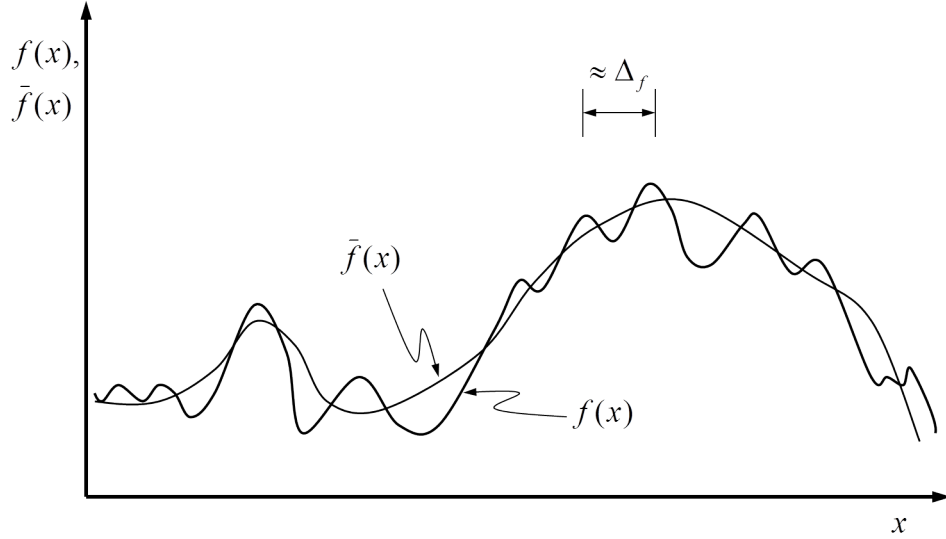


Figure 2.3: Sketch of function  $f(x)$  and its filtered component  $\bar{f}(x)$  where the filter width is  $\Delta_f$ . [85] Reprinted with permission from A. Tejada-Martínez, Dynamic subgrid-scale modeling for large-eddy simulation of turbulent flows with a stabilized finite element method, PhD thesis, Rensselaer Polytechnic Institute, November 2002. Copyright 2002, A. Tejada-Martínez.

In LES, the large scales of turbulence are resolved and the effect of the smaller scales are modeled. To achieve this, a low-pass spatial filter is applied to the Navier-Stokes equations. The filtering process is similar to Reynolds averaging in that flow variables are separated into their resolved and unresolved components. Using a notation similar to that used for the RANSS approach, flow property  $\psi$  is decomposed as

$$\psi = \bar{\psi} + \psi' \tag{2.15}$$

where  $\bar{\psi}$  is the resolved (filtered) component and  $\psi'$  is the residual (subgrid or smaller) component.

A generalized filter is defined by [52]:

$$\bar{\psi}(x,t) = \int_{\Omega} G(x,y)\psi(y,t)dy \quad (2.16)$$

where  $G$  is a filter function.  $G$  is some function which damps the small scales of  $\psi$  on the order of filter width denoted as  $\Delta_f$  (see Fig. 2.3).

Filtering N-S equations leads to governing equations given in terms of resolved components ( $\bar{\psi}$ ) and also generates extra terms similar to the ones obtained by Reynolds averaging. For the momentum equation, these terms are called subgrid-scale (SGS) stresses and denoted by  $\tau_{ij}^{\text{SGS}}$ :

$$\tau_{ij}^{\text{SGS}} = \overline{u_i u_j} - \bar{u}_i \bar{u}_j \quad (2.17)$$

and for scalar equation these terms are known as subgrid-scale (SGS) fluxes and denoted by  $q_j^{\text{SGS}}$ :

$$q_j^{\text{SGS}} = \overline{\phi u_j} - \bar{\phi} \bar{u}_j \quad (2.18)$$

where  $\overline{u_i u_j}$  and  $\overline{\phi u_j}$  terms must be modeled. This is due to the fact that  $\tau_{ij}^{\text{SGS}}$  and  $q_j^{\text{SGS}}$  can not be evaluated without knowledge of  $u_i$  and  $\phi$  and in LES we do not have access neither to unfiltered velocity,  $u_i$  nor to unfiltered scalar  $\phi$ . We need a subgrid-scale model to model the turbulent residual scales which cannot be resolved by the grid and the discretization scheme. This matter will be discussed in detail in Chapter 4. The significance of the SGS stress is that it accounts for the impact of the missing (unresolved) scales on the explicitly computed (resolved) scales.

Note that the SGS stress in LES and the Reynolds stress in RANSS are not the same. "The SGS stress in LES is due to a local average of the complete field, whereas the Reynolds stress in RANSS is due to a time or ensemble average. The SGS energy is a much smaller part of the total flow than the RANSS turbulent energy, so model accuracy may be less crucial in LES than in RANSS computations" [42].

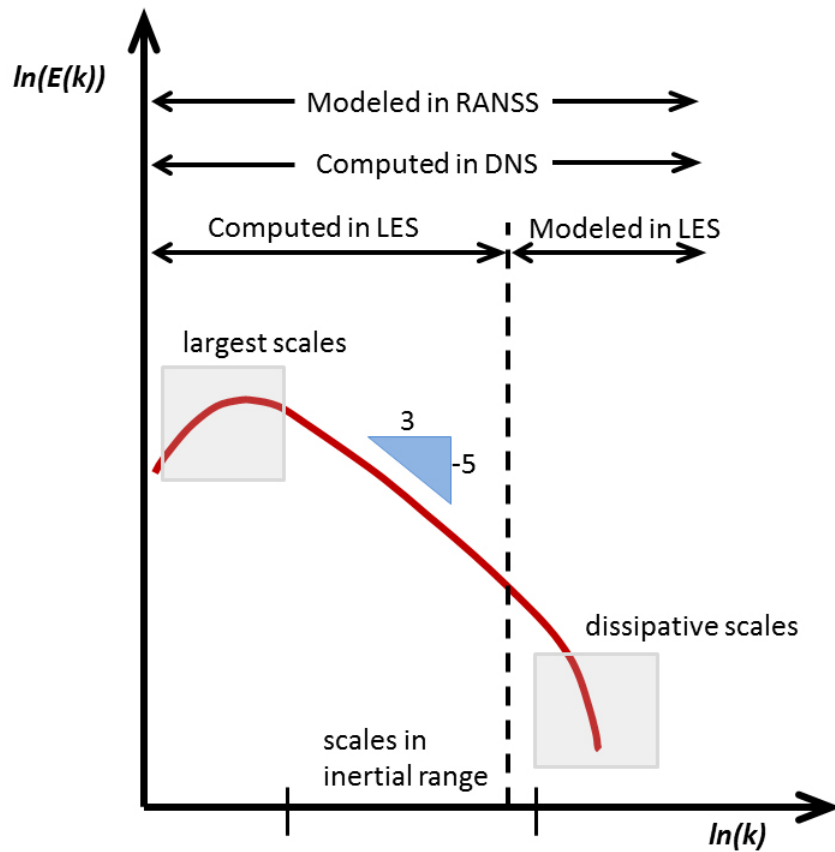


Figure 2.4: A depiction of the observed energy cascade.

As explained previously, in a turbulent flow large eddies contain most of the energy. Also, they are unstable and break up transferring their energy to smaller eddies. These smaller eddies transfer their energy to even smaller eddies and this goes on until energy is dissipated by the smallest eddies. This process is known as energy cascade. We can determine how the turbulent kinetic energy is distributed among the eddies of different

sizes. This is usually done by considering the energy spectrum. A simplified form of an energy spectrum is shown in Fig. 2.4. Energy spectrum can be thought of as being composed of three parts: energy containing range (range for the large, energy containing eddies), the inertial subrange for isotropic scales (independent of the large scales) and the dissipation range (range for small, isotropic, dissipative scales). In DNS, all the scales in the energy spectrum are resolved whereas in RANSS all scales of turbulence are modeled. In LES large scales are solved explicitly while small, dissipative scales are modeled using a subgrid-scale model.

Advantages of LES are summarized below:

- LES is somewhere in between DNS and RANSS in terms of rigor and computational requirement.
- In LES, we only model the small scales. Large scales depend on the mean flow and boundary conditions whereas small scales depend on viscosity and on the rate at which they receive energy from the larger scales. Thus, they are universal and are independent of the geometry of the flow [68]. As a result, the models used to account for small scales can be universal as well (i.e. they maybe applicable to different flow configurations) [29].
- Turbulent flows at higher Reynolds numbers (compared to DNS) can be simulated.

Disadvantages of LES are summarized below:

- Computational requirement for LES is less than DNS, but still it might be too costly for most engineering and geophysical applications [29].



- Although, assumption of small scales being independent of the flow geometry is true for most of the cases, it might cause a problem for boundary layers where small scales are of importance. "*Without explicit modeling of these regions the benefits of LES would be destroyed, since the proximity of the wall defines (some of) the smallest scales in the flow*" [29]. Note that in the computations presented in this work, resolution of molecular boundary layers is required in order to resolve mass transfer at the surface, thus modeling of these boundary layers is not performed. This is the main reason why the present computations are limited to low  $Re$  and low  $Sc$  numbers.

## 2.2 Turbulence in the Upper Ocean

Turbulence processes associated with winds, waves, currents and buoyancy in the ocean cause rapid mixing as well as increased rates of momentum, heat and mass transfer. For this reason, turbulent mixing has a fundamental role in the atmosphere-ocean systems ([39, 47, 89]). In 1938, Langmuir [49] observed that when the wind speed exceeds  $3 \text{ m s}^{-1}$ , lines of foam roughly aligned in the direction of the wind occurred at the water surface. He also showed that these lines occur at the surface convergence of counter-rotating cells causing downwelling of water to depths below (See Fig. 2.5). These cells (referred to as Langmuir circulation or LC) are characteristic of the turbulence (i.e. the Langmuir turbulence) advected by the mean flow. As is the case for the eddies in all turbulent flows, Langmuir cells come in a wide range of spatial and temporal scales.

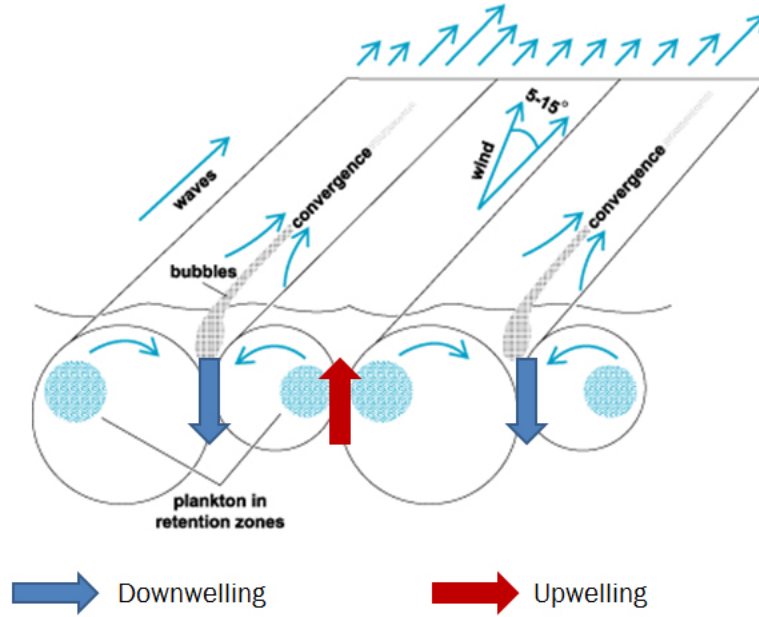


Figure 2.5: Schematized Langmuir circulation patterns.

The typical crosswind length scale of the smallest observed vortices is on the order of several centimeters when the wind begins to blow over a quiescent interface and short capillary waves first appear. The crosswind length scale of the largest vortices reaches up to tens of meters when the wind waves become fully developed and the spectrum of waves includes longer gravity waves. Scott et al. (1969) [75] notes that the smallest LCs (i.e. centimeter-scale LCs) appear briefly during gusts, are poorly defined and coexist with larger LCs (i.e. meter-scale LC). Larger LCs have higher coherency, appear under winds greater than  $3\text{ m/s}$  and have longer life span.

Large scale LC can often be observed in deep water where it extends throughout the surface mixed layer. Recently, Gargett and collaborators [27, 28] observed large scale LC engulfing the entire water column in a shallow coastal shelf region.

LC is formed as a result of the interaction between the Stokes drift velocity and the shear current. Craik and Leibovich [14] derived a mathematical model to account for the

generation mechanism behind LC consisting of a vortex force appearing in the momentum equation parameterizing the interaction between the Stokes drift velocity and the mean shear current. Their work was later supported by laboratory experiments performed by Fallor and Caponi [24]. In the late 1990s, LES of LC in the ocean surface mixed layer using the Craik-Leibovich (C-L) vortex force were performed by Skillingstad & Denbo [77], McWilliams et al. [60] and Skillingstad et al. [76]. Recent studies focused on accounting for the effects of wave breaking [63, 83] and surface buoyancy forcing [54] together with Langmuir circulation (LC).

LES of wind-driven shear current in shallow water with full-depth LC performed by Tejada-Martínez and Grosch [86] and Tejada-Martínez et al. [87] lead to results in good agreement with field measurements of Gargett et al. [28] and Gargett & Wells [27] which were made in a shallow coastal shelf region. In this case the cell extends to the bottom of the water column as previously described. Although the LES was at a lower Reynolds number than that of field observations, the major characteristics of shallow water Langmuir turbulence were captured. For example, LES of full-depth LC was able to predict large-scale features associated with Langmuir turbulence in shallow water consistent with those recorded in the field observations. Moreover, the magnitude of the LES fluctuations obtained via dimensionalization of LES-computed velocity fluctuations with the wind stress friction velocity measured during the field observations of Gargett et al. [28] and Gargett & Wells [27], was in good agreement with those of the field measurements during episodes of LC.

The interested reader may refer to the book chapter by Smith [80] and paper by Thorpe [89] for comprehensive literature review on LC.

### **2.3 Chapter Summary**

In the first part of this chapter, physical and mathematical aspects of turbulence were introduced. Following that, an overview of numerical approaches to turbulence was given where the numerical approach used in this dissertation (large eddy simulation) is also discussed. In the second part, Langmuir turbulence on the ocean was introduced. This type of turbulence and its impact on scalar transport is the focus of this dissertation.

## Chapter 3:

### Boundary Exchange at the Interface

Our main interest is in the impact of the water-side Langmuir turbulence on the transfer of sparingly soluble gases from the air side to water side. As noted earlier, for this type of gases, the transfer is controlled by the water side. Mass transfer occurs when a component in a mixture goes from one point to another driven by a concentration gradient of the component. This process results in a net boundary vertical mass flux at the air-water interface,  $F$ , which can have diffusive and advective components (In our studies, vertical advection at air-water interface is taken as zero assuming non-deforming interface). The main difficulty is in determining the magnitude of this flux due to the nature of the turbulence dynamics that controls the transfer process. Thus, models or parameterizations are used to predict the magnitude of  $F$ . Next, we provide a background for these models. Note that material used in this Section is formed following lecture notes of Socolofsky [81].

#### 3.1 Stagnant Film Model

In order to understand the boundary exchange concept, first consider a stagnant fluid case. We start with the transport equation for concentration ( $C$ ) of a dissolved gas in water and its solution. Since we have an infinite horizontal fluid of uniform thickness,  $\partial C/\partial x = \partial C/\partial y = 0$ . As a result, our transport equation becomes one-dimensional and because the

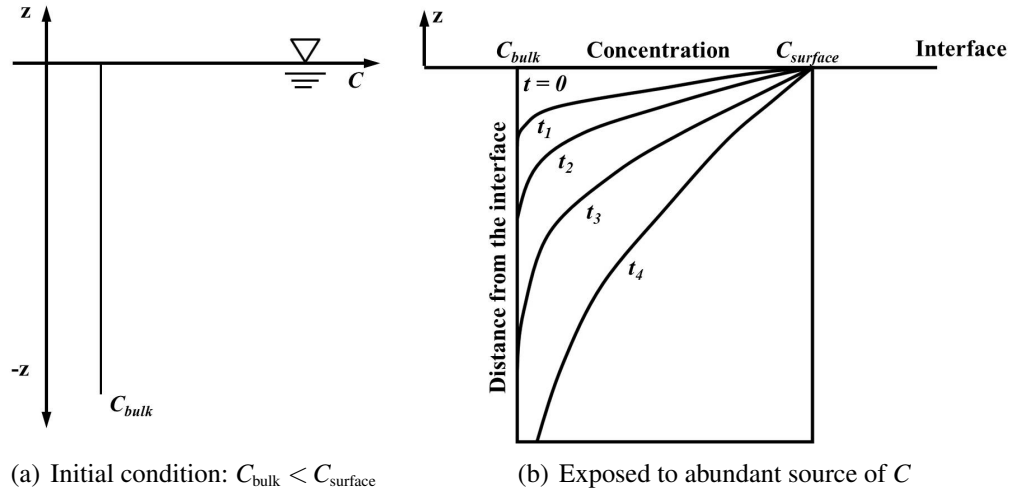


Figure 3.1: Schematic for the boundary exchange for a dissolving substance into a stagnant water body. [81] Reprinted with permission from Y. Socolofsky, Environmental fluid mechanics 1: Mass transfer and diffusion, Lecture Notes, Copyright (2009), Y. Socolofsky.

fluid is stagnant, we can neglect advection. Then, we get the following equation

$$\frac{\partial C}{\partial t} = D \frac{\partial^2 C}{\partial z^2} \quad (3.1)$$

The boundary and initial conditions are:

$$C(-\infty, t) = C_{bulk} \quad (3.2)$$

$$t = 0, z < 0 : C = C_{bulk} \quad (3.3)$$

$$t > 0, z = 0 : C = C_{surface} \quad (3.4)$$

The solution for the boundary conditions above is given by the following equation:

$$\frac{C(z, t) - C_{bulk}}{C_{surface} - C_{bulk}} = 1 - \operatorname{erf} \left( \frac{z}{\sqrt{4Dt}} \right) \quad (3.5)$$

where  $\text{erf}(z)$  is the *error function* defined as

$$\text{erf}(z) = \frac{2}{\sqrt{\pi}} \int_0^z \exp(-z^2) dz \quad (3.6)$$

In Fig. 3.1 we see the concentration profile obtained by this model. Notice that this profile changes with time. Since the transport is governed by molecular diffusion in this case, we can write the flux law as follows

$$F = -D \left. \frac{\partial C}{\partial z} \right|_{z=0} \quad (3.7)$$

Inserting the solution given in Eqn. 3.5 into Eqn. 3.7, we get

$$F(t) = -(C_{\text{surface}} - C_{\text{bulk}}) \sqrt{\frac{D}{\pi t}} \quad (3.8)$$

Thus, for the stagnant case we can write the boundary flux as

$$F = -K(C_{\text{surface}} - C_{\text{bulk}}) \quad (3.9)$$

where  $K$  is the transfer velocity, which in this case is  $K = \sqrt{D/(\pi t)}$ .

### 3.2 Exchange into a Turbulent Water Body

Turbulence causes formation of eddies with different length scales. Below the interface of a water body, these eddies will interact with the mass boundary layer which is defined by boundary layer thickness  $\delta_c$  (See Fig. 1.1).

Turbulent motion will mix the high concentration fluid from the surface region with lower concentration fluid from greater depths generating the bulk region sketched in Fig. 1.1. Vertical turbulent transport weakens as the surface is approached from below. Thus the turbulence does not completely erode the mass boundary layer and thus is not able to extend the bulk region all the way to the surface. Instead, positive vertical turbulent transport of bulk fluid limits the growth of the boundary layer that is promoted by molecular diffusion evidenced by the stagnant case of Section 3.1. An increase in vertical turbulent intensity say by an increase in wind speed brings lower concentration bulk fluid closer to the surface thereby increasing the sharpness of the mass boundary layer and the surface vertical concentration gradient. The latter results in higher diffusion levels in the surface region and thus higher mass flux across the air-water interface. To conclude, turbulent motion in a water body will increase the transfer velocity,  $K$ , and thus lead to an increase in flux,  $F$ . In Chapter 5, we will see how Langmuir turbulence affects this process.

### **3.3 Mass Transfer and Turbulence**

Computation of turbulent mass transport across air-water interface is a significant topic in many areas including chemical and mechanical engineering, geophysical and environmental engineering. Recently, attention of the scientific society has been directed to exchange of greenhouse gases such as  $\text{CO}_2$  between the atmosphere and the oceans because of their importance on global warming [30]. As explained briefly in the previous chapter, measurement of concentration and velocity across the mass boundary layer is very difficult. Due to this fact, parameterizations of mass transfer velocity are used.



In Section 3.3.1, papers focused on computation of turbulence and scalar exchange are reviewed and in Section 3.3.2, the conceptual theories, from which parameterizations of mass transfer velocity rooted, are reviewed.

### **3.3.1 Review of Mass Transfer Computation**

Estimates of ocean flux uptake are derived from parameterizations based on mass transfer velocity and the difference in concentration across the air-sea interface, as reviewed in Chapter 1. There are numerous studies focused on developing parameterizations that are based on commonly measured quantities in the field or via experiments. For instance, in studies by Liss and Merlivat [55], Wanninkhof [94], Wanninkhof and McGillis [96] and Nightingale [62], laboratory and field results are used to propose a transfer velocity based on wind speed. Similarly, Zappa et al. [100] proposed another parameterization that is based on turbulent kinetic energy dissipation, as highlighted in the introduction. Other studies that are based on laboratory and field results include Boutin et al. [7], Jahne et al. [41], Jahne and Haussecker [39].

Besides experimental and field studies, a number of computational studies have also focused on understanding and modeling mass transfer at the air-sea interface. For example Calmet and Magnaduet [10] performed LES simulations for wind driven flows without wave effects (i.e. without Langmuir circulation) and compared their results with different transfer velocity parameterizations. The works of Calmet and Magnaduet [9] and Dong et al. ([22]) are among these in which mass transfer studies are performed with LES. There are also mass transfer investigations performed with DNS such as Banerjee et al. [4], and Debusschere and Rutland [16].

In the present work, we present transfer velocity results from LES and compare them to transfer velocity results that are based on different parameterizations. The work done in this study is similar to work of Calmet and Magnaduet in this aspect. However, the effect of Langmuir turbulence on mass transfer has not been studied neither by them nor by other scientists.

### 3.3.2 Review of Mass Transfer Theories

- **Film theory** - Introduced by Lewis and Whitman [53], film theory is the simplest theory for mass transfer across the air-water interface. It is based on the assumptions that mass transfer occurs in a thin film of thickness  $\delta$  and also that concentration and velocity only change in the vertical direction but not in any other direction or in time. According to this theory, concentration distribution is linear and mass transfer velocity  $K$  can be computed as

$$K = D/\delta \quad (3.10)$$

where  $D$  is the diffusivity.

- **Boundary layer theory** - In boundary layer theory both the concentration and velocity can vary in all three directions. This is in contrast with film theory in which the concentration and velocity vary in the vertical direction only. Furthermore, the change in the concentration profile in the thin film is larger in the vertical direction than in any of the other directions, thus it is sufficient to just consider diffusion in the

vertical direction [3]. As a result of this theory,  $K$  can be computed as

$$K \sim v^{-1/2} D^{2/3} \quad (3.11)$$

- **Penetration theory** - Proposed by Higbie [35], this theory suggests that the boundary layer grows as in the stagnant case until the water in the boundary layer is replaced by low concentration water from below due to the action of turbulent eddies and the same process starts from the beginning. This boundary exchange happens periodically and the renewal frequency between the exchange events is a function of turbulent characteristics of the flow.

In this theory, the boundary layer is allowed to grow like the stagnant case until it is suddenly replaced by the water from below because of the turbulence. We can again determine the net flux using the same governing transport equation and the same initial and boundary conditions used in the stagnant case in Section 3.1. However, since the boundary layer is replaced after some time it started growing, the solution is now valid from  $t = 0$  to  $t = \tau_r$ , the time between renewal events. Then, we can evaluate the mean boundary flux over one cycle by taking the time average:

$$\begin{aligned} \bar{F} &= \frac{1}{\tau_r} \int_0^{\tau_r} F(t) dt \\ &= -\frac{1}{\tau_r} \int_0^{\tau_r} (C_{\text{surface}} - C_{\text{bulk}}) \sqrt{\frac{D}{\pi t}} dt \\ &= -(C_{\text{surface}} - C_{\text{bulk}}) \sqrt{\frac{4D}{\pi \tau_r}} \end{aligned} \quad (3.12)$$

where  $\tau_r$  is a surface renewal time scale . Thus,

$$\bar{F} = -(C_{\text{surface}} - C_{\text{bulk}}) \sqrt{\frac{4D}{\pi \tau_r}} \quad (3.13)$$

and the average transfer velocity is given by

$$\bar{K} = \sqrt{\frac{4D}{\pi \tau_r}} \quad (3.14)$$

- **Surface renewal theory** - Danckwerts [15] improved Higbie's penetration theory.

Higbie assumed that the time a fluid element stays at the surface is the same as all the other fluid elements whereas Danckwerts suggested that fluid elements can remain at the surface for variable times which is more likely to happen in a turbulent environment. In this case, averaging in time, he obtained the following relationship

$$K = \sqrt{\frac{D}{\tau_r}} \quad (3.15)$$

According to surface renewal theory, the surface renewal time scale is modeled or parameterized. Since, the renewal time scale  $\tau_r$  depends on the turbulence, scientists have come up with different parameterizations of  $\tau_r$  based on turbulence characteristics.

For example, if we assume that boundary layer is renewed by near-surface small scale eddies, we can define a  $\tau_r$  characterizing these small eddies. Note that turbulent flow consists of a wide range scales from large ones to small ones. Also, energy

is transferred from larger eddies to smaller eddies. For sufficiently small eddies, molecular viscosity ( $\nu$ ) is effective in dissipating kinetic energy. The rate of turbulent kinetic energy dissipation rate is denoted as  $\varepsilon$ . Thus, given two parameters  $\varepsilon$  and  $\nu$ , we can form a unique time scale for the smallest eddies (Kolmogorov time scale):

$$\tau_r = \sqrt{\frac{\nu}{\varepsilon}} \quad (3.16)$$

As a result, we can obtain an average transfer velocity based on small eddies by inserting this time scale into Eqn. 3.15.

In wind-driven flows without large-scale structures such as LC, the turbulence is shear-dominated. In these cases, the small eddy model given through equations (3.15) and (3.16) has been shown to be successful at predicting surface transfer velocity in computations [10] as well as in field measurements [100]. One of the results of the analysis presented in Chapter 6 is that in flows with large-scale structures such as LC, the small scale eddies as well as the large-scale LC both play important roles in the determining the surface renewal rate.

In Chapter 7 we analyze the small eddy model along with various other models based on surface renewal theory in order to assess how well they capture the effect of LC on transfer velocity. We focus on surface renewal theory because these types of models have been gaining popularity within the oceanography community. These models have gained popularity as they have been recently shown to lead to accurate predictions of transfer velocity via comparisons with transfer velocity measured directly

in the field and in controlled lab experiments representative of the turbulence at the surface of the ocean (see [2, 100]).

### **3.4 Chapter Summary**

This chapter covered a review of mass transfer theories including the commonly used surface renewal theory. In this dissertation, transfer velocity obtained from different parameterizations based on surface renewal theory will be compared with transfer velocity evaluated via LES.

## Chapter 4:

### Turbulent Mass Transport: Computational Methodology

#### 4.1 Governing LES Equations

The Navier-Stokes (N-S) equations are the basic governing equations for laminar and turbulent flows. Interaction between Stokes drift velocity (induced by surface gravity waves) with the shear current (induced by wind) leads to the generation of Langmuir circulation (LC) [89]. The N-S equations are wave-filtered resulting in a vortex force appearing in the momentum equation. This force, known as the Craik-Leibovich (C-L) vortex force, accounts for the generating mechanism of LC without having to directly resolve surface waves [14, 36].

Note that if surface waves are resolved, then the Craik-Leibovich force is not needed to generate LC. Kawamura (2000) [44] performed a low-Reynolds number simulation with resolution of a surface monochromatic wave and a second simulation with the same Reynolds number but with the C-L vortex force and a flat surface. The simulation with the C-L vortex force was characterized by Langmuir cells in good agreement with Langmuir cells present in the simulation resolving the surface wave. Good agreement was seen in terms of the crosswind width of the cells.

#### 4.1.1 Time Filtered N-S Equations (C-L Equations)

The non-dimensional Navier-Stokes equations (augmented by the C-L vortex force) and a scalar transport equation for concentration (of say a dissolved gas) may be written as

$$\frac{\partial u_i}{\partial x_i} = 0 \quad (4.1a)$$

$$\frac{\partial u_i}{\partial t} + \frac{\partial(u_i u_j)}{\partial x_j} = -\frac{\partial \Pi}{\partial x_i} + \frac{1}{Re_\tau} \frac{\partial^2 u_i}{\partial x_j \partial x_j} + \frac{1}{La_t^2} \varepsilon_{ijk} \phi_j^s \omega_k \quad (4.1b)$$

$$\frac{\partial C}{\partial t} + \frac{\partial(Cu_j)}{\partial x_j} + \frac{1}{La_t^2} \phi_j^s \frac{\partial C}{\partial x_j} = \frac{1}{Re_\tau Sc} \frac{\partial^2 C}{\partial x_j \partial x_j} \quad (4.1c)$$

where  $\varepsilon_{ijk}$  is the totally antisymmetric third-rank tensor,  $u_i$  and  $\omega_i$  are the  $i$ th components of the non-dimensional time-filtered velocity and vorticity, respectively. The resolved pressure is denoted as  $\Pi$  and defined as

$$\Pi = p + \frac{1}{2} \Gamma \quad (4.2)$$

where  $p$  is the non-dimensional, resolved pressure and

$$\Gamma = \frac{1}{La_t^4} \phi_i^s \phi_i^s + \frac{2}{La_t^2} u_i \phi_i^s \quad (4.3)$$

Note that C-L vortex force is the last term of Eqn. 4.1b. These equations have been made dimensionless with water column half-depth,  $\delta$ , and friction velocity associated with wind stress,  $u_\tau$  which is defined as  $u_\tau = \sqrt{\tau_w/\rho}$ , where  $\tau_w$  is the wind stress and  $\rho$  is the density of water. Reynolds number,  $Re_\tau \equiv u_\tau \delta/\nu$ , gives a measure of the ratio of inertial forces to



viscous forces and  $Sc$  is the Schmidt number defined as the ratio of momentum diffusivity (viscosity) to mass diffusivity ( $Sc = \nu/D$ ). The turbulent Langmuir number,  $La_t$ , is a ratio of the friction velocity to the Stokes drift velocity which is expressed as  $La_t = \sqrt{u_\tau/u_s}$  where Stokes drift velocity is defined as  $u_s = \omega \kappa a^2$  with  $\omega$  being the dominant frequency,  $\kappa$  being the dominant wavenumber and  $a$  being the dominant amplitude of the surface gravity waves generating LC.  $La_t$  is inversely proportional to the strength of wave forcing relative to wind forcing. Thus a decrease in  $La_t$  results in an increase of wave forcing and thus an increase in the strength of the Langmuir cells generated by the Craik-Leibovich vortex force, as will be shown in Chapter 5.

The non-dimensional Stokes drift velocity is defined by [67] and [50] as

$$\phi_1^s = \frac{\cosh(2(\kappa x_3 + 1))}{2\sinh^2(2\kappa)}, \quad \phi_2^s = \phi_3^s = 0 \quad (4.4)$$

where the  $x_3$  coordinate extends from the bottom of the water column at  $x_3 = -1$  to the surface at  $x_3 = 1$ . In the case there is no dominant amplitude/wavelength/frequency of the wave, the Stokes drift velocity can be computed in terms of the equilibrium displacement spectra for pure wind seas that represent the cumulative effect over some fetch or duration of surface stress due to local wind conditions (see [33]).

Expanding the C-L vortex force which is Stokes drift velocity crossed with the filtered velocity, we can see that the C-L force does not contribute to the  $x_1$  (downwind) momentum equation as the Stokes drift velocity is zero in  $x_2$  and  $x_3$  (cross-wind and vertical) directions. Note that the Stokes drift velocity decays with depth. Waves with shorter wavelength induce a faster decay and thus greater Stokes drift velocity shear. It will be shown in

Chapter 5 that Stokes drift velocity shear plays an important role in determining Langmuir turbulence intensity in the near-surface region of the water column.

### 4.1.2 Spatially Filtered (LES) Equations

In LES, a low-pass spatial filter passes the large scales and cuts off the small scales that are smaller than the filter width (see Fig. 2.3). Applying a low-pass spatial filter to N-S equations leads to

$$\frac{\partial \bar{u}_i}{\partial x_i} = 0 \quad (4.5a)$$

$$\frac{\partial \bar{u}_i}{\partial t} + \bar{u}_j \frac{\partial \bar{u}_i}{\partial x_j} = -\frac{\partial \bar{\Pi}}{\partial x_i} + \frac{1}{Re_\tau} \frac{\partial^2 \bar{u}_i}{\partial x_j^2} + \frac{\partial \tau_{ij}^{\text{SGS}}}{\partial x_j} + \frac{1}{La_t^2} \epsilon_{ijk} \phi_j^s \bar{\omega}_k \quad (4.5b)$$

$$\frac{\partial \bar{C}}{\partial t} + \frac{\partial (\bar{C} \bar{u}_j)}{\partial x_j} + \frac{1}{La_t^2} \phi_j^s \frac{\partial \bar{C}}{\partial x_j} = \frac{1}{Re_\tau Sc} \frac{\partial^2 \bar{C}}{\partial x_j^2} + \frac{\partial q_j^{\text{SGS}}}{\partial x_j} \quad (4.5c)$$

where an overbar denotes application of the low-pass spatial filter and  $\bar{u}_i$  and  $\bar{\omega}_i$  are the  $i$ th components of the dimensionless space and time filtered velocity and vorticity, respectively in the Cartesian coordinate system  $(x_1, x_2, x_3)$ . The dimensionless space and time filtered scalar concentration and pressure are denoted as  $\bar{C}$  and  $\bar{\Pi}$ , respectively.

## 4.2 Subgrid Scale (SGS) Modeling

### 4.2.1 SGS Stress for Momentum Equation

Spatial filtering of momentum equation generates the subgrid-scale (SGS) stress,  $\tau_{ij}^{\text{SGS}}$ , defined as

$$\tau_{ij}^{\text{SGS}} = \bar{u}_i \bar{u}_j - \overline{u_i u_j} \quad (4.6)$$

where  $\overline{u_i u_j}$  terms must be modeled as they cause a closure problem. This is due to the fact that  $\overline{u_i u_j}$  can not be evaluated without knowledge of  $u_i$  and in LES we do not have access to unfiltered velocity,  $u_i$ , as described in Chapter 2. The significance of the SGS stress is that it accounts for the impact of the missing (unresolved) scales on the explicitly computed (resolved) scales.

One can split the SGS stress into deviatoric and isotropic components as follows

$$\tau_{ij}^{\text{SGS}} = \tau_{ij}^{\text{SGS(d)}} + \frac{1}{3} \delta_{ij} \tau_{kk}^{\text{SGS}} \quad (4.7)$$

The deviatoric part is parameterized using Smagorinsky closure and the isotropic part is added to pressure. Deviatoric part of the SGS stress using Smagorinsky closure is given as

$$\tau_{ij}^{\text{SGS(d)}} = 2\nu_T \bar{S}_{ij} \quad (4.8)$$

The eddy viscosity in Eqn. 4.8 is

$$\nu_T = (C_s \bar{\Delta})^2 |\bar{S}_{ij}| \quad (4.9)$$

where  $C_s$  is the dimensionless Smagorinsky coefficient for momentum equation,  $\bar{\Delta}$  is the low-pass filter width,  $|\bar{S}|$  is the norm of the filtered strain-rate tensor,  $|\bar{S}| = (2\bar{S}_{ij}\bar{S}_{ij})^{1/2}$  and  $\bar{S}_{ij}$  is the filtered strain-rate tensor  $\bar{S}_{ij} = (\bar{u}_{i,j} + \bar{u}_{j,i})/2$ . Note that in practice, the low-pass filter used to obtain the filtered equations in Eqn. 4.1 is implicitly set by an undefined combination of the numerical method and the grid discretizing the filtered equations. Thus, typically  $\bar{\Delta}$  is set equal to a characteristic grid-cell size.

## 4.2.2 SGS Flux for Scalar Equation

Spatial filtering of scalar equation generates SGS fluxes,  $q_j^{\text{SGS}}$ , which is defined as

$$q_j^{\text{SGS}} = \overline{Cu_j} - \bar{C}\bar{u}_j \quad (4.10)$$

where  $\overline{Cu_j}$  terms must be modeled because of the closure problem previously described in terms of the SGS stresses. Analogous to the SGS stresses, the SGS fluxes can be modeled as

$$q_j^{\text{SGS}} = -D_T \frac{\partial \bar{C}}{\partial x_j} \quad (4.11)$$

where eddy (turbulent) diffusivity in Eqn. 4.11 is defined as

$$D_T = (C_c \bar{\Delta})^2 |\bar{S}| \quad (4.12)$$

and  $C_c$  is the dimensionless Smagorinsky coefficient for the scalar equation. Coefficients  $C_s$  in Eqn. 4.9 and  $C_c$  4.12 are determined dynamically as described in [86].

Tejada-Martínez and Grosch [86] showed results of Langmuir turbulence in shallow water using LES. In this study, we are expanding these simulations to track the concentration by adding the scalar equation. Our goals are to understand the impact of Langmuir turbulence on near surface scalar or mass transport and test how well parameterizations of transfer velocity account for Langmuir turbulence. Details of numerical method used to solve the previously described equations are given in Appendix A. Equations and variables have been presented in dimensionless form to facilitate presentation of dimensionless

quantities such as  $La_t$  and  $Re_\tau$ . Throughout the rest of this dissertation, all variables will be taken as dimensionless unless specified otherwise.

### 4.3 Geometry of the Flows

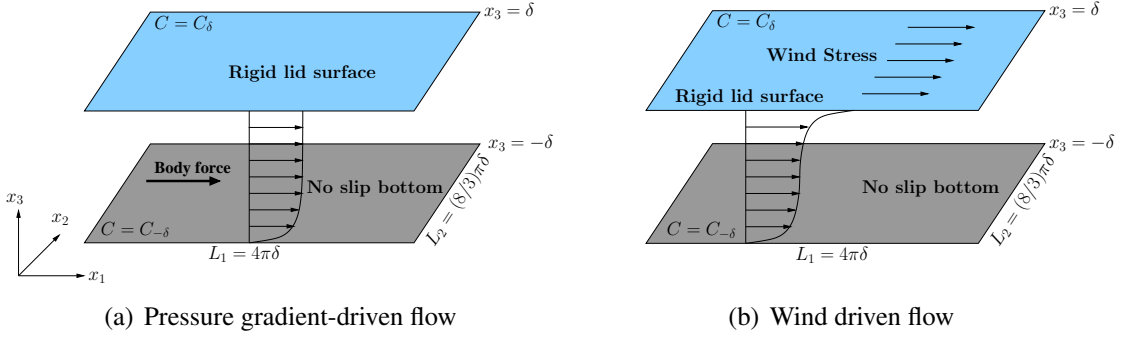


Figure 4.1: Model domain.

In order to understand near-surface scalar transport and test parameterizations of transfer velocity based on the previously described surface renewal theory, LES of wind-driven shallow water flows with and without LC will be performed based on the equations described in Section 4.1. The domains of the flows computed in this study are shown in Fig. 4.1. All flows are characterized by a rigid-lid top surface where zero normal flow is imposed. The flow depicted in Figure 4.1(a) is driven by a constant pressure gradient. Note that pressure gradient is the same as the body force shown in 4.1(a)b. This configuration is typical of a tidal driven flow with small or zero surface wind stress. In wind driven flow (depicted in Figure 4.1(b)) constant wind stress is prescribed at the top surface. No-slip boundary condition is applied at the bottom walls. Also, periodic boundary conditions are set in the horizontal directions ( $x_1$  and  $x_2$ ). This is representative of a continental shelf where there is no shoreline effect. Wind stress is applied at the top surface such that Reynolds number,  $Re_\tau = u_\tau \delta / \nu$ , is 395. The velocities in the  $x_1$  (downwind),  $x_2$

(crosswind), and  $x_3$  (vertical) directions are denoted by  $u_1$ ,  $u_2$ , and  $u_3$ . The domain size in the  $x_1$  and  $x_2$  directions is  $4\pi\delta$  and  $(8/3)\pi\delta$  respectively. Given this crosswind size, the flow domain is expected to be sufficiently wide to be able to resolve one Langmuir cell. In terms of total depth  $H$ , the domain size in the crosswind ( $x_2$ ) direction is  $8\pi H/6 \sim 4H$ , which is within the  $3H$ - $6H$  range of the crosswind length of one Langmuir cell measured by Gargett et al [28]. Dirichlet boundary conditions for concentration are prescribed at the bottom ( $x_3 = -\delta$ ) and at the top ( $x_3 = \delta$ ) with concentration at the top being greater than at the bottom. These conditions are representative of having a fixed reservoir of the scalar on the air side of the air-water interface.

Note that all the simulations were performed on a  $32 \times 64 \times 96$  grid. This grid is uniform in the streamwise ( $x_1$ ) and spanwise ( $x_2$ ) directions. However, in the vertical direction ( $x_3$ ), the grid is highly stretched in order to resolve the details of the momentum and the mass boundary layers near the bottom boundary and the top surface. Details of grid stretching is given in Appendix A.4.

In the following sections, results from (i) pressure gradient-driven flow and (ii) wind driven flow with and without LC are presented. Simulations with full-depth LC are characterized by different values of the turbulent Langmuir number ( $La_t = 1.0, 0.7, 0.4$ ) and the dominant wavelength of surface waves ( $\lambda = 6H, 4H/3$ , where  $H = 2\delta$  is water column depth) used as inputs to the CL vortex force in the momentum equation. Wavelength  $\lambda = 6H$  corresponds to a shallow/intermediate surface wave, and  $\lambda = 4H/3$  corresponds to a shorter (deep water) wave. The case with  $La_t = 0.7$  and  $\lambda = 6H$  is representative of the wind and wave forcing conditions during the full-depth LC field measurements of Gargett et al. [27] and [27]. Wind stress, wind speed, wave amplitude, wave period and frequency

obtained from field measurements are summarized in Table 4.1 [28]. Recall that  $La_t$  is representative of wind forcing relative to wave forcing and the smaller this number is the stronger LC becomes. For example, an increase in wave forcing relative to wind forcing leads to an increase in strength of the cells whereas an increase in wave forcing relative to wind forcing leads to an increase in  $La_t$  and less coherent cells.

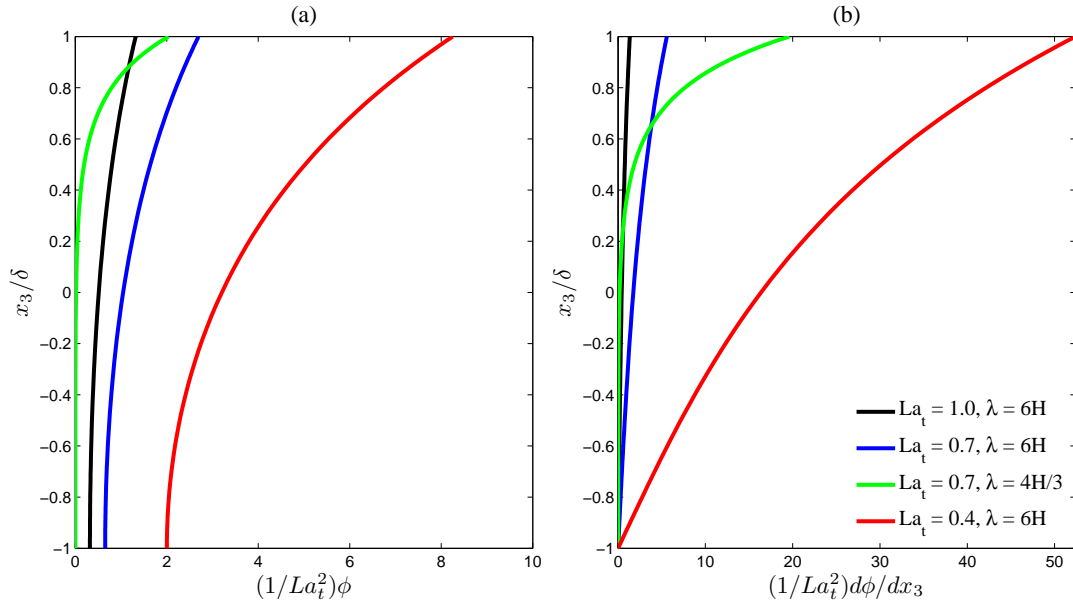


Figure 4.2: (a) Stokes drift velocity and (b) Stokes drift velocity shear.

Table 4.1: Variables obtained from field measurements (See [28]).

Wind stress, $\tau_w$	0.1 N/m <sup>2</sup>
Wind speed, $u_\tau$	7.8 m/s
Amplitude, $a$	1 m
Wave period, $T$	8 s
Frequency, $\omega = 2\pi/T$	0.7854 s <sup>-1</sup>

Fig. 4.2a shows that a smaller value  $La_t$  induces greater Stokes drift throughout the entire water column, thereby increasing the C-L vortex force. Furthermore, waves with smaller  $\lambda$  induce a faster decay with depth of the Stokes drift velocity and thus the C-L

vortex force. Ultimately, a smaller value of  $\lambda$  induces higher Stokes drift shear near the surface (Fig. 4.2b).

#### **4.4 Chapter Summary**

In this chapter the time and space filtered Navier-Stokes equations as well as an introduction to the subgrid-scale models for momentum and scalar equations were provided. Problem domain for the simulations performed were also presented.



## Chapter 5:

### LC Structure and Turbulence Statistics of the Velocity Field

We can decompose a resolved (or LES) variable obtained from the computations into mean and fluctuating components following the Reynolds decomposition. Any LES-resolved variable  $\bar{\phi}$  may be decomposed as

$$\bar{\phi} = \langle \bar{\phi} \rangle + \bar{\phi}' \quad (5.1)$$

where  $\langle \cdot \rangle$  denotes a quantity that is averaged in time and over horizontal directions ( $x_1$  and  $x_2$ ) and  $\bar{\phi}'$  is the resolved fluctuation. This fluctuation denotes the resolved turbulence, and in particular, in flows with LC, this fluctuation corresponds to the resolved Langmuir turbulence.

For a statistically steady flow as is the case for all flows studied here, the mean when taken over a sufficiently long time, is independent of time (See Fig. 5.1).

#### 5.1 LC Structure

Figs. 5.2-5.7 show color maps of instantaneous partially averaged fluctuating velocity components on the  $(x_2, x_3)$ -plane for wind driven flows with and without LC and pressure gradient driven flow, respectively. Partially averaging corresponds to averaging over the downwind direction ( $x_1$ ). Thus, partially averaged fields are functions of  $x_2$  and  $x_3$  (cross-

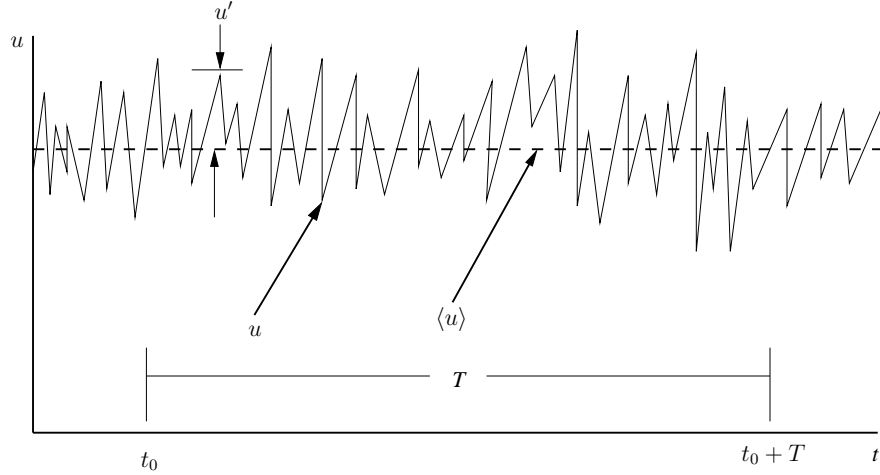


Figure 5.1: Turbulent velocity at a point in a statistically steady flow.

wind and vertical directions) and time. This averaging reveals the secondary (large scale) structures of the turbulence resolved in our flows. The flows with C-L vortex forcing (i.e. the flows with LC) are characterized by a full-depth one-cell structure which corresponds to the resolved full-depth, large scale LC. This large scale LC structure is the largest scale of the resolved Langmuir turbulence. The crosswind width of the large scale LC is equal to the size of the domain in the crosswind ( $x_2$ ) direction ( $8\pi H/6 \sim 4H$ ), where  $H = 2\delta$  is the depth of the water column. This is in agreement with the field observations of Gargett et al [28], who measured the crosswind length of one Langmuir cell in the range  $3H-6H$ . Wind driven flow without LC and pressure gradient-driven flow are characterized by a two-cell structure, but this structure is less coherent than the one-cell structure in the flow with LC.

$\langle \bar{u}'_1 \rangle_{x_1}$ ,  $\langle \bar{u}'_2 \rangle_{x_1}$  and  $\langle \bar{u}'_3 \rangle_{x_1}$  shown in Figs. 5.2-5.7 are partially averaged downwind, crosswind and vertical velocity fluctuations, respectively. In Figs. 5.3c and 5.4c, for wind driven flows with LC, we see that  $\langle \bar{u}'_1 \rangle_{x_1}$  is intensified near the surface and near the bottom while there is no such intensification near the surface in wind driven flow without LC (Fig. 5.6c) and in pressure gradient-driven flow (Fig. 5.7c). In all flows with LC, a region of posi-

tive  $\langle \bar{u}'_1 \rangle_{x_1}$  coincides with a region of negative  $\langle \bar{u}'_3 \rangle_{x_1}$  and vice versa. Furthermore, positive  $\langle \bar{u}'_2 \rangle_{x_1}$  followed by negative  $\langle \bar{u}'_2 \rangle_{x_1}$  generates the surface convergence of the cell (5.3a and 5.4a) which coincides with a downwelling limb (regions of negative  $\langle \bar{u}'_3 \rangle_{x_1}$ ; Figs. 5.3b, 5.4b). Similarly, negative  $\langle \bar{u}'_2 \rangle_{x_1}$  followed by positive  $\langle \bar{u}'_2 \rangle_{x_1}$  generates the bottom divergence of the cell which coincides with an upwelling limbs (regions of positive  $\langle \bar{u}'_3 \rangle_{x_1}$ ). Downwelling and upwelling limbs of the LC are depicted in the sketch shown in Fig. 1.3 in Chapter 1.

Similar to flows with LC, flows without LC (pressure gradient-driven and wind-driven, (Figs. 5.7 and 5.6) are characterized by full-depth streamwise elongated cells. In the case of the wind-driven flow without LC the cells have the same characteristics as Couette cells that occur in flow between parallel no-slip plates moving in opposite directions [65].

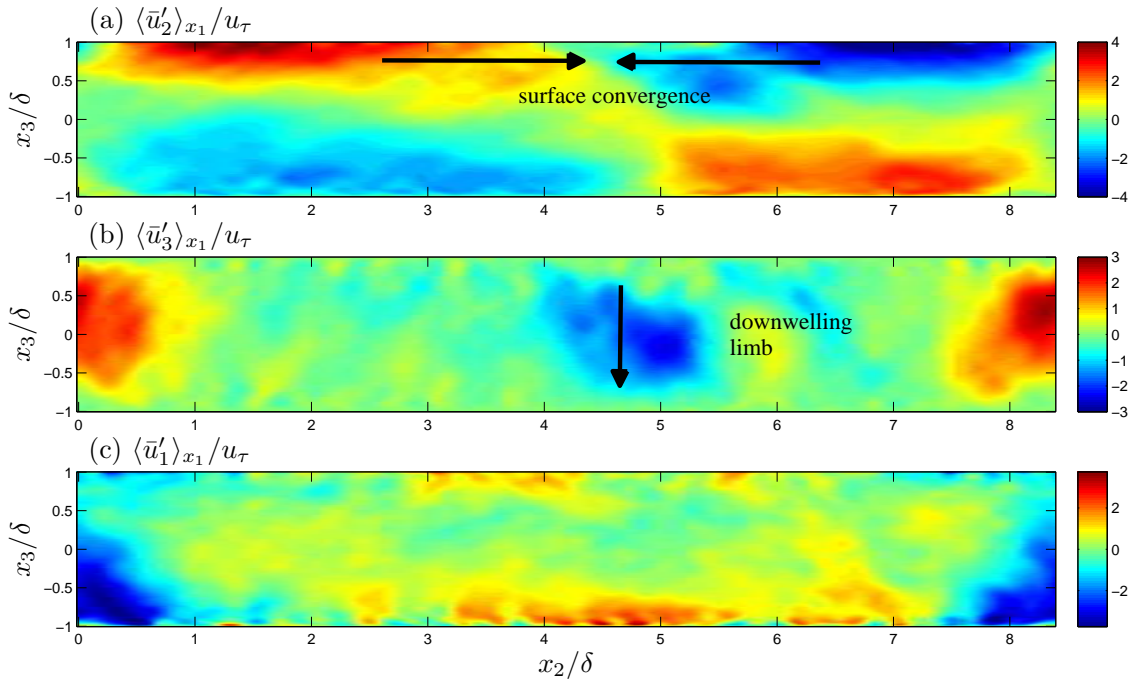


Figure 5.2: Color maps of partially averaged fluctuating velocity components on the  $(x_2, x_3)$ - plane for wind driven flow with LC ( $La_t = 0.4$ ,  $\lambda = 6H$ ).

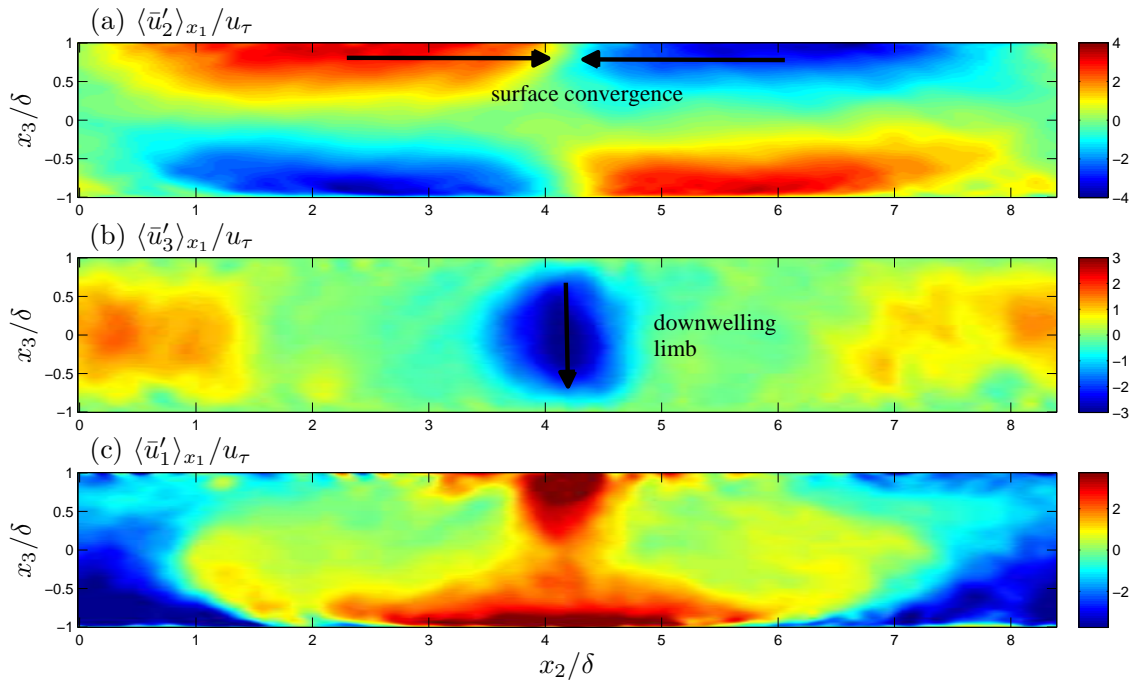


Figure 5.3: Color maps of partially averaged fluctuating velocity components on the  $(x_2, x_3)$ - plane for wind driven flow with LC ( $La_t = 0.7$ ,  $\lambda = 6H$ ).

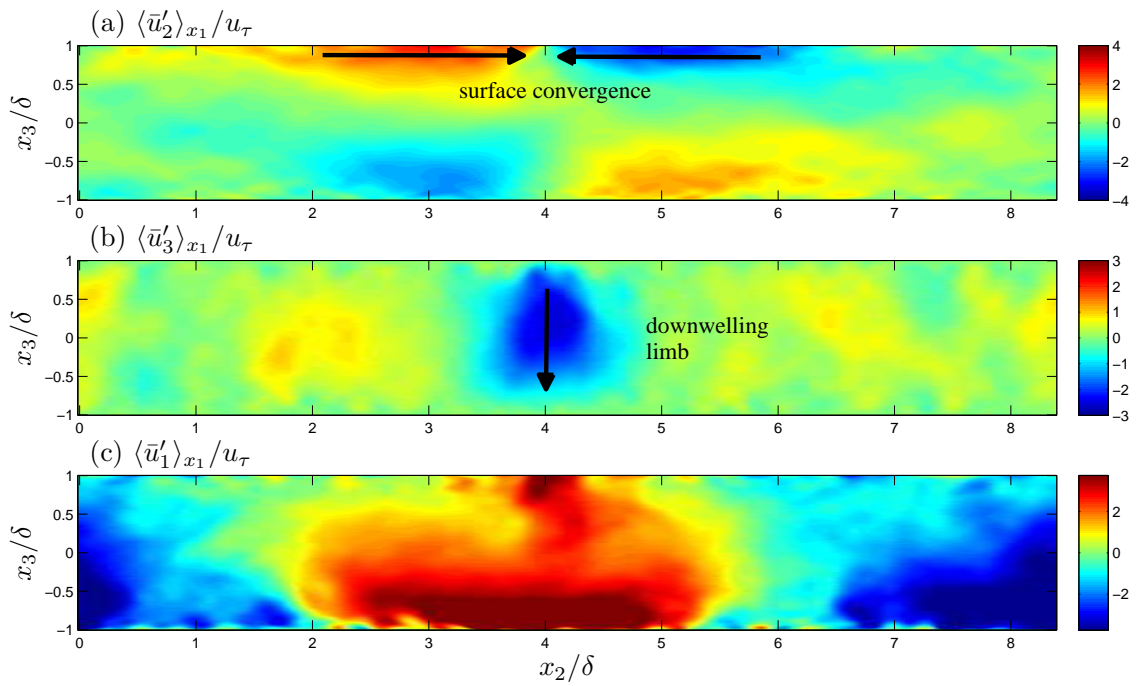


Figure 5.4: Color maps of partially averaged fluctuating velocity components on the  $(x_2, x_3)$ - plane for wind driven flow with LC ( $La_t = 0.7$ ,  $\lambda = 4H/3$ ).

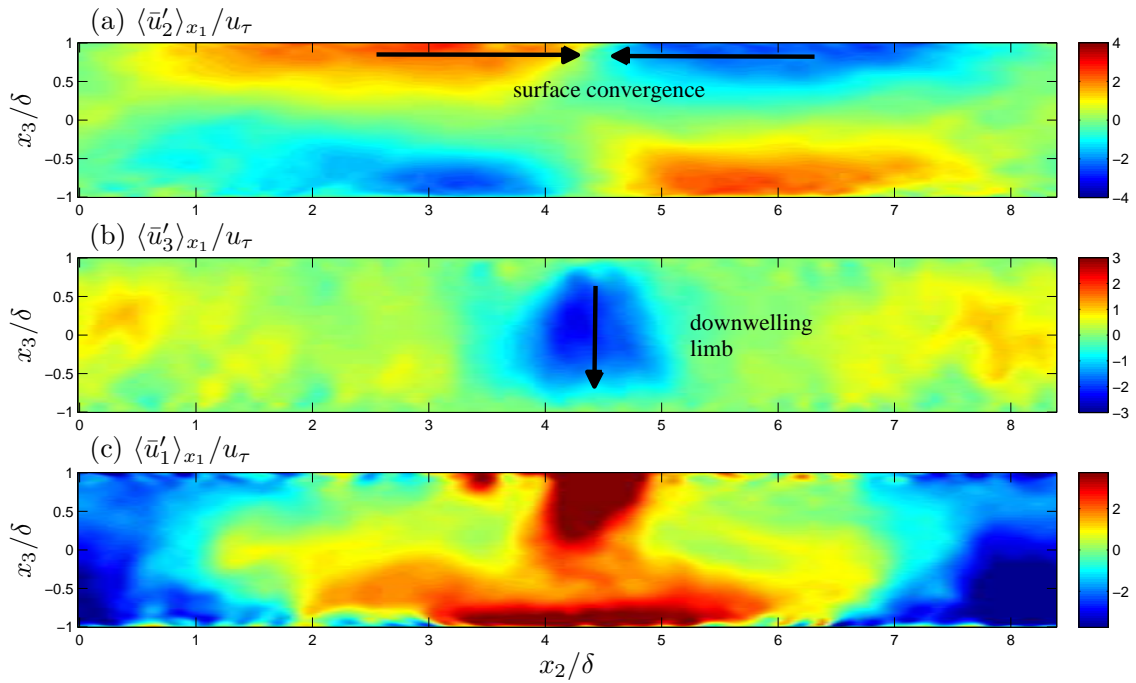


Figure 5.5: Color maps of partially averaged fluctuating velocity components on the  $(x_2, x_3)$ - plane for wind driven flow with LC ( $La_t = 1.0$ ,  $\lambda = 6H$ ).

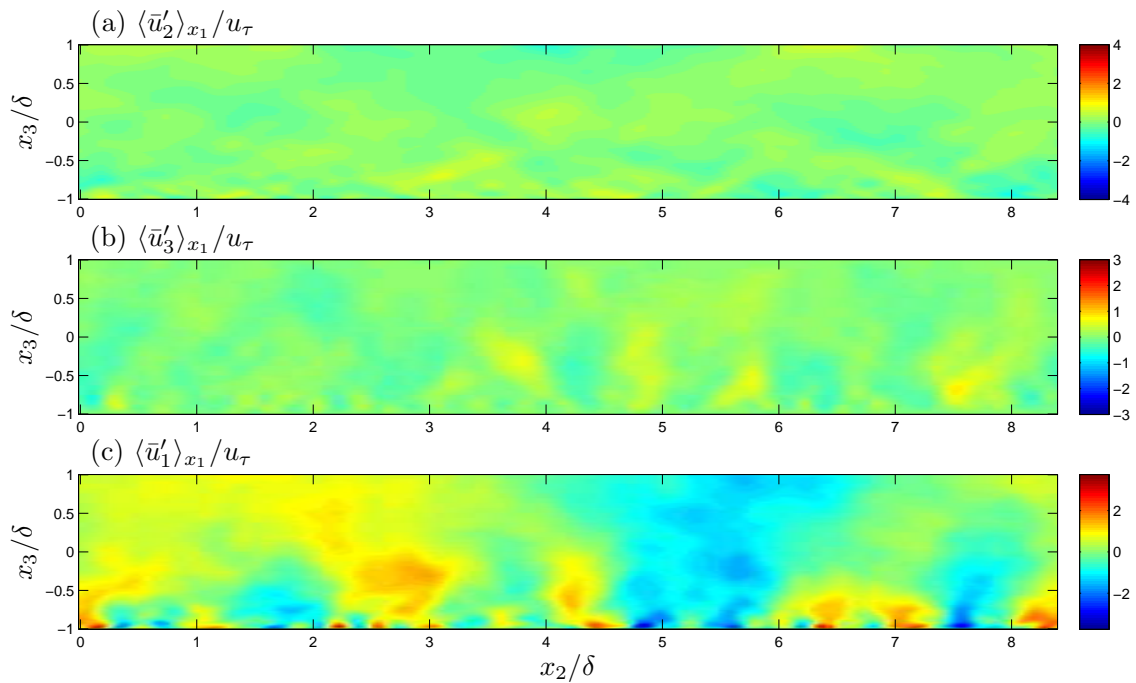


Figure 5.6: Color maps of partially averaged fluctuating velocity components on the  $(x_2, x_3)$ - plane for wind driven flow without LC ( $La_t = \infty$ ).

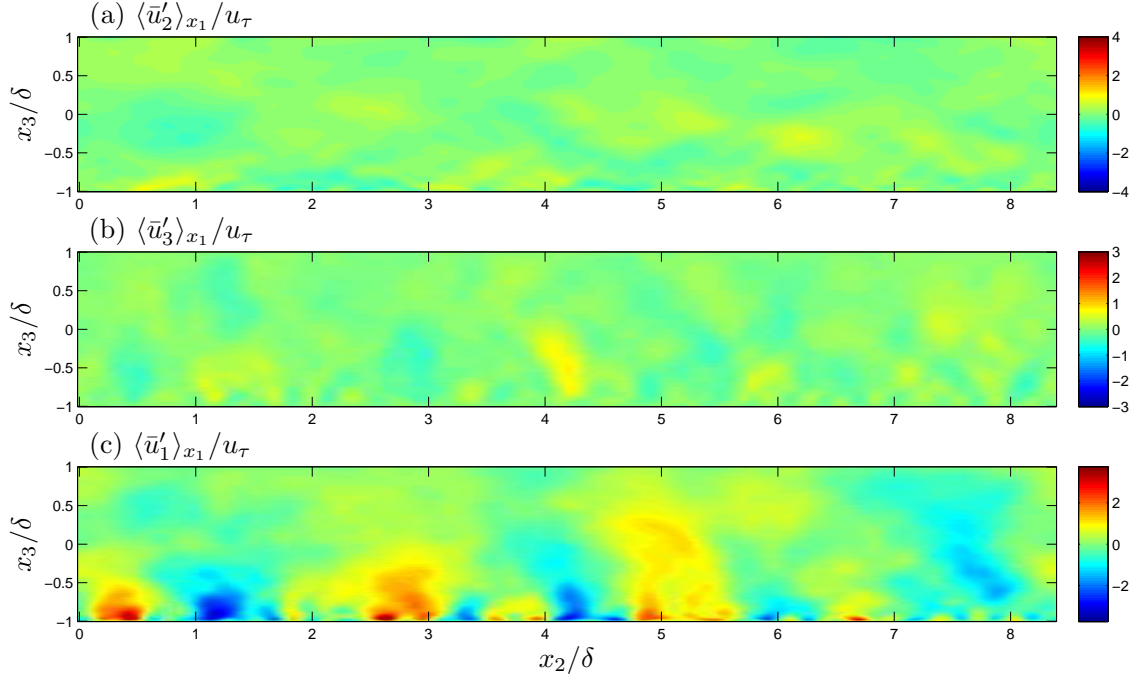


Figure 5.7: Color maps of partially averaged fluctuating velocity components on the  $(x_2, x_3)$ - plane for pressure gradient-driven flow.

For a fixed wavelength of surface waves ( $\lambda = 6H$ ), decreasing turbulent Langmuir number say from  $La_t = 1$  down to  $La_t = 0.7$  results in an intensification of the averaged velocity fluctuations (Figs. 5.3 and 5.5) and thus stronger LC. For a fixed turbulent Langmuir number ( $La_t = 0.7$ ), going from  $\lambda = 6H$  to  $\lambda = 4H/3$  leads to less intense averaged velocity fluctuations weaker in magnitude, especially in terms of crosswind and vertical velocity fluctuations (see Figs. 5.3a, b and 5.4a, b, respectively). This is to be expected because the magnitude of the CL vortex force decays with depth faster for smaller values of  $\lambda$ .

In wind driven flow with LC with  $\lambda = 6H$  and  $La_t = 0.7$ , crosswind velocity fluctuations are stronger than in the flow with  $\lambda = 4H/3$  and  $La_t = 0.7$ . Nevertheless, the latter has a more intense surface convergence zone characterized by a sharper crosswind gradient of crosswind velocity fluctuations when compared to flow with  $\lambda = 6H$  (Figs. 5.3a and 5.4a).

Because of this, downwelling region in flow with  $\lambda = 4H/3$  attains greater fluctuations closer to the surface, as will be seen later in terms of root mean square of vertical velocity.

## 5.2 Mean Profiles

Next, the impact of LC within the near-surface log-layer is analyzed in terms of mean velocity and normal components of resolved Reynolds stress. In flows with LC, as  $La_t$  decreases (i.e. larger wave forcing and more intense LC), the mean velocity profile gets steeper and flattens close to the surface which is consistent with homogenizing action of LC as seen in Fig. 5.8a. Note that in Fig. 5.8a  $u_1^+ = \langle u_1 \rangle / u_\tau$  and in Fig. 5.8b  $x_3^+$  measures distance to the surface in plus units and it is made dimensionless with  $u_\tau$  and  $\nu$  ( $x_3^+ = (u_\tau x_3) / \nu$ ). The horizontal axis in Fig. 5.8b measures  $\log(x_3^+)$ . Mean downwind velocity deficit in the upper half of the water column is shown in 5.8b. Mean downwind velocity deficit is defined as  $(\langle \bar{u}_{\text{surface}} \rangle - \langle \bar{u}_1 \rangle) / u_\tau$  where  $\langle \bar{u}_{\text{surface}} \rangle$  is mean downwind velocity,  $\langle \bar{u}_1 \rangle$ , evaluated at the surface. In the flow without LC the mean downwind velocity deficit follows a log-law whereas in flows with LC mean velocity profiles are deviated from the log-law. LC increases mixing causing smaller near constant deficit (i.e. smaller differences between surface downwind velocity and the downwind velocity at depths below the surface) which eventually leads to the deviation from the log-law. In the flow with LC with  $La_t = 0.7$  and  $\lambda = 4H/3$  disruption of the velocity deficit is more notable than in the flow with LC with  $La_t = 0.7$  and  $\lambda = 6H$  where LC is stronger. This means that disruption of the velocity deficit does not solely depend on the strength of LC, but it also depends on Stokes drift velocity shear. As explained in Chapter 4, shorter wavelength results in greater Stokes drift

velocity shear. This greater shear induces greater vertical velocity fluctuations (Fig. 5.9c, blue and green curves) near the surface and thus greater vertical mixing. This is the reason why velocity deficit is more pronounced in flow with LC with  $La_t = 0.7$  and  $\lambda = 4H/3$  than in flow with LC with  $La_t = 0.7$  and  $\lambda = 6H$ .

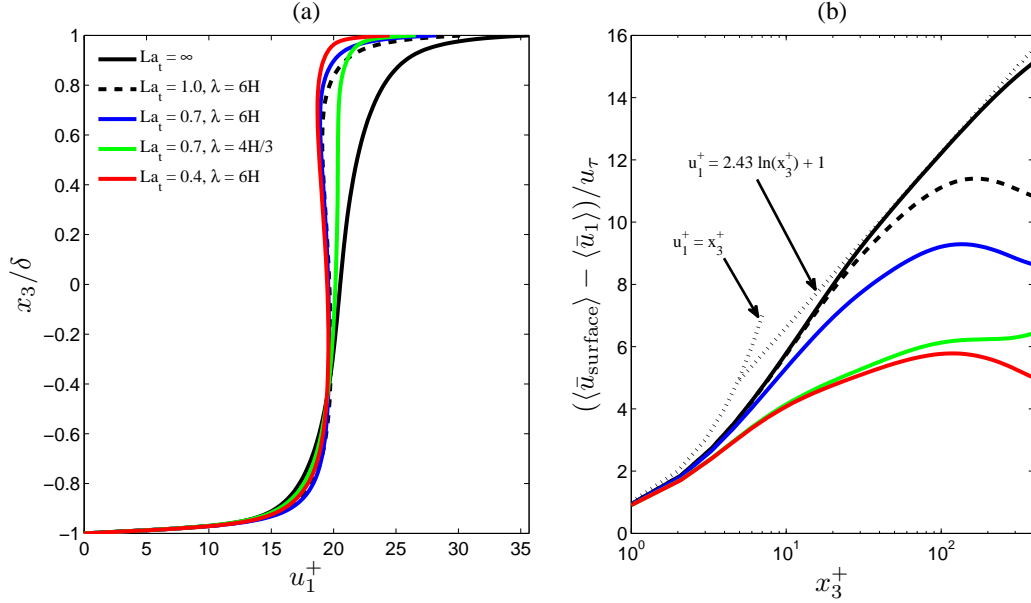


Figure 5.8: Mean downwind velocity (a) and mean downwind velocity deficit in the upper half of the water column (b) in flows with and without LC.

In Fig. 5.9 root mean square (rms) of velocity fluctuations are presented. The rms of velocity fluctuations are computed as  $u_1^{rms} = \sqrt{\langle \bar{u}_1'^2 \rangle}$ ,  $u_2^{rms} = \sqrt{\langle \bar{u}_2'^2 \rangle}$ , and  $u_3^{rms} = \sqrt{\langle \bar{u}_3'^2 \rangle}$  where the brackets denote averaging in  $x_1$ ,  $x_2$  and in time. First thing to note here is that all three rms components of velocity fluctuations are zero at the bottom wall because of the no slip boundary condition. A decrease in  $La_t$  (for a fixed  $\lambda$ ) leads to higher  $u_2^{rms}$  (Fig. 5.9b) in the surface region. These higher values are associated with increasing strength of surface convergence zones of LC as  $La_t$  is decreased. For all wind driven flows with LC,  $u_2^{rms}$  values are more intensified compared to wind driven flow without LC and pressure gradient driven flow. In the upper region,  $u_3^{rms}$  (Fig. 5.9c) increases with decreasing  $La_t$



and also with decreasing  $\lambda$ . The impact of the latter behavior on mean velocity deficit was previously described.

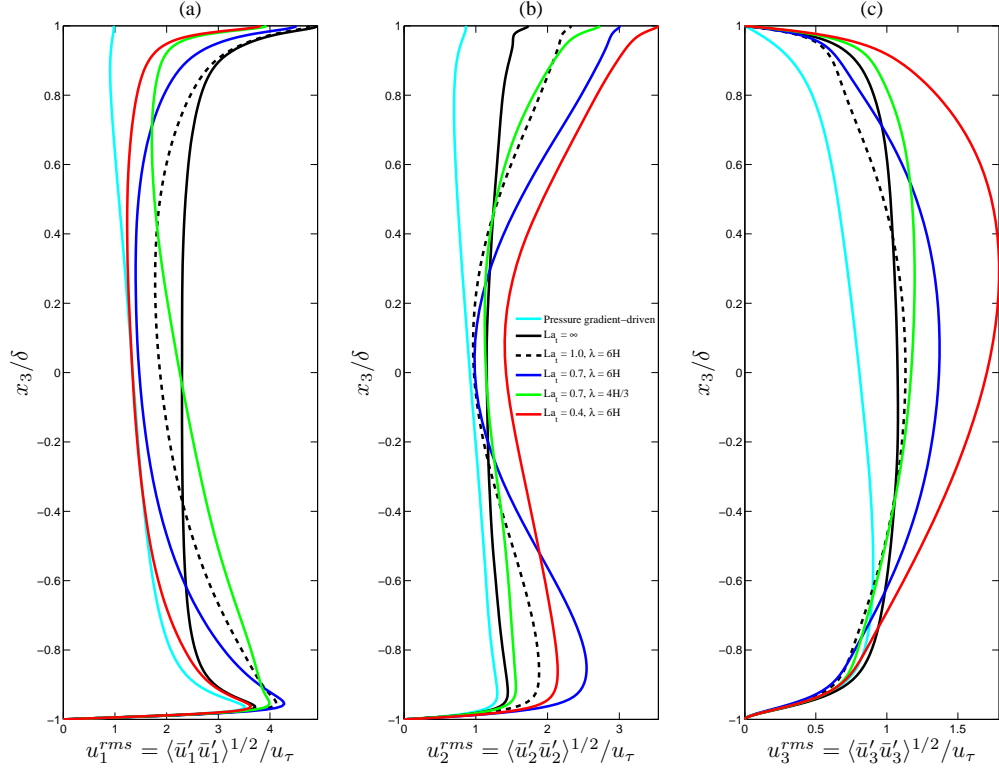


Figure 5.9: Root mean square (r.m.s.) of downwind (a), crosswind (b) and vertical (c) velocity fluctuations.

In Fig. 5.10, normal components of resolved Reynolds stress in flows with and without LC are presented. There are several differences between the pressure gradient-driven flow, wind driven flows with LC and without LC. First, in pressure gradient-driven flow and in wind driven flow without LC the stresses are ordered as  $\langle \bar{u}'_1 \bar{u}'_1 \rangle > \langle \bar{u}'_2 \bar{u}'_2 \rangle > \langle \bar{u}'_3 \bar{u}'_3 \rangle$  throughout the entire water column. In the wind driven flows with LC this ordering changes in the middle and upper half of the water column. For example, in the flow with  $La_t = 0.7$  and  $\lambda = 6H$ , in the middle of the water column  $\langle \bar{u}'_1 \bar{u}'_1 \rangle \approx \langle \bar{u}'_2 \bar{u}'_2 \rangle > \langle \bar{u}'_3 \bar{u}'_3 \rangle$  while towards the upper part of the water column this ordering changes to  $\langle \bar{u}'_2 \bar{u}'_2 \rangle > \langle \bar{u}'_1 \bar{u}'_1 \rangle > \langle \bar{u}'_3 \bar{u}'_3 \rangle$  and at

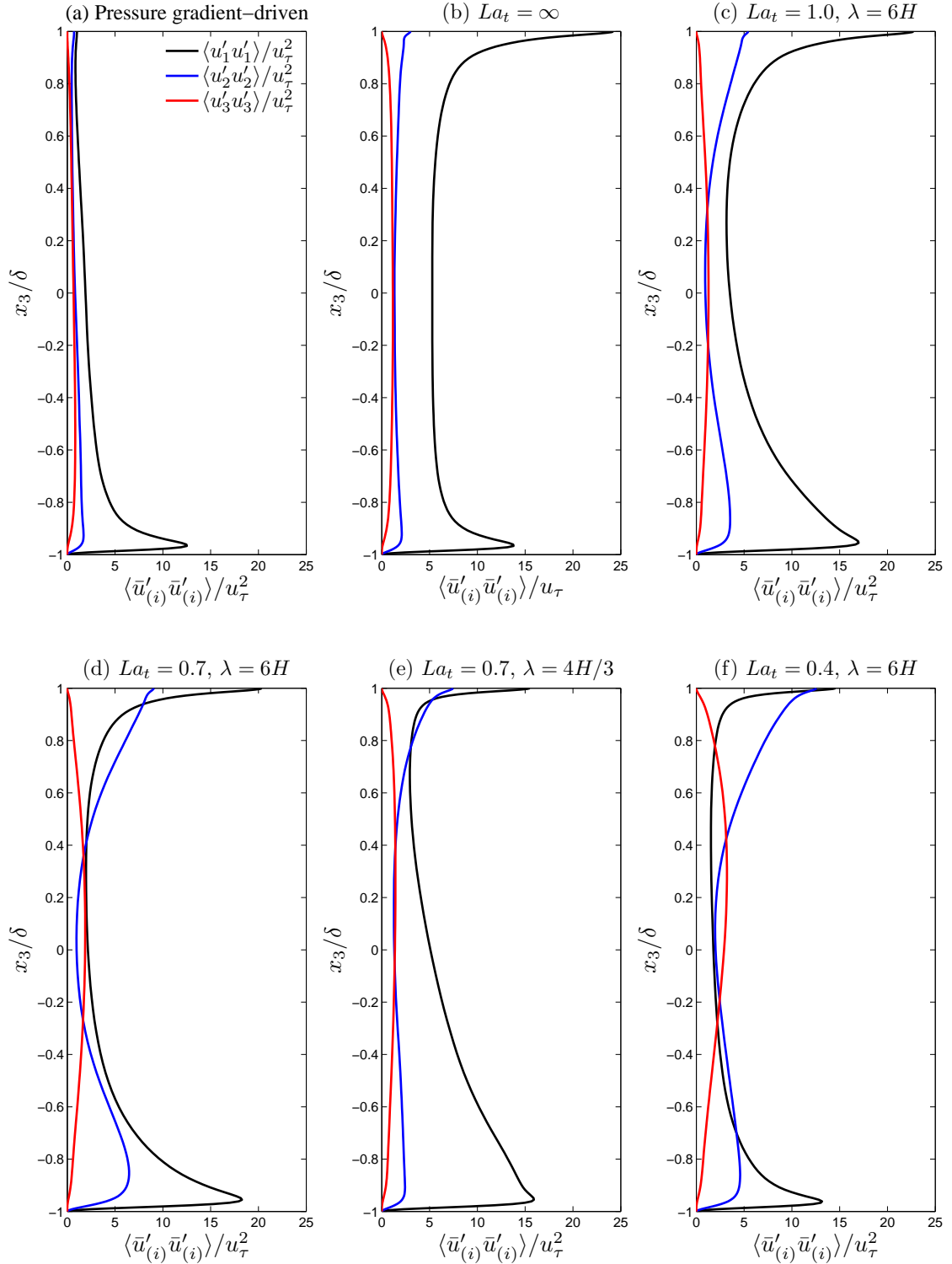


Figure 5.10: Normal components of the resolved Reynolds stress in flows with LC (c-f) and without LC (c-f).

the surface ordering goes back to  $\langle \bar{u}'_1 \bar{u}'_1 \rangle > \langle \bar{u}'_2 \bar{u}'_2 \rangle > \langle \bar{u}'_3 \bar{u}'_3 \rangle$ . This can be attributed to the surface convergence zone of the LES-resolved LC which serves to increase the magnitudes of crosswind velocity fluctuations. Ordering of normal components of resolved Reynolds stress is also changed in wind driven flow with LC with  $La_t = 0.7$  and  $\lambda = 4H/3$ , but near-surface values of crosswind velocity fluctuations are smaller than the flow with  $La_t = 0.4$  and  $\lambda = 6H$ . This is because a decrease in  $\lambda$  leads to less intense averaged velocity fluctuations as explained in Section 5.1.

### 5.2.1 Budgets of $\langle \bar{u}'_i \bar{u}'_i \rangle$

Analysis of TKE budgets have important implications on turbulence parameterizations for RANSS (Reynolds-averaged Navier-Stokes simulation) of the coastal ocean. Coefficients in popular RANSS-based turbulence models are calibrated by constraining them such that model equations satisfy various flow conditions. One of these flow conditions is the existence of a log-layer in the near surface region. As will be shown next in terms of TKE and as was shown earlier in terms of mean downwind velocity deficit, this region is greatly disrupted by the presence of LC. Thus accounting for this near surface effect of LC on RANSS turbulence parameterizations should be addressed in future studies.

Following the Reynolds decomposition,  $\bar{u}_i = \langle \bar{u}_i \rangle + \bar{u}'_i$ , the transport equation for mean resolved turbulent kinetic energy,  $\bar{q} \equiv \langle \bar{u}'_i \bar{u}'_i \rangle / 2$  can be expressed as

$$\frac{\partial \bar{q}}{\partial t} + \langle \bar{u}_k \rangle \frac{\partial \bar{q}}{\partial x_k} = P + L + T + T^{\text{SGS}} + D + A + \epsilon + \epsilon^{\text{SGS}} \quad (5.2)$$

where  $T$  is turbulent transport,  $A$  is pressure transport,  $T^{\text{SGS}}$  is sub-grid scale (SGS) transport,  $D$  is viscous diffusion,  $\varepsilon$  is viscous dissipation,  $\varepsilon^{\text{SGS}}$  is SGS dissipation,  $P$  is mean velocity shear production and  $L$  is production by Stokes drift velocity shear. Definition of these terms are given in Appendix C in table C.1. Using the space and time-dependent numerical solutions of the LES equations in Section 4.1.2, each of the turbulent kinetic energy (TKE) budget terms in Eqn. C.1 were plotted in Fig. 5.12 for flows with and without LC within the surface log-layer.

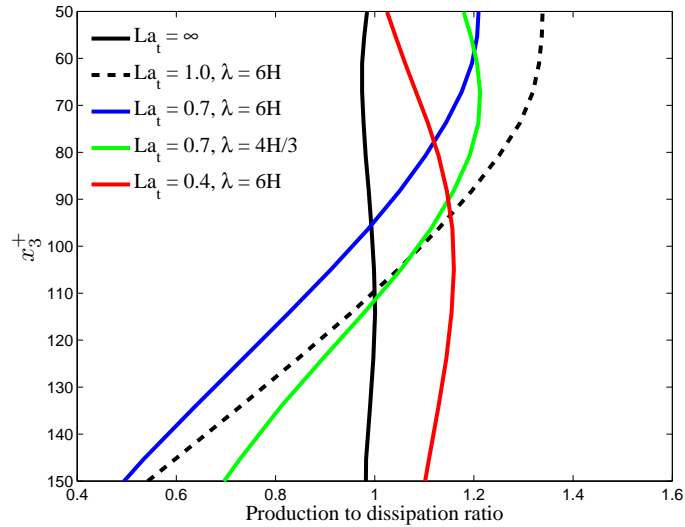


Figure 5.11: Production-to-dissipation ratio in the surface log-layer.

In all flows with LC, production by Stokes drift velocity shear plays an important role (green line). The magnitude of this production term depends on  $\lambda$ , the wavelength of surface waves. Recall that the Stokes drift velocity decays with depth and, furthermore, the decay is faster for shorter wavelengths which results in greater Stokes drift shear. Thus, as expected, in flow with LC with  $La_t = 0.7$  and  $\lambda = 4H/3$ , production by Stokes drift shear reaches higher values than in the flow with the same  $La_t$  but with longer wavelength  $\lambda = 6H$ . In the case of the flow with LC with  $La_t = 0.4$  and  $\lambda = 6H$  (Fig. 5.12e), production

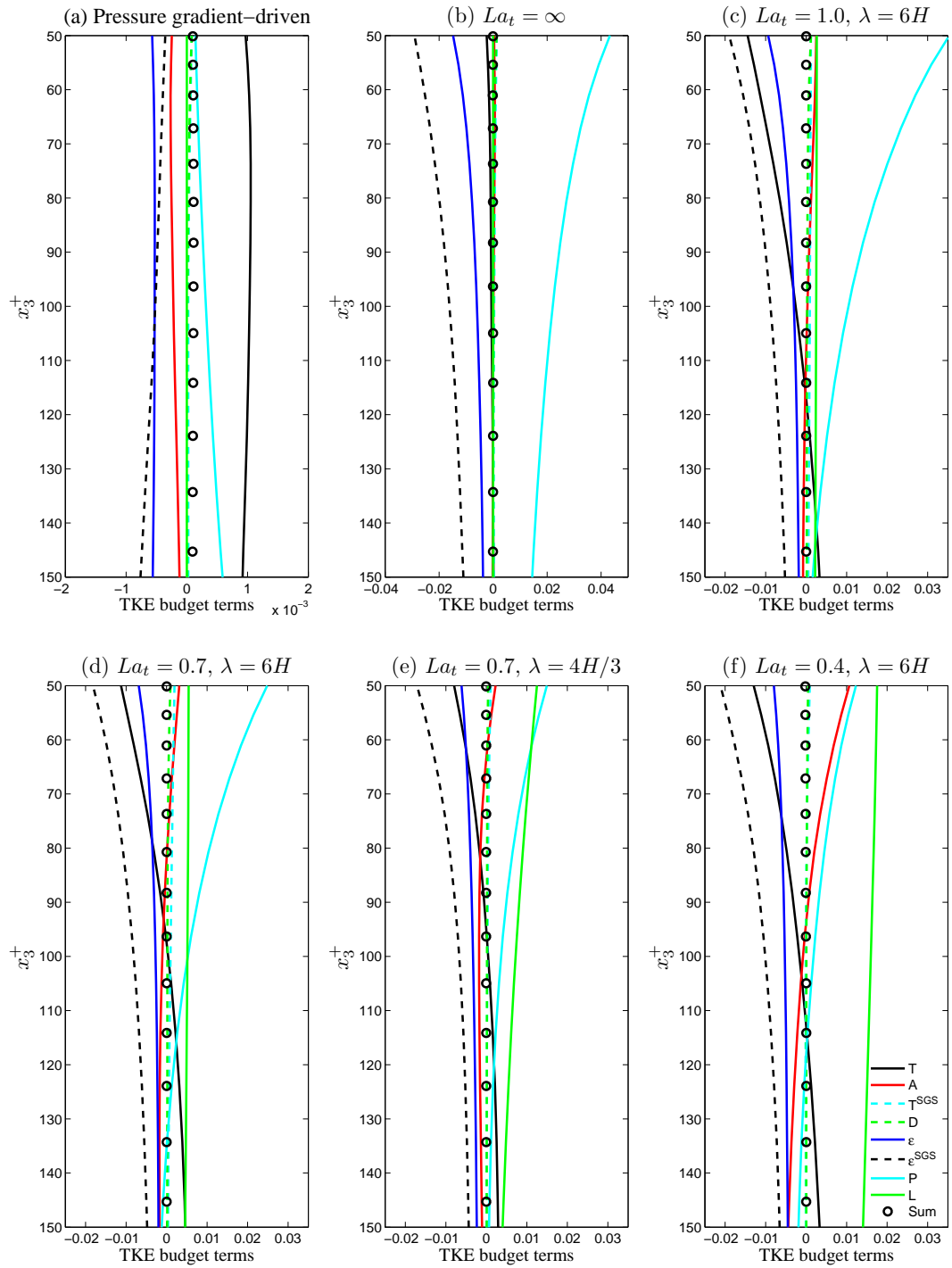


Figure 5.12: Budgets of turbulent kinetic energy scaled by  $u_\tau^2$  in the surface log-layer.

by Stokes drift shear is greater than production by mean velocity shear throughout the entire  $x_3^+$  range shown partly due to the enhanced mixing caused by LC in this flow which serves to diminish velocity shear.

The flow without LC (Fig. 5.12a) is characterized by a well-developed log-layer for which the classical balance between production by mean shear (light blue line) and dissipation holds. In this case dissipation of TKE is caused by viscous (molecular) stress (dark blue line) and also by the subgrid-scale (SGS) stress (black dashed line) described earlier. Balances in flows with LC within the log layer are drastically different than in the flow without LC, as turbulent transport (black line) and pressure transport (light blue line) play non-negligible roles. Consequently, a strict balance between production and dissipation does not occur, as seen in the production-to-dissipation ratios plotted in Fig. 5.11. For the flow without LC this ratio is nearly unity. However, for the flows with LC, the ratios deviate greatly from unity. Also note that the extent of the deviation is independent of the strength of LC. As described earlier, the flow with LC with  $La_t = 0.7$  and  $\lambda = 4H/3$  is characterized by weaker LC than the other two flows with LC studied. However, at depths in the range  $100 < x_3^+ < 60$  the deviation from unity in the production-to-dissipation ratio in the flow with  $La_t = 0.7$  and  $\lambda = 4H/3$  is greater than in the ( $La_t = 0.7, \lambda = 6H$ ) case.

### 5.3 Chapter Summary

Results from LES of wind-driven shallow water flow with full-depth LC have been analyzed in terms of turbulence structure, mean velocity and TKE budgets with emphasis on the near-surface log-layer region of the water column. Wind-driven flows with full-

depth LC are commonly found in shallow coastal shelves undergoing strong wind and wave forcing as evidenced by recent field measurements of Gargett et al. [28] and Gargett & Wells [27].

The present LES revealed that both, the turbulent Langmuir number ( $La_t$ ), inversely proportional to wave forcing relative to wind forcing) and the wavelength ( $\lambda$ ) of surface waves generating LC, play important roles in determining the turbulence structure and overall dynamics. For example, a decrease  $La_t$  led to stronger LC characterized by higher magnitudes of crosswind and vertical velocity fluctuations. The latter are associated with the downwelling and upwelling limbs of LC, and the former are associated with the surface convergence and bottom divergence of LC. A decrease in  $\lambda$  while holding  $La_t$  fixed led to weaker LC.

The presence of LC led to the disruption of surface log-layer dynamics in terms of the mean downwind velocity and production and dissipation rates of TKE. This disruption consisted of deviations from 1. the classical log-law velocity profile and 2. the classical balance between production and dissipation rates of TKE, both exhibited by wind-driven flows without LC in the near-surface region of the water column. It was seen that for a fixed value of  $\lambda$ , a decrease in  $La_t$  gives rise to greater disruption of the near surface log-layer together with stronger LC as previously described. Furthermore, it was also seen that for a fixed value of  $La_t$ , waves of shorter wavelength (i.e. smaller  $\lambda$ ) can lead to greater disruption of the near surface log-layer attributed to an increased production rate of TKE by Stokes drift shear, in spite of weaker LC.

## Chapter 6: Scalar Transport

### 6.1 LC Structure and Scalar Transport

As described earlier, the Navier-Stokes equations are solved together with a transport equation for the concentration of passive scalar (say the concentration of dissolved  $\text{CO}_2$  in water). Dirichlet boundary conditions for concentration are prescribed at the bottom ( $x_3 = -\delta$ ) and at the top ( $x_3 = \delta$ ) with concentration at the top being greater than at the bottom. These conditions are representative of having a fixed reservoir of the scalar on the air side of the air-water interface.

In all flows with LC, downwind-averaged vertical velocity fluctuations (Fig. 6.1, panels on left) are strongly negatively correlated with downwind-averaged scalar concentration fluctuations (Fig. 6.1, panels on right). For example, downwelling limbs coincide with regions of positive scalar concentration and vice-versa. Recall that Dirichlet boundary conditions for the scalar have been specified such that the concentration at the surface ( $C_\delta$ ) is greater than the concentration at the bottom ( $C_{-\delta}$ ). Thus, downwelling limbs transport high-concentration scalar fluctuations from the surface towards the bottom resulting in full-depth regions of positive concentration fluctuations coinciding with the the full-depth downwelling limbs. Similarly, upwelling limbs transport low-concentration scalar fluctuations from the bottom towards the surface resulting in full-depth regions of negative scalar



fluctuations coinciding with the full-depth upwelling limbs. Note that in these figures, concentration fluctuations have been scaled with  $C_{\text{ref}} = C_{\delta} - C_{-\delta}$ .

As explained in Chapter 5, the cells in the flows without LC are characterized by weak downwind averaged vertical velocity fluctuations relative to the corresponding fluctuations in flows with LC and thus are less coherent than LC. Ultimately, the weaker cells play a less significant role in transporting the scalar compared to LC. Instead, in flows without LC, scalar transport near the surface is dominated by small eddies as will be explained in the next section.

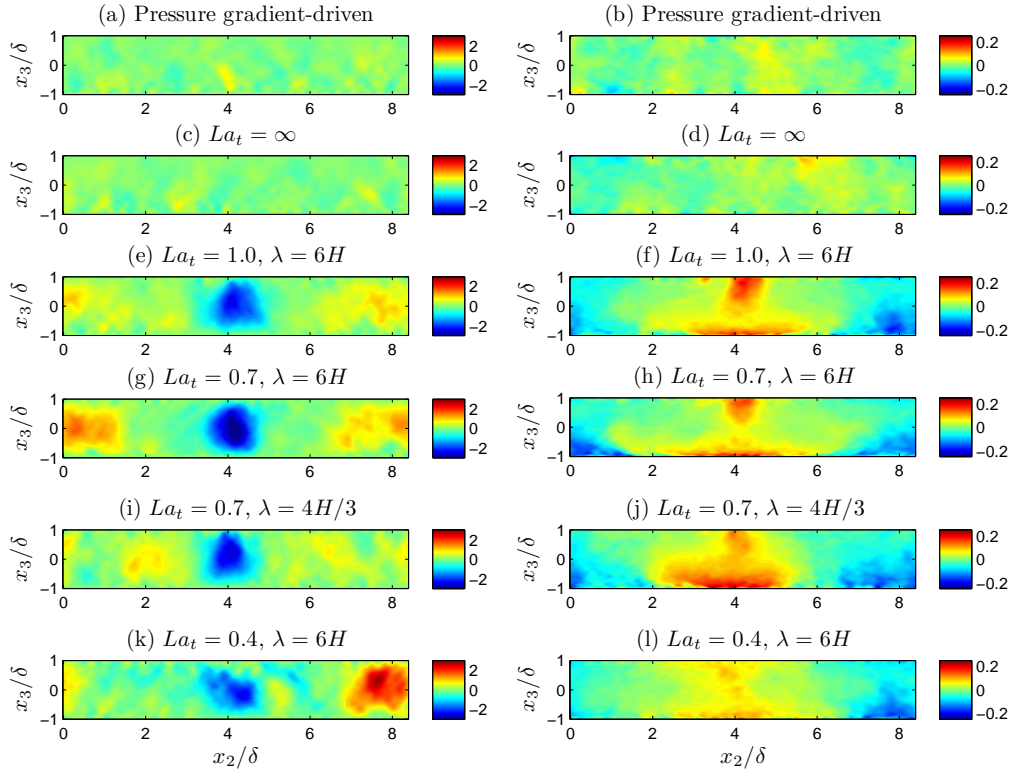


Figure 6.1: Color maps of partially averaged fluctuating vertical velocity components  $\langle \bar{u}'_3 \rangle_{x_1} / u_{\tau}$  on the left and concentration fluctuations  $\langle \bar{C}' \rangle_{x_1} / C_{\text{ref}}$  on the right on  $(x_2, x_3)$ -plane for all flows simulated.

Using Reynolds decomposition in Eqn. 5.1, the resolved vertical turbulent scalar flux can be computed as  $\langle \bar{C}' \bar{u}'_3 \rangle$ . Fig. 6.2a shows that for a fixed value of wavelength of surface

waves  $\lambda$ , decreasing  $La_t$  (decreasing surface wave forcing relative to wind forcing) leads to an increase in vertical scalar flux. Recall that a decrease in  $La_t$  with fixed  $\lambda$  leads to an increase in the strength of LC, as described earlier.

Vertical flux of concentration fluctuations is not solely a function of strength of LC but also a function of  $\lambda$  which is associated with Stokes drift velocity shear. A decrease in  $\lambda$  with fixed value of  $La_t$  also leads to an increase in vertical flux of concentration fluctuations. This can be seen by comparing the cases with  $La_t = 0.7$  and  $\lambda = 6H$  and  $\lambda = 4H/3$ , respectively, in Fig. 6.2a.

As noted earlier, the decay of Stokes drift velocity with depth is inversely proportional to the wavelength of surface waves. Thus, shorter wavelengths induce greater Stokes drift shear near the surface. The increase in Stokes drift shear near the surface serves to enhance vertical fluctuations in that region (see Fig. 6.2b) which ultimately leads to an increase in turbulent vertical scalar flux throughout the entire water column.

As previously analyzed (See Chapter 5), the Langmuir turbulence is characterized by large-scale full-depth LC. A triple decomposition of resolved fields may shed light to how this large-scale LC structure interacts with the smaller scales of the Langmuir turbulence and affect scalar transport. The triple decomposition is defined as

$$\bar{\phi} = \langle \phi \rangle + \underbrace{\langle \bar{\phi} \rangle'_{t,x_1}}_{=\bar{\phi}'} + \bar{\phi}'' \quad (6.1)$$

In flows with LC the fluctuation  $\bar{\phi}'$  corresponds to the resolved Langmuir turbulence. Here the fluctuation  $\bar{\phi}'$  has been decomposed into a time/downwind-averaged component,  $\langle \bar{\phi} \rangle'_{t,x_1}$ , plus the remainder  $\bar{\phi}''$ . The time/downwind-averaged component is characterized

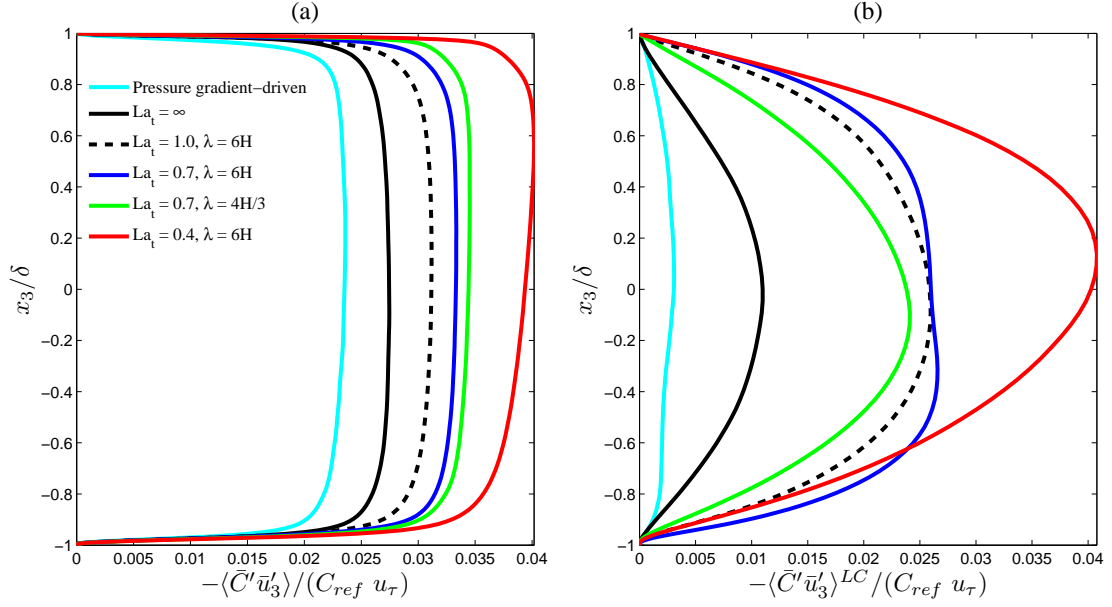


Figure 6.2: (a) Resolved turbulent vertical scalar flux, (b) contribution to resolved turbulent vertical scalar flux from full-depth large-scale streamwise vortices (i.e. full-depth LC in wind driven flows with LC).

by the downwind coherent LC structure analyzed earlier in Figs. 5.2-5.5. The contribution of full-depth LC to the resolved turbulent vertical scalar flux can be computed by employing the triple decomposition in Eqn. 6.1 and expressing the flux as

$$\langle \bar{C}' \bar{u}'_3 \rangle = \langle \bar{C}'' \bar{u}''_3 \rangle + \langle \langle \bar{C}' \rangle_{t,x_1} \langle \bar{u}'_3 \rangle_{t,x_1} \rangle + \langle \langle \bar{C}' \rangle_{t,x_1} \bar{u}''_3 \rangle + \langle \langle \bar{u}'_3 \rangle_{t,x_1} \bar{C}'' \rangle \quad (6.2)$$

where the contribution due to full-depth LC is defined as

$$\langle \bar{C}' \bar{u}'_3 \rangle^{LC} = \langle \langle \bar{C}' \rangle_{t,x_1} \langle \bar{u}'_3 \rangle_{t,x_1} \rangle \quad (6.3)$$

This quantity serves as a measure of coherency between concentration fluctuations and vertical velocity fluctuations (i.e. downwelling and upwelling limbs of LC) observed in Fig. 6.1. Comparing Figs. 6.2a and b, for the flows with LC with  $(La_t = 0.7, \lambda = 4H/3)$

and ( $La_t = 0.7$ ,  $\lambda = 6H$ ), it can be seen that decreasing  $\lambda$  while holding  $La_t$  fixed leads to an increase in  $\langle \bar{C}'\bar{u}'_3 \rangle$  and a decrease in  $\langle \bar{C}'\bar{u}'_3 \rangle^{LC}$ . The latter behavior is as expected given that decreasing  $\lambda$  while holding  $La_t$  fixed leads to a weakening of the full-depth LC structure. Thus, the increase in  $\langle \bar{C}'\bar{u}'_3 \rangle$  is purely due to the enhancement of vertical velocity fluctuations associated with the greater Stokes drift shear induced by shorter waves (smaller values of  $\lambda$ , see Fig. 6.3b). Furthermore, decreasing  $La_t$  (decreasing surface wave forcing relative to wind forcing) for a fixed value of wavelength of surface waves  $\lambda$ , leads to an increase in  $\langle \bar{C}'\bar{u}'_3 \rangle$  and  $\langle \bar{C}'\bar{u}'_3 \rangle^{LC}$ , the latter associated with stronger coherency between downwelling and upwelling limbs of LC and the downwind-averaged scalar concentration fluctuations seen in Fig. 6.1.

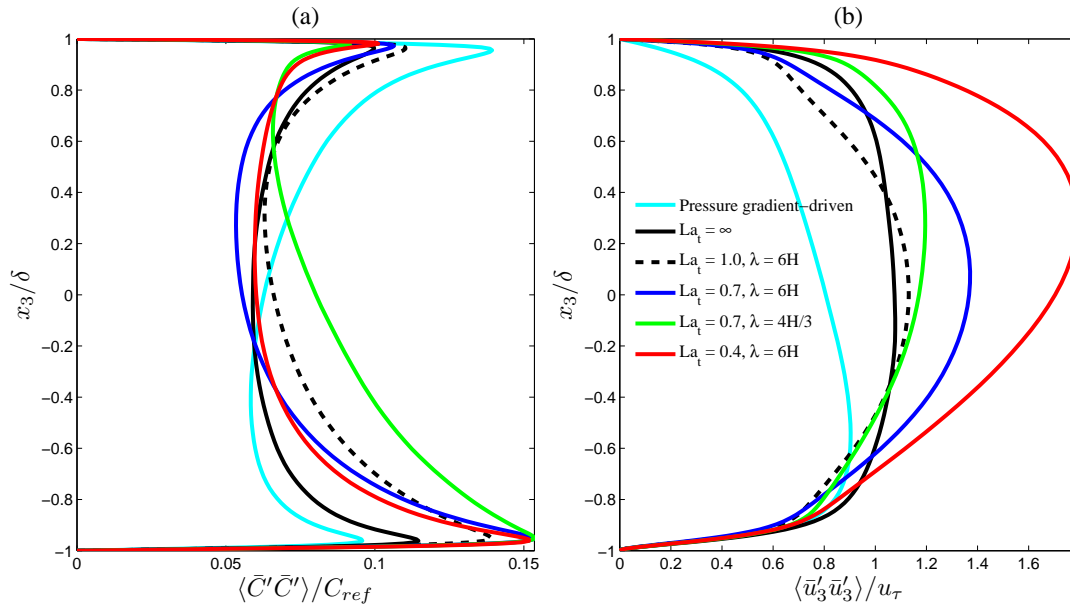


Figure 6.3: (a) Root mean square of (a) resolved scalar concentration and (b) resolved vertical velocity.

Root mean squares (rms) of concentration are shown in Fig. 6.3. Relative to the pressure gradient-driven flow, all wind-driven flows possess higher peaks of concentration rms in the bottom portion of the water column and lower peaks near the surface. Notice

that the near-surface rms of concentration profile for the  $La_t = 0.7$ ,  $\lambda = 4H/3$  case resembles that for the  $La_t = 0.4$ ,  $\lambda = 6H$ , the former influenced by strong near-surface Stokes drift shear and the latter influenced by the strength of LC as described earlier. Meanwhile, the near-bottom rms of concentration profile for the  $La_t = 0.7$ ,  $\lambda = 4H/3$  flow resembles that of the  $La_t = 1$ ,  $\lambda = 6H$  flow, both of which are characterized by weak LC relative to the  $La_t = 0.4$ ,  $\lambda = 6H$  and  $La_t = 0.7$ ,  $\lambda = 6H$  cases.

## 6.2 Near Surface Scalar Transport

In all wind-driven flows, the near-surface region is characterized by small scale stream-wise vortices. The small-scale vortices can not be seen in the downwind-averaged velocity fluctuations in Fig. 6.1. However, they can be seen in instantaneous snapshots of velocity fluctuations without averaging. In Fig. 6.4 small-scale downwells and upwells corresponding to near-surface small streamwise vortices are seen embedded in the near-surface region of full-depth downwelling and upwelling limbs of LC. Fig. 6.5 shows a zoomed-in view of the near-surface small vortices in terms of vertical velocity fluctuations.

In wind driven flows with LC, the strength of the near-surface small scale streamwise vortices depends on  $La_t$  and  $\lambda$ . Fig. 6.5 shows that the intensity of the downwelling and upwelling limbs of the near-surface vortices increases with decreasing  $La_t$  for a fixed  $\lambda$  and vice-versa. Small near-surface vortices in flows simulated with ( $La_t = 0.6$ ,  $\lambda = 4H/3$ ) and ( $La_t = 0.4$ ,  $\lambda = 6H$ ) possess the most intense downwelling and upwelling limbs relative the other flows simulated. Transport of scalar concentration fluctuations is correlated with the downwelling and upwelling limbs of the small-scale vortices, especially in the wind-driven

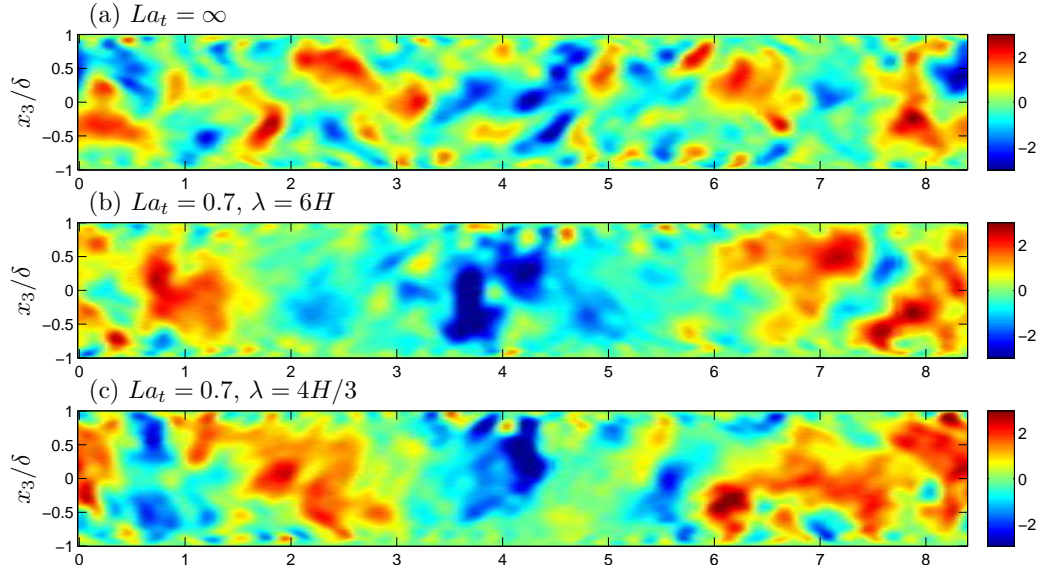


Figure 6.4: Instantaneous snapshots of vertical velocity fluctuations at  $x_1 = L_1/2$ , where  $L_1$  is the downwind length of the domain in wind-driven flows.

flow without LC. For example, downwelling limbs generally take positive concentration fluctuations from the surface to depths below. However, in flows with LC, the signature of full-depth LC appears near the surface through the instantaneous scalar concentration fluctuations (Fig. 6.5). In the mid-span region of the domain, the near-surface small-scale downwells and upwells are not well-correlated with concentration fluctuations. Instead, the full-depth downwelling limb of LC, located at around the mid-span region, is responsible for bringing high concentration fluctuations from the surface to depths below. Thus, in this region the full-depth LC downwelling limb plays a more prominent role in distributing the scalar concentration than the downwelling and upwelling limbs of the small scale near-surface vortices and the impact of the latter on scalar transport is diminished.

Previously shown small-scale streamwise eddies consist of downwind elongated streaks of high speed and low-speed downwind velocity fluctuations when viewed on a horizontal plane (Fig. 6.6). These streaks have drawn a lot of attention since they are an important

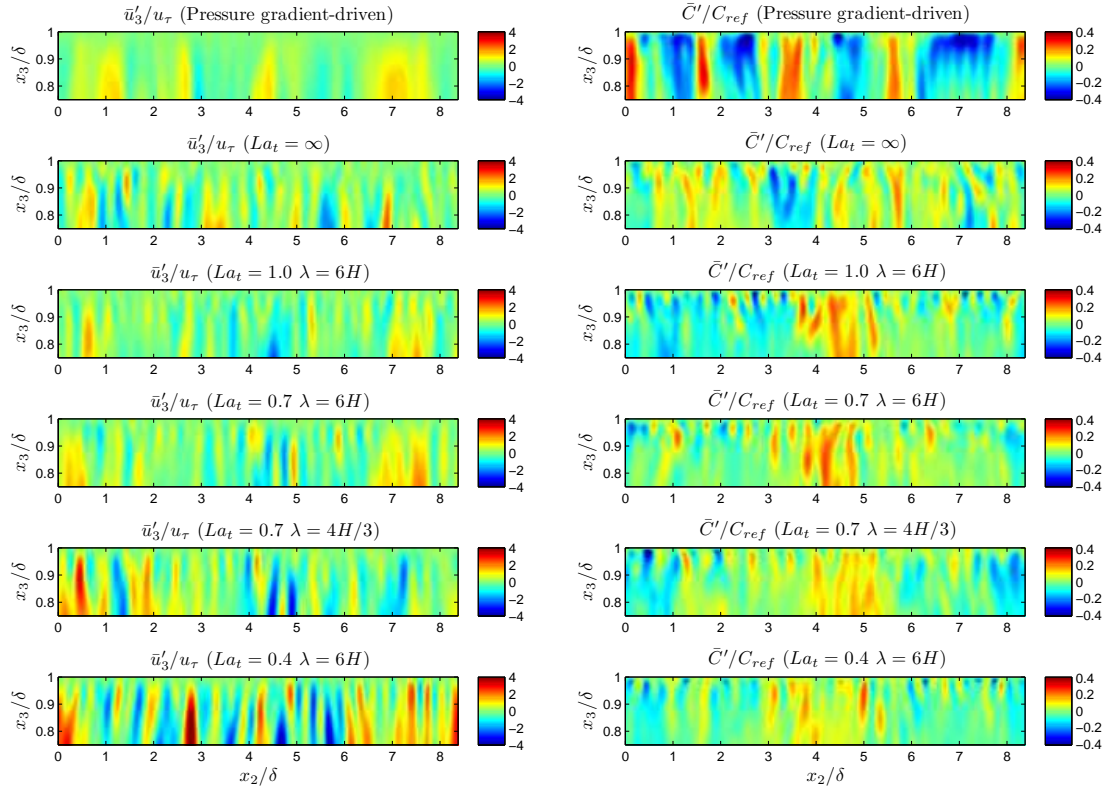


Figure 6.5: Instantaneous snapshots of vertical velocity fluctuations and scalar concentration fluctuations in the uppermost one-eighth portion of the water column at  $x_1 = L_1/2$  where  $L_1$  is the downwind length of the computational domain.

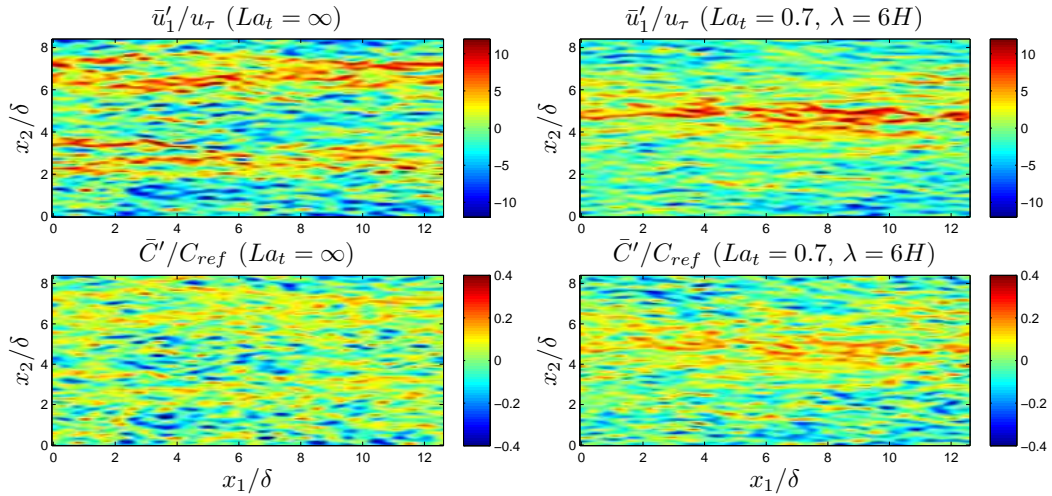


Figure 6.6: Instantaneous snapshots of downwind velocity fluctuations and scalar concentration fluctuations on a horizontal plane close to the surface within the buffer layer ( $x_3/\delta = 0.96$ ).

feature of surface and viscous sublayers (e.g. [32, 43, 46, 56, 79]). Notice that in Fig. 6.6, velocity streaks are correlated with streaks in concentration fluctuations. Similar structures and correlations in surface shear driven flow without wave effects are also described by Tsai et al. ([90–92]) and Calmet & Magnaudet [10]. Furthermore, the impact of the full-depth LC on the small-scale streaks can be seen in Fig. 6.6, as the positive streaks are generally concentrated towards the mid-span of the domain coinciding with the full-depth downwelling limb of LC. A similar impact of the Couette cells present in wind-driven flow without LC is also observed.

In order to better understand near surface scalar transport in wind driven flow without LC and in wind driven flow with LC away from the upwelling limb of LC, we start with the scalar transport equation which is also given in Eqn. 4.1:

$$\frac{\partial \bar{C}}{\partial t} + \frac{\partial (\bar{C} \bar{u}_j)}{\partial x_j} + \frac{1}{La_\tau^2} \phi_j^s \frac{\partial \bar{C}}{\partial x_j} = \frac{1}{Re Sc} \frac{\partial^2 \bar{C}}{\partial x_j^2} + \frac{\partial q_j}{\partial x_j} \quad (6.4)$$

Following Reynolds decomposition,  $\bar{u}_i = \langle \bar{u}_i \rangle + \bar{u}'_i$ , Eqn. 6.4 can be written as

$$\frac{\partial \langle \bar{C} \rangle}{\partial t} + \frac{\partial \langle \bar{C} \rangle \langle \bar{u}_j \rangle}{\partial x_j} + \frac{1}{La_\tau^2} \phi_j^s \frac{\partial \langle \bar{C} \rangle}{\partial x_j} = \frac{1}{Re Sc} \frac{\partial^2 \langle \bar{C} \rangle}{\partial x_j^2} + \frac{\partial \langle q_j \rangle}{\partial x_j} - \frac{\partial \langle \bar{u}'_j \bar{C}' \rangle}{\partial x_j} \quad (6.5)$$

where  $\langle \cdot \rangle$  denotes averaging in time and over the horizontal directions ( $x_1$  and  $x_2$ ). Since we are averaging in time, the first term  $\partial \langle \bar{C} \rangle / \partial t$  of LHS of the equation above becomes zero. Furthermore, in all our flows  $\langle \bar{u}_2 \rangle \approx 0$  and  $\langle \bar{u}_3 \rangle \approx 0$  since wind stress serves to drive mean flow in  $x_1$  only.

Also, we can re-write the second term on the LHS as



$$\frac{\partial \langle \bar{C} \rangle \langle \bar{u}_j \rangle}{\partial x_j} = \langle \bar{u}_1 \rangle \frac{\partial \langle \bar{C} \rangle}{\partial x_1} + \langle \bar{u}_2 \rangle \frac{\partial \langle \bar{C} \rangle}{\partial x_2} + \langle \bar{u}_3 \rangle \frac{\partial \langle \bar{C} \rangle}{\partial x_3} = 0 \quad (6.6)$$

Since we are averaging in time and over the horizontal directions ( $x_1$  and  $x_2$ ), derivatives of mean concentration  $\langle \bar{C} \rangle$  with respect to  $x_1$  and  $x_2$  become zero.

As a result, Eqn. 6.4 becomes

$$0 = \underbrace{-\frac{1}{La_t^2} \phi_j^s \frac{d\langle \bar{C} \rangle}{dx_j}}_L + \underbrace{\frac{1}{Re Sc} \frac{d^2 \langle \bar{C} \rangle}{dx_j^2}}_D + \underbrace{\frac{d\langle q_j \rangle}{dx_j}}_S \underbrace{-\langle \bar{u}'_1 \frac{d\bar{C}}{dx_1} \rangle}_{T_1} \underbrace{-\langle \bar{u}'_2 \frac{d\bar{C}}{dx_2} \rangle}_{T_2} \underbrace{-\langle \bar{u}'_3 \frac{d\bar{C}}{dx_3} \rangle}_{T_3} \quad (6.7)$$

where  $L$  is Langmuir forcing,  $D$  is molecular diffusion,  $S$  is the subgrid-scale flux and  $T_1$ ,  $T_2$ ,  $T_3$  are transports in downwind, crosswind and vertical directions, respectively.

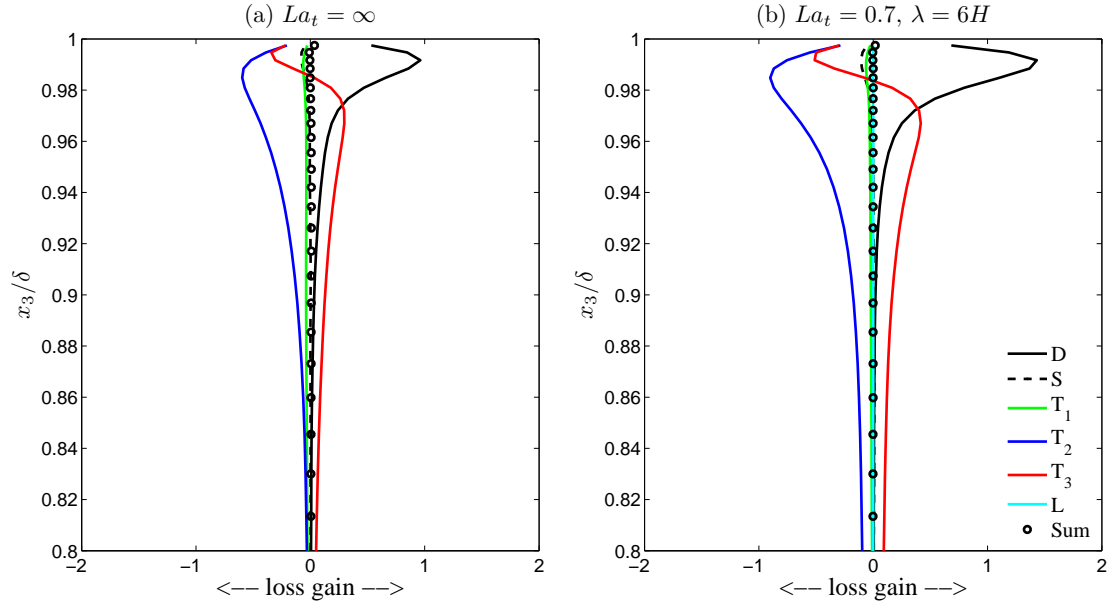


Figure 6.7: Near surface budgets of Reynolds averaged scalar transport equation in (a) wind driven flow without LC and (b) in wind driven flow with LC (with  $La_t = 0.7$ )

Using the space and time-dependent numerical solutions of the LES equations in Section 4.1.2 each of the terms in Eqn. 6.7 were computed and plotted in Fig. 6.7 for wind



takes high concentration fluid from the surface to depths below the surface. Conversely, on the left side of the eddy, we see an upward motion that takes low concentration fluid from below up to the surface. This results in a surface positive crosswind gradient of  $\bar{C}'$ . This near-surface crosswind gradient of concentration fluctuations and the predominantly positive crosswind velocity fluctuations ( $\bar{u}'_2$ ) associated with the top of the eddy result in a near-surface region of instantaneous negative crosswind transport,  $-\bar{u}'_2 \partial \bar{C}' / \partial x_2$  (See Fig. 6.8(b)).

The result of Fig. 6.8(b) indicates that near-surface small eddies play an important role in determining crosswind transport. However, this previous result is based on instantaneous fields. To establish a coherency between streamwise near-surface small eddies and crosswind transport, we performed conditional averaging over  $x_1$  and time, similar to the conditional averaging performed by Debusschere and Rutland [16] in the near-wall region of a turbulent Couette flow.

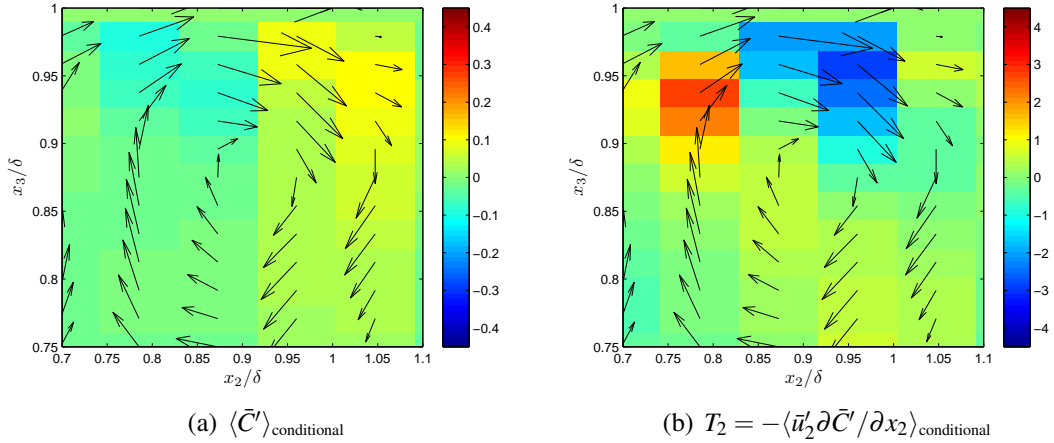


Figure 6.9: Conditionally averaged velocity fluctuation vectors superimposed with color contour of (a) conditionally averaged concentration fluctuation  $\langle \bar{C}' \rangle_{\text{conditional}}$  and (b) conditionally averaged crosswind transport,  $T_2$ , in wind-driven flow without LC.

Averaging was performed only over  $x_2 - x_3$  ( $x_1$ ) planes that have  $-\bar{u}'_2 \partial \bar{C}' / \partial x_2 \geq -\langle \bar{u}'_2 \partial \bar{C}' / \partial x_2 \rangle$  and that have crosswind velocity fluctuations greater than zero ( $\bar{u}'_2 > 0$ ) at the point  $x_2/\delta = 0.92$  and  $x_3/\delta = 0.98$  (following the instantaneous results of Figs. 6.8(a) and 6.8(b)). Note that  $x_2/\delta = 0.92$  corresponds to the  $x_2$  location of the instantaneous eddy in Figures 6.8(a) and 6.8(b)), and  $x_3/\delta = 0.98$  corresponds to the near surface depth at which  $T_2 = -\langle \bar{u}'_2 \partial \bar{C}' / \partial x_2 \rangle$  reaches a maximum (See Fig. 6.7).

Figures 6.9(a) and 6.9(b) show results of the previously described conditional average. The averaging demonstrates that events such as the one depicted in Figures 6.8(a) and 6.8(b)) in terms of instantaneous fields are indeed common. Thus, small streamwise eddies are strongly correlated with concentration fluctuation  $\bar{C}'$  and crosswind transport near the surface in wind-driven flow without LC. In wind driven flows with LC such events are also common in near surface regions away from the upwelling limb of the large scale LC. In these flows, in near-surface regions occupied by the upwelling limb of full-depth LC, the latter dominates vertical transport, thereby diminishing the impact of the near surface small scale eddies, as described earlier.

## 6.3 Mean Scalar Concentration and Transfer Velocity

### 6.3.1 Bulk concentration

As will be discussed in greater detail, transfer velocity  $K$  depends on the scalar concentration in the bulk region of the flow,  $C_{\text{bulk}}$ . Thus it is important to try to define the bulk region.

The bulk region is the part of the water column not strongly affected by surface effects nor bottom effects. The near-surface turbulent structure differs greatly between the different flows studied here, especially between the pressure-gradient driven flow, the wind-driven flow without LC and any of the wind-driven flows with LC. In the case of flow with LC, the surface affects the entire water column as the Langmuir cells are generated precisely at the surface. Overall, given the vast differences in the turbulent mixing between all the flows studied, there is no single, well-defined way of obtaining the shallowest depth of the bulk region ("the depth of the bulk region") across all simulations. The simplest way to set this depth is to let it be equal to the shallowest depth where the vertical gradient of mean concentration or mean downwind velocity becomes zero. This works well for the flows with LC. For each of the following LC cases ( $La_t = 0.7$ ,  $\lambda = 6H$ ), ( $La_t = 1.0$ ,  $\lambda = 6H$ ) and ( $La_t = 0.4$ ,  $\lambda = 6H$ ) the vertical gradients of mean velocity and mean concentration become zero at slightly different depths. Because of the strong homogenizing action of the LC, for each case, the concentrations at those depths (i.e. the value of  $C_{\text{bulk}}$ ) differ by  $\sim 1\%$  from one another. For these cases the depth of the bulk region is taken as given through the vertical gradient of mean concentration. For the LC case ( $La_t = 1.0$ ,  $\lambda = 4H/3$ ) the vertical gradient of mean concentration never becomes zero, thus the vertical gradient of mean velocity is used to determine the depth of the bulk region. For the pressure gradient-driven flow, vertical gradients of mean concentration and vertical gradient of mean velocity never become zero. For this case, we follow Calmet and Magnaudet (2003) [11] and take the depth of the bulk region to be the near-surface depth at which the root mean square of crosswind and vertical fluctuations deviate from each other. Note that in Fig. 6.10, crosswind (blue) and vertical (red) rms start to deviate from each other at

$x_3/\delta \sim 0.6$  denoting the depth of the bulk region and thus the depth where  $C_{\text{bulk}}$  is obtained. Finally, for the wind-driven flow without LC, vertical gradients of mean concentration and vertical gradient of mean velocity never become zero. Furthermore, the approach used for pressure gradient-driven flow is not applicable. Thus, we let the depth of the bulk region be the depth where the vertical gradients of root mean square of vertical and crosswind velocity fluctuations become zero which corresponds to the middle of the water column.

As described above, across simulations we have had to use a different measure for determining the depth of the bulk region and subsequently  $C_{\text{bulk}}$ . In order to avoid the uncertainty of locating the bulk region, we have alternatively taken  $C_{\text{bulk}}$  as the mean concentration at the middle of the water column for all cases. This approach is similar to Dong et al. (2003) [22] who in their simulations of turbulent channel flow (i.e. flow between parallel plates (walls)) took  $\Delta C$  in the equation for  $K$  as the difference between mean concentration at the top and bottom walls (normally  $\Delta C$  is the difference between concentration at the surface and in the bulk region). Thus, for each flow except for the wind-driven flow without LC, we have two values of  $C_{\text{bulk}}$  and thus two values of  $K$ . These are listed in the Tables 6.1 and 6.2 further below. The values of  $C_{\text{bulk}}$  reported in Table 6.2 correspond to mean concentration at the middle of the water column and the values of  $C_{\text{bulk}}$  given in Table 6.1 correspond to mean concentration at different locations of the depth of the bulk region depending on the definitions described above.

From Tables 6.1 and 6.2, one can see that estimates of  $K$  vary by only a few percent based on the two different methods of estimating  $C_{\text{bulk}}$  described previously. That means that, even though the way we choose  $C_{\text{bulk}}$  is not well defined, the final result (i.e. the estimated value of  $K$ ) is not strongly influenced by how we choose  $C_{\text{bulk}}$ .

Table 6.1: Comparison of  $K_{LES}$ ,  $C_{\text{bulk}}$ ,  $\Delta C$  and vertical gradient of concentration at the surface for all flows;  $C_{\text{bulk}}$  is the mean concentration at the shallowest depth of the bulk region based on the definitions described earlier.

Case	$K_{LES}/u_\tau$	$\frac{C_{\text{bulk}}}{C_{\text{ref}}}$	$\frac{\Delta C}{C_{\text{ref}}}$	$\frac{\delta}{C_{\text{ref}}} \left( \frac{d\langle C \rangle}{dx_3} \right)_{x_3=\delta}$
Pressure gradient-driven	0.055	0.577	0.423	9.203
$La_t = \infty$	0.066	0.571	0.429	11.224
$La_t = 1.0, \lambda = 6H$	0.078	0.600	0.400	12.282
$La_t = 0.7, \lambda = 6H$	0.096	0.650	0.350	13.219
$La_t = 0.7, \lambda = 4H/3$	0.123	0.722	0.298	14.101
$La_t = 0.4, \lambda = 6H$	0.141	0.720	0.280	16.556

Table 6.2: Comparison of  $K_{LES}$ ,  $C_{\text{bulk}}$ ,  $\Delta C$  and vertical gradient of concentration at the surface for all flows;  $C_{\text{bulk}}$  is the mean concentration at the middle of the water column.

Case	$K_{LES}/u_\tau$	$\frac{C_{\text{bulk}}}{C_{\text{ref}}}$	$\frac{\Delta C}{C_{\text{ref}}}$	$\frac{\delta}{C_{\text{ref}}} \left( \frac{d\langle C \rangle}{dx_3} \right)_{x_3=\delta}$
Pressure gradient-driven	0.049	0.524	0.476	9.203
$La_t = \infty$	0.066	0.571	0.429	11.224
$La_t = 1.0, \lambda = 6H$	0.081	0.614	0.386	12.282
$La_t = 0.7, \lambda = 6H$	0.097	0.654	0.346	13.219
$La_t = 0.7, \lambda = 4H/3$	0.120	0.703	0.297	14.101
$La_t = 0.4, \lambda = 6H$	0.137	0.711	0.289	16.556

Increased large-scale homogenization induced by strengthening LC gives rise to a thinner molecular boundary layer at the surface. This serves to increase the diffusive scalar flux (transfer rate) at the surface, the latter proportional to the vertical gradient of mean concentration at the surface (listed in Tables 6.1 and 6.2). A greater transfer rate of the scalar across the surface into the water column leads to an increase in mean scalar concentration in the bulk flow region. This increase in bulk mean concentration is reflected by a decrease in  $\Delta C$ , defined as the difference between mean concentration at the surface and mean concentration in the bulk flow,  $C_{\text{bulk}}$ . Values of  $\Delta C$  for the different flows are listed in Tables 6.1 and 6.2. Note that this previous trend in  $\Delta C$  is independent of the method in calculating  $C_{\text{bulk}}$  described earlier.

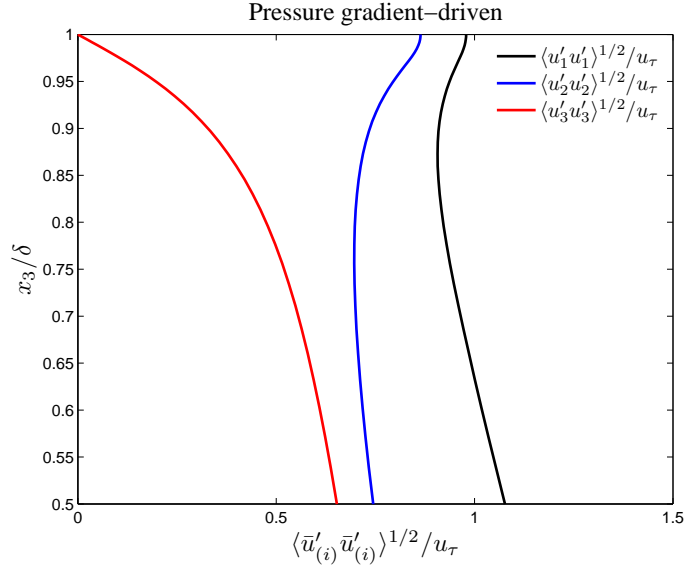


Figure 6.10: Components of root mean square of velocity in pressure gradient-driven flow.

As observed earlier, in the case of a decreasing surface wave wavelength,  $\lambda$  with fixed  $La_t$ , LC becomes weaker. However, in this case the increasing near-surface Stokes drift velocity shear leads to higher small scale turbulence (in terms of the vertical velocity fluctuations) (see Fig. 6.3b). This gives rise to increased levels of vertical mixing near the surface, resulting in an increase in vertical gradient of the mean concentration (listed in Tables 6.1 and 6.2) and thus greater diffusion in that region. This then serves to increase the diffusive scalar transfer across the surface leading to an increase in scalar concentration in the bulk flow region, similar to the case with decreasing  $La_t$  previously described. This increase in bulk mean concentration is reflected by a decrease in  $\Delta C$ , also listed in Tables 6.1 and 6.2.

Consider the flows with LC with  $(La_t = 0.7, \lambda = 4H/3)$  and  $(La_t = 0.7, \lambda = 6H)$ . Recall that in the latter case the full-depth LC is stronger, however, the near-surface intensity of vertical velocity fluctuations is weaker. As can be seen from Tables 6.1 and 6.2, despite



the weaker LC, the near-surface vertical turbulence intensity in the  $\lambda = 4H/3$  case is able to produce a sharper vertical gradient of mean scalar concentration at the surface and thus greater molecular diffusion at the surface than in the  $\lambda = 6H$  case. Thus, the bulk mean concentration is greater in the  $\lambda = 4H/3$  flow than in the  $\lambda = 6H$  flow. However, note that the stronger LC in the  $\lambda = 6H$  case is able to generate greater mixing throughout the entire water column than the LC in the  $\lambda = 4H/3$  case leading to a more uniform mean scalar concentration profile, as seen in Fig. 6.11.

Transfer velocity  $K$  (a measure of mass transfer efficiency at the surface) is defined proportional to the vertical gradient of mean concentration evaluated at the surface and is expressed as

$$K = \frac{D}{\Delta C} \left( \frac{d\langle \bar{C} \rangle}{dx_3} \right)_{x_3=\delta} \quad (6.8)$$

where  $D$  is the molecular diffusivity [10]. Values of  $K$  non-dimensionalized by wind stress friction velocity  $u_\tau$  are listed in Tables 6.1 and 6.2. This quantity is often referred to as the Stanton number ( $St$ ) and is related to the Sherwood number ( $Sc$ ) popular within the chemical engineering community as  $Sh = St Re Sc$ . In general, transfer velocity or  $St$  increases under decreasing  $La_t$  and fixed  $\lambda$ . Transfer velocity also increases under decreasing  $\lambda$  and fixed  $La_t$ . These trends are consistent with the trends observed in  $\Delta C$  and  $d\langle \bar{C} \rangle/dx_3$  at the surface, as described earlier.

According to the LES results (as can be seen from Tables 6.1 and 6.2), transfer velocity is approximately 46% higher in wind driven flow with LC (with  $La_t = 0.7$  and  $\lambda = 6H$ ) than in wind driven flow without LC. When Reynolds number dependence of the results is examined, it is seen that increase in transfer velocity is about 68% for a lower Reynolds

number ( $Re_\tau = 180$ ). Thus, increase in transfer velocity under the action of LC should occur at higher Reynolds numbers as well. Further information on Reynolds number dependence can be found in Appendix G. We have also analyzed Schmidt number dependence which is given in more detail in Appendix F. According to the theoretical law showing the relationship between transfer velocity and Schmidt number, transfer velocity is given as  $K \approx Sc^{-0.5}$ . We found that this classical law still holds in the presence of LC.

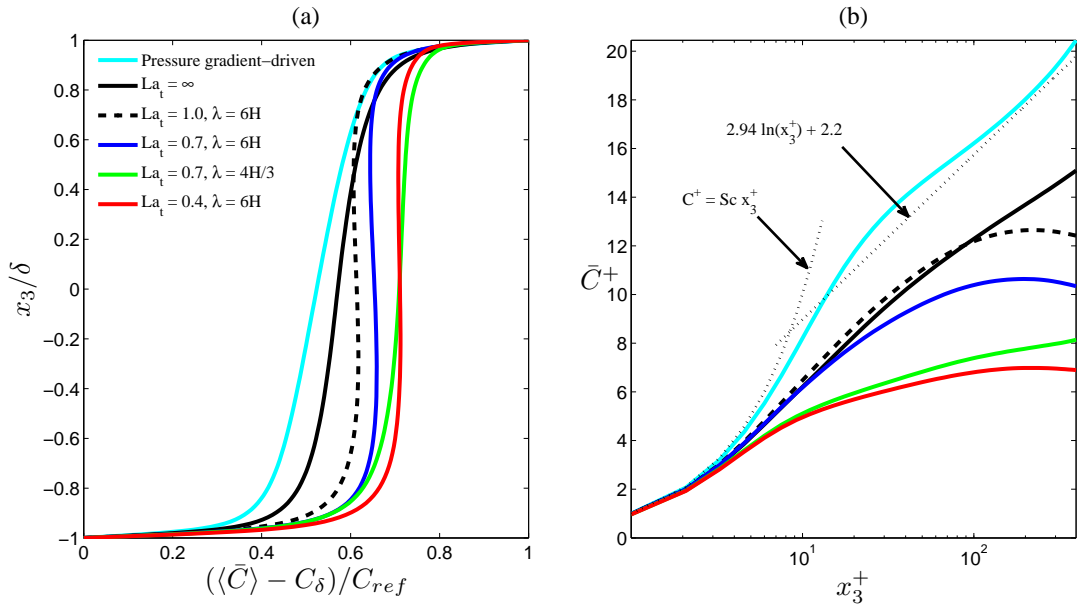


Figure 6.11: Mean concentration (a) and mean concentration deficit in the upper half of the water column (b) in flows with and without LC.

Fig. 6.11b plots mean concentration versus  $x_3^+$  which measures distance to the surface in plus units. Here, the superscript '+' denotes normalization by the friction concentration  $c_* = (D/u^*)(\partial \langle \bar{C} \rangle / \partial x_3)_{x_3 = -\delta}$ , thus  $C^+$  is defined as:

$$C^+ = \frac{C_\delta - \langle \bar{C} \rangle}{c_*} \quad (6.9)$$

In pressure gradient-driven flow and wind driven flow without LC, the profiles of  $C^+$  satisfy the law of the wall with  $C^+ = Sc x_3^+$  and  $C^+ = (1/\kappa) \ln x_3^+ + B$ . The presence of LC leads to a deviation from the classical log-law near-surface concentration behavior exhibited by pressure gradient-driven flow and wind stress-driven flow without LC. The increase in bulk scalar concentration due to a decreasing  $La_t$  or a decreasing  $\lambda$  leads to large deviations from the classical log-layer and diffusive sublayer profiles. Flows with  $La_t = 0.4$ ,  $\lambda = 6H$  and  $La_t = 0.4$ ,  $\lambda = 6H$  yield the most deviation.

## 6.4 Chapter Summary

Large-eddy simulation (LES) of shallow water Langmuir turbulence has been conducted in order to understand transport at the surface and throughout the entire water column.

The large scales of the Langmuir turbulence are characterized by full-depth Langmuir circulation (LC), consisting of downwind-elongated full-depth vortices. The strength of LC (determined through the magnitude of downwind-averaged crosswind and vertical velocity fluctuations) was seen inversely proportional to the turbulent Langmuir number ( $La_t$ ). This parameter is representative of wind forcing relative to wave forcing. Thus, an increase in wave forcing leads to smaller  $La_t$ , greater Craik-Leibovich vortex forcing throughout the entire water column and stronger LC. The strength of LC was also seen proportional to the wavelength of surface waves ( $\lambda$ ) generating LC. Waves of shorter wavelength generate weaker LC.

Two key mechanisms were identified controlling near-surface scalar transport and thus the transfer rate of the scalar from the surface into the interior of the water column in the presence of Langmuir turbulence. The first mechanism is provided by the large-scale full-depth LC turbulent structure. Given the Dirichlet boundary conditions imposed on the scalar concentration with concentration greater at the surface than at the bottom, the surface (i.e. the air-water interface) acts as a source and the bottom wall acts as a sink for the scalar. Furthermore, given these boundary conditions, the downwelling limb of LC takes high concentration fluctuations from the surface to the bottom and the upwelling limb takes low concentration fluctuations from the bottom to the surface. As a result, LC is seen to increase resolved vertical turbulent scalar flux within the bulk region of the flow. Additional impact of LC is seen through its mixing of the scalar throughout the entire water column. The enhanced mixing provided by LC (relative to a similar wind-driven flow, but without LC, i.e. without the C-L vortex force) leads to a thinning of the mean scalar concentration surface boundary layer, and thus an increase in vertical gradient of the mean concentration in that region. In turn, this gives rise to increased molecular diffusion at the surface and thus a greater scalar transfer rate from the surface into the water column.

The second key mechanism controlling scalar transport and its transfer at the surface in the presence of Langmuir turbulence is provided directly by the Stokes drift velocity. A decrease in surface wave wavelength ( $\lambda$ ) leads to greater Stokes drift velocity shear near the surface, which was seen to increase the root mean square of vertical velocity fluctuations (i.e. vertical turbulent kinetic energy) despite a weakening of the full-depth LC. Note that shorter waves induce smaller values of the Stokes drift velocity and the Craik-Leibovich vortex force throughout the entire water column, hence leading to a weaker LC. However,

the increased small scale vertical turbulent activity near the surface induced by the Stokes drift velocity shear of shorter waves leads to enhanced near-surface mixing, sharper vertical gradient of mean scalar concentration, greater molecular diffusion and greater transfer rate of the scalar into the water column. Increased vertical turbulence intensity near the surface associated with Stokes drift velocity shear also leads to greater resolved vertical turbulent scalar within the bulk region of the flow.

## Chapter 7:

### Mass Transfer Through Air-Water Interfaces

#### 7.1 Surface Renewal Theory

As noted in the introduction, scientists are interested in making estimates of mass flux of sparingly soluble gases across the air-sea interface. Of interest is CO<sub>2</sub> since oceans uptake 30-40% portion of human-made CO<sub>2</sub>. Mass flux can be obtained as

$$F = K\Delta C \quad (7.1)$$

where  $K$  is the transfer velocity as described earlier and  $\Delta C$  is the difference in concentration in the aqueous phase across the diffusion sub-layer. Surface renewal theory is one of the widely accepted theories used to obtain parameterizations of  $K$ . This theory suggests that mass transfer rate can be determined from a relation between the molecular diffusivity and the *surface renewal rate*. *Surface renewal rate* comes from the concept that turbulent eddies bring up fresh fluid packages from below intermittently as described earlier in Chapter 3. According to surface renewal theory transfer velocity can be obtained as

$$K = (D/\tau_r)^{1/2} \quad (7.2)$$

Several parameterizations are derived based on surface renewal theory where each parameterization has its own definition of renewal time scale,  $\tau_r$ . One of the objectives of the current work is to test these different parameterizations evaluated through large eddy simulation (LES) results previously presented.

Following Eqn. 7.1, transfer velocity is expressed as

$$K = \frac{F}{\Delta C} \quad (7.3)$$

As discussed earlier in Section 1, in our LES we can directly compute the flux  $F$  following Fick's law:

$$F = D \left( \frac{d\langle \bar{C} \rangle}{dx_3} \right)_{x_3=\delta} \quad (7.4)$$

where  $D$  is the diffusivity of the scalar and  $(d\langle \bar{C} \rangle/dx_3)_{x_3=\delta}$  is the gradient of the mean concentration in the vertical direction evaluated at the surface. Inserting Eqn. 7.4 into Eqn. 7.3 leads to

$$K = \frac{D}{\Delta C} \frac{d\langle \bar{C} \rangle}{dx_3} \Big|_{x_3=\delta} \quad (7.5)$$

from which we are able to compute  $K$  directly in our LES.

In the following sections, we describe four different models (parameterizations) that are based on the surface renewal theory: (i) Stokes drift shear model (ii) large eddy model; (iii) small eddy model; (iv) surface divergence model. We compare  $K$  obtained from these parameterizations to  $K$  computed directly in LES via Eqn. 7.5.

Note that  $K$  values predicted in LES and used for analysis in this chapter have been computed using the value of  $C_{\text{bulk}}$  corresponding to the mean concentration at the middle

of the water column. Alternative ways for obtaining  $C_{\text{bulk}}$  were described in the previous chapter. Also note that we are interested in testing how well the models can capture the trend in  $K$  with variations in wind and wave forcing parameters  $La_t$  and  $\lambda$ . A measure of this is obtained by determining the slope of the best-fit line through the points mapping  $K$  predicted by LES versus  $K$  predicted by one of the models.

### 7.1.1 Stokes Drift Shear Model

In Chapters 5 and 6, we have seen that shorter wavelength results in greater Stokes drift velocity shear and causes a disruption in both mean velocity and scalar concentration profiles. For example, this disruption is more notable in flow with LC with  $La_t = 0.7$  and  $\lambda = 4H/3$  than in the flow with LC with  $La_t = 0.7$  and  $\lambda = 6H$  due to the higher near surface Stokes drift velocity shear in the former. Thus, we propose to set the surface renewal time scale as inversely proportional to the Stokes drift shear at the surface

$$\tau_r \propto \left( \frac{\partial U_s}{\partial x_3} \right)_{x_3=\delta}^{-1} \quad (7.6)$$

where  $U_s$  is the Stokes drift velocity. Inserting Eqn. 7.6 into Eqn. 7.2 gives

$$K \propto \left( D \frac{\partial U_s}{\partial x_3} \right)^2 \quad (7.7)$$

Fig. 7.1 exhibits vertical gradient of dimensionless Stokes drift velocity for different flow with LC. Notice that the case with smallest  $\lambda$  yields higher Stokes drift shear at the surface.



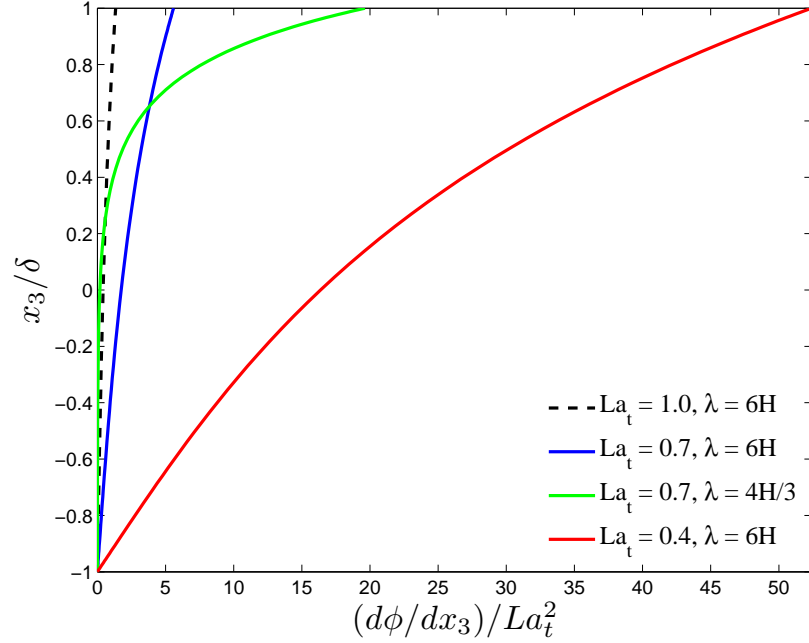


Figure 7.1: Comparison of dimensionless vertical gradient of dimensionless Stokes drift velocity shear for different flows with LC.

Fig. 7.2 shows a comparison of transfer velocity results obtained with the Stokes drift shear model with transfer velocity evaluated directly in the LES. This model predicts the increasing trend in transfer velocity as  $La_t$  decreases and also when  $\lambda$  decreases. Stokes drift shear model prediction gets better with smaller  $La_t$  (i.e. more coherent LC). However, for bigger  $La_t$  like 1.0, the model prediction is not as accurate. This is expected because with increasing  $La_t$  as C-L vortex forcing and thus Langmuir turbulence becomes less prominent in determining near surface dynamics.

### 7.1.2 Large Eddy Model

Gulliver and Halverson [31] conducted laboratory flume experiments on mass transfer. Their results were in a flume which generates large-scale streamwise vortices extending from the top of the water column to the bottom. Note that these streamwise vortices are not

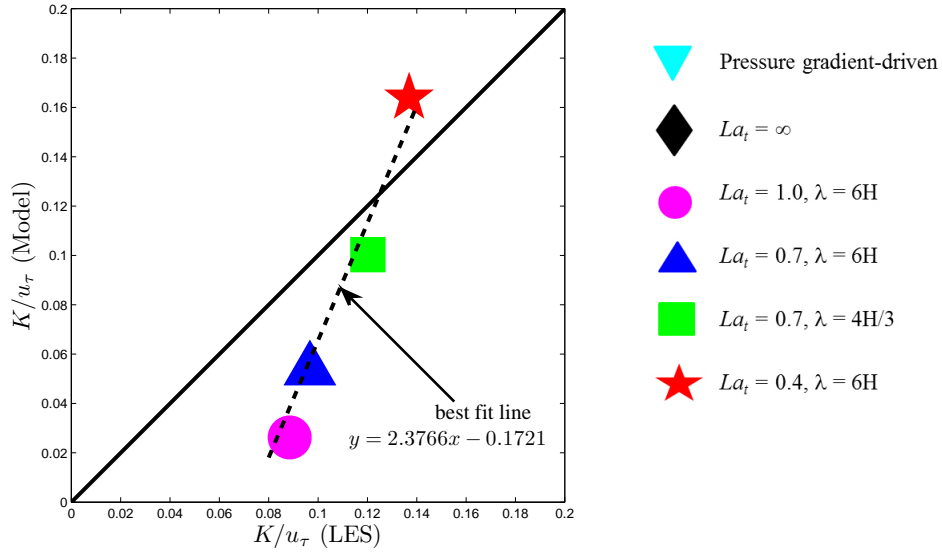


Figure 7.2: Comparison of transfer velocity evaluated through Stokes drift shear model based on surface renewal theory with LES results.

LC. From these experiments they concluded that the surface renewal is governed by these large scale structures and proposed

$$\tau_r = \frac{1}{(k_f w_s / h) F_r} \quad (7.8)$$

where  $w_s$  is the maximum vertical velocity associated with large scale eddies,  $h$  is the depth of the water column,  $k_f$  is a constant showing that average renewal is a fraction of that caused by  $w_s$ , and  $F_r$  is a portion of an eddy consisting of an upwelling. Inspired by Gulliver and Halverson's [31] work, we define a surface renewal time scale,  $\tau_r$ , that is based on the large scale eddies as follows

$$\tau_r \propto \frac{1}{[\langle \bar{u}'_3 \rangle_{t,x_1}^{max} / h] F_r} \quad (7.9)$$

Inserting Eqn. 7.9 into Eqn. 7.2 gives

$$K \propto \left( \frac{D}{[\langle \bar{u}'_3 \rangle_{t,x_1}^{max} / H] F_r} \right)^{1/2} \quad (7.10)$$

In our implementation,  $\langle \bar{u}'_3 \rangle_{t,x_1}^{max}$  is the maximum of the partially averaged vertical velocity fluctuations shown in Fig. 7.3. Averaging here is performed over time ( $t$ ) and over the downwind direction ( $x_1$ ). Values of  $\langle \bar{u}'_3 \rangle_{t,x_1}^{max}$  for all flows are given in Table 7.1. One can see that wind driven flows with LC have much greater values of  $\langle \bar{u}'_3 \rangle_{t,x_1}^{max}$  compared to wind driven flow without LC and pressure gradient-driven flow. Also, among the wind driven flows with LC,  $La_t = 0.4$  has the greatest  $\langle \bar{u}'_3 \rangle_{t,x_1}^{max}$  value as Langmuir cells are strongest in this case.

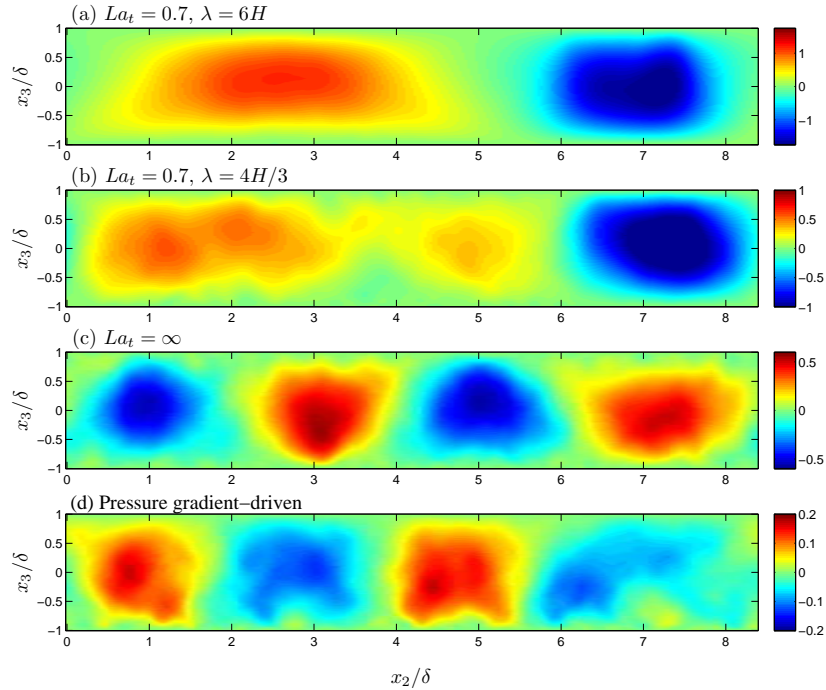


Figure 7.3: Time/downwind averaged vertical velocity fluctuations,  $\langle \bar{u}'_3 \rangle_{t,x_1} / u_\tau$ .

Table 7.1: Comparison of values of maximum dimensionless partially averaged vertical velocity fluctuations and  $F_r$  for different flows.

Case	$K_{LES}/u_\tau$	$\left(\frac{\langle \bar{u}'_3 \rangle_{t,x_1}^{max}}{u_\tau}\right)^{1/2}$	$(F_r)^{1/2}$
Pressure gradient-driven	0.049	0.412	0.650
$La_t = \infty$	0.066	0.751	0.707
$La_t = 1.0, \lambda = 6H$	0.081	1.181	0.682
$La_t = 0.7, \lambda = 6H$	0.097	1.367	0.773
$La_t = 0.7, \lambda = 4H/3$	0.120	1.121	0.843
$La_t = 0.4, \lambda = 6H$	0.137	1.530	0.791

After  $\langle \bar{u}'_3 \rangle_{t,x_1}^{max}$  is evaluated, we also need to find the value of  $F_r$  (i.e. the portion of a large-scale eddy consisting of an upwelling). Gulliver and Halverson [31] reported that  $F_r$  is a function of Reynolds number in the case of the streamwise vortices in their flume experiments. Later in this dissertation results will be shown from LES of wind driven flow with LC at different Reynolds number (Re) for which we have found that the value of  $F_r$  for LC is independent of Re. Furthermore, we note that even though Re is much smaller in our LES than in field observations of LC, our value of  $F_r$  is in agreement with those measured during the field observations. Interested reader is directed to [27, 86] for more information on comparison of the simulations with field measurements.

In the upper two panels of Fig. 7.3, partially averaged vertical velocity fluctuations are shown for wind driven flows with LC. From these panels we can see that in the wind driven flows with LC, the upwelling and downwelling limbs of full-depth LC are strongly coherent in the downwind direction as described in Chapters 5 and 6. Furthermore, although wind driven flow without LC and pressure gradient driven flow also have coherent large scale structures, they are not as coherent as full-depth LC as can be seen by comparing Figs. 7.3a,b,c,d.

LC consists of an upwelling (positive regions in Fig. 7.3a,b) and a downwelling limbs (negative regions in Fig. 7.3a,b). We can determine  $F_r$  as the ratio between the size of the upwelling limb to the size of the LC using partially averaged vertical velocity fluctuations shown Figs. 7.3a,b. In brief, the  $F_r$  value is calculated by taking the depth-average of partially averaged vertical velocity fluctuations and then finding the ratio of the depth-averaged upwelling region to the size of the domain in the  $x_2$  (crosswind) direction. Values of  $F_r$  for different flows are given in Table 7.1.

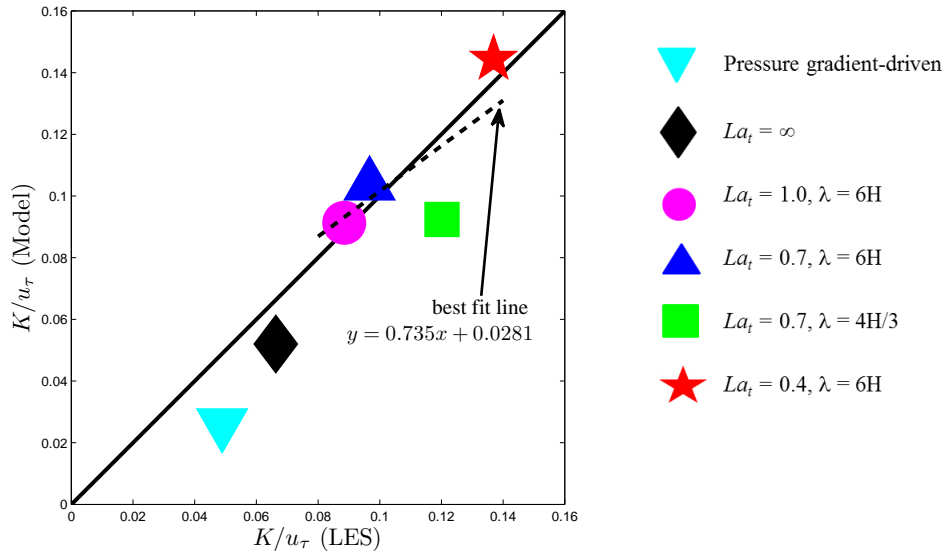


Figure 7.4: Comparison of transfer velocity evaluated through large eddy model based on surface renewal theory with LES results.

Fig. 7.4 shows comparison of transfer velocity evaluated through large eddy model with LES results. Note that a constant proportionality of 2.75 is used when evaluating the modeled transfer velocity in Eqn. 7.10. Transfer velocity values are in good agreement with transfer velocity of the LES. Moreover, the LES predicts an increase in transfer velocity with decreasing  $La_t$  (i.e. with increasing strength of large scale structures). For instance, in wind driven flow with LC (with  $La_t = 0.7$ ) transfer velocity is 60 % higher than the wind

driven flow without LC. Recall that, in wind driven flows with LC, large scale structures become more coherent with decreasing turbulent Langmuir number,  $La_t$ . The stronger coherency of large scale structures leads to higher transfer velocity. The large eddy model is able to capture this effect because it is explicitly given in terms of a vertical velocity scale associated with the large scale structures. Also, as the strength of the large scale structure increases (i.e. as  $La_t$  decreases), the large eddy model transfer velocity prediction gets better.

On the other hand, when the model is tested for a different  $\lambda$ , it is seen that the model prediction is not able to capture the increasing trend in transfer velocity with decreasing  $\lambda$ . This is to be expected since large eddy model depends on the downwind averaged vertical velocity fluctuations which are weaker in wind driven flow with  $La_t = 0.7$  and  $\lambda = 4H/3$  compared to wind driven flow with  $La_t = 0.7$  and  $\lambda = 6H$  as explained in detail in Chapter 5.

### 7.1.3 Small Eddy Model

Turbulent flow consists of wide range of scales, from small ones to large ones. Small eddies (scales) are dissipated by viscosity  $\nu$ . Thus, if we assume that small scales dominate the mass transfer at the surface ([5, 48, 100]), then

$$\tau_r \propto (\nu/\varepsilon)^{1/2} \quad (7.11)$$

where  $\varepsilon$  is the turbulent kinetic energy (TKE) dissipation rate evaluated at the surface. This model has been shown to yield good results for flows without LC with wave-breaking based

on the field measurements of Zappa et al. [100]. TKE dissipation rate appears in the TKE budgets given in Appendix C and is given as:

$$\varepsilon = \nu \left\langle \frac{\partial u'_i}{\partial x_j} \frac{\partial u'_i}{\partial x_j} \right\rangle \quad (7.12)$$

Inserting Eqn. 7.11 into Eqn. 7.2 gives

$$K \propto \left( \frac{D\varepsilon}{\nu} \right)^{1/2} \quad (7.13)$$

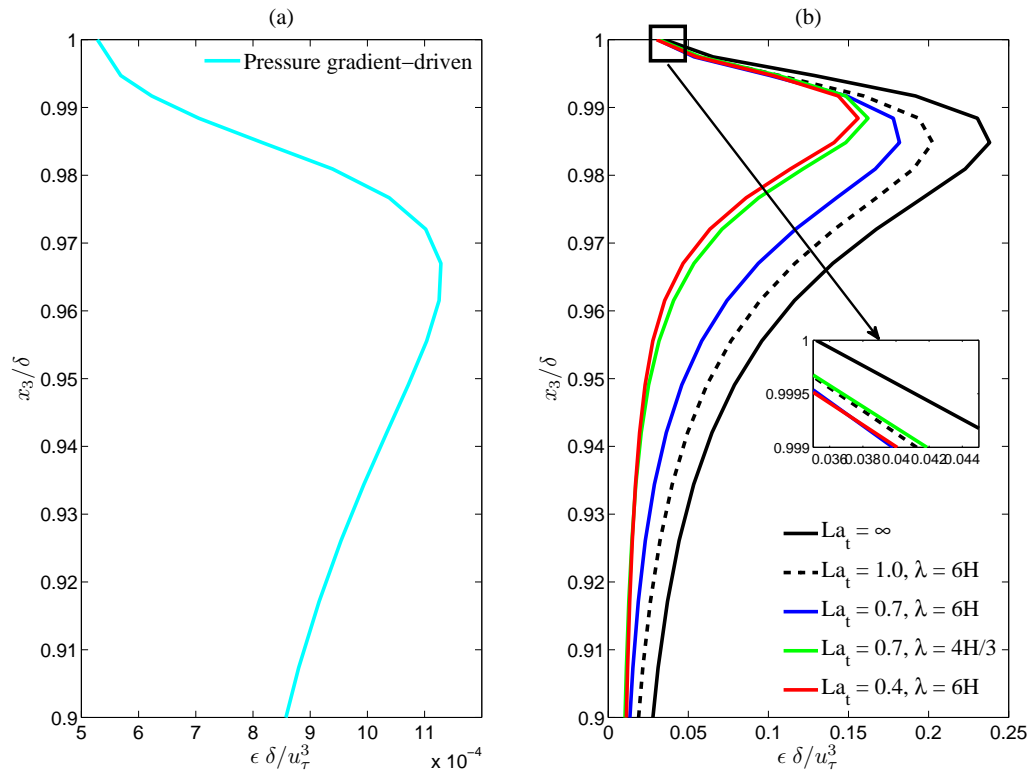


Figure 7.5: TKE dissipation (a) for pressure gradient-driven flow, (b) for wind driven flows with and without LC

As discussed in Chapter 6, the effect of small eddies on near surface transport is diminished in presence of large scale upwelling limbs of LC. Thus, one would expect that the

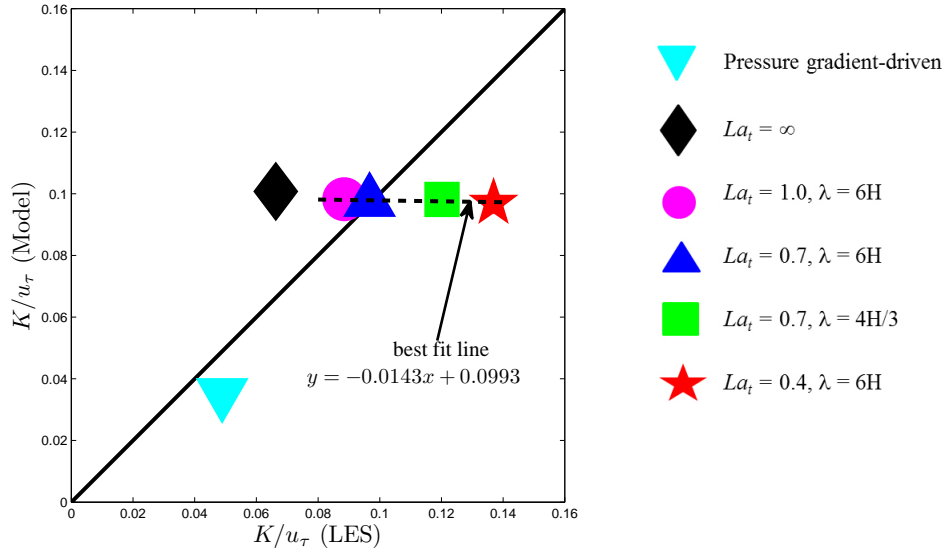


Figure 7.6: Comparison of transfer velocity evaluated through small eddy model based on surface renewal theory with LES results.

small eddy model would not be able to capture the effect of LC as it is based on the small eddies. This is verified by the poor values of transfer velocity predicted by the small eddy model as shown in Fig. 7.6.

Table 7.2: Comparison of values of dimensionless turbulent kinetic energy dissipation,  $\varepsilon$  for different flows.

Case	$K_{LES}/u_\tau$	$\left(\frac{\delta\varepsilon}{u_\tau^3}\right)_{x_3=\delta}^{1/4}$
Pressure gradient-driven	0.049	0.309
$La_t = \infty$	0.066	0.882
$La_t = 1.0, \lambda = 6H$	0.081	0.860
$La_t = 0.7, \lambda = 6H$	0.097	0.854
$La_t = 0.7, \lambda = 4H/3$	0.120	0.859
$La_t = 0.4, \lambda = 6H$	0.137	0.849

In Figure 7.5, TKE dissipation rates for different flows are plotted near the surface. For wind driven flows with and without LC, values of TKE dissipation rates are very close to each other at the surface (i.e. at  $x_3/\delta = 1$ ). Note that LC is an inviscid process, thus dissipation at the surface is not influenced by the presence of LC. Moreover, TKE dissipation



rate ( $\varepsilon$ ) slightly decreases as we go from pressure gradient driven flow to wind driven flows with and without LC. From Eqn. 7.13, we see that decreasing  $\varepsilon$  leads to a decrease in transfer velocity (recall that the LES was predicting an increase). Because of this and since there is no significant difference between wind-driven flows in terms of  $\varepsilon$  at the surface, the small eddy model prediction does not line up with the LES result in wind driven flows. See Table 7.2 also for LES results and values of  $\varepsilon$  at the surface.

#### 7.1.4 Surface Divergence Model

McCready et al. [58] and Banerjee et al. [4] considered surface divergence as the key mechanism of mass exchange and they considered surface renewal time scale as

$$\tau_r \propto \langle \beta^2 \rangle^{-1/2} \quad (7.14)$$

where  $\beta = -\partial u'_3 / \partial x_3$  evaluated at the surface. Note that  $\beta = -\partial u'_3 / \partial x_3 = \partial u'_1 / x_1 + \partial u'_2 / x_2$  which is the surface divergence. Also note that both McCready et al. [58] and Banerjee et al. [4] did not consider Langmuir turbulence in their studies.

Inserting Eqn. 7.14 into Eqn. 7.2 gives

$$K \propto \left( \frac{D}{\langle \beta^2 \rangle^{-1/2}} \right)^{1/2} \quad (7.15)$$

Expression in Eqn. 7.14 is inspired from the Taylor series expansion to describe the vertical velocity in the concentration boundary layer. One can write the vertical velocity

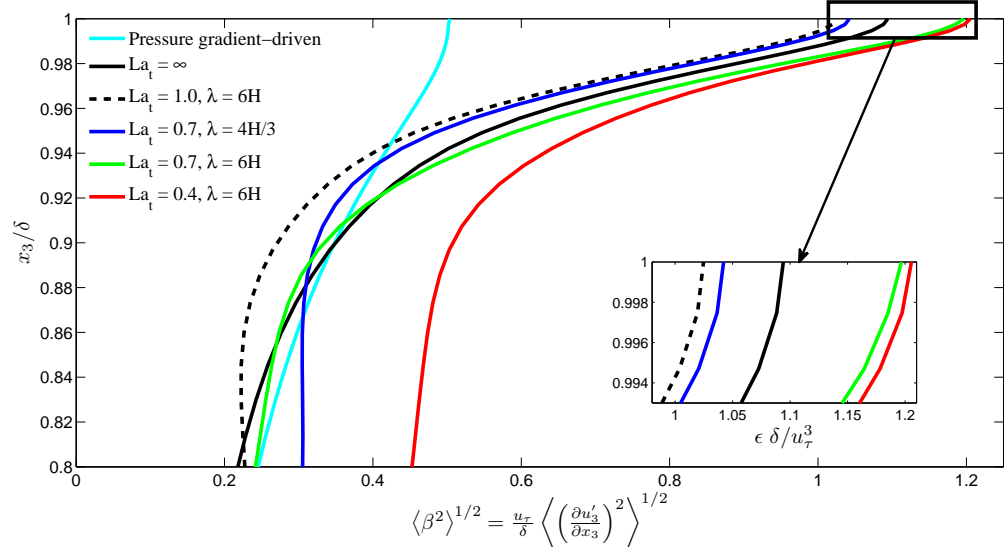


Figure 7.7:  $\langle \beta^2 \rangle^{1/2}$  for different flows.

fluctuations near the surface using Taylor expansion as [59]

$$u'_3(t, x_1, x_2, x_3) = u'_3(t, x_1, x_2, x_3^s) + \frac{\partial u'_3}{\partial x_3} \Big|_s [x_3 - x_3^s] + \frac{\partial^2 u'_3}{\partial x_3^2} \Big|_s \frac{[x_3 - x_3^s]^2}{2!} + \dots \quad (7.16)$$

where the superscript 's' shows the quantity that is computed at the surface,  $x_3 = \delta$ . Note that  $u_3(x_3 = \delta) = 0$  because of the boundary condition. Thus, the equation above becomes

$$u'_3(x_3) \approx \frac{\partial u'_3}{\partial x_3} \Big|_s [x_3 - x_3^s] = \beta [x_3 - x_3^s] \quad (7.17)$$

and thus  $\beta^{-1}$  at the surface may serve as a characteristic time scale for surface renewal as shown in Eqn. 7.14.  $\langle \beta^2 \rangle^{1/2}$  for different flows is depicted in Fig. 7.7. Although this quantity increases with decreasing  $La_t$  in the middle of the domain, it starts to decrease as we approach the surface and the values get close to each other for different flows (See Table 7.3). Transfer velocity values obtained via surface divergence model are compared

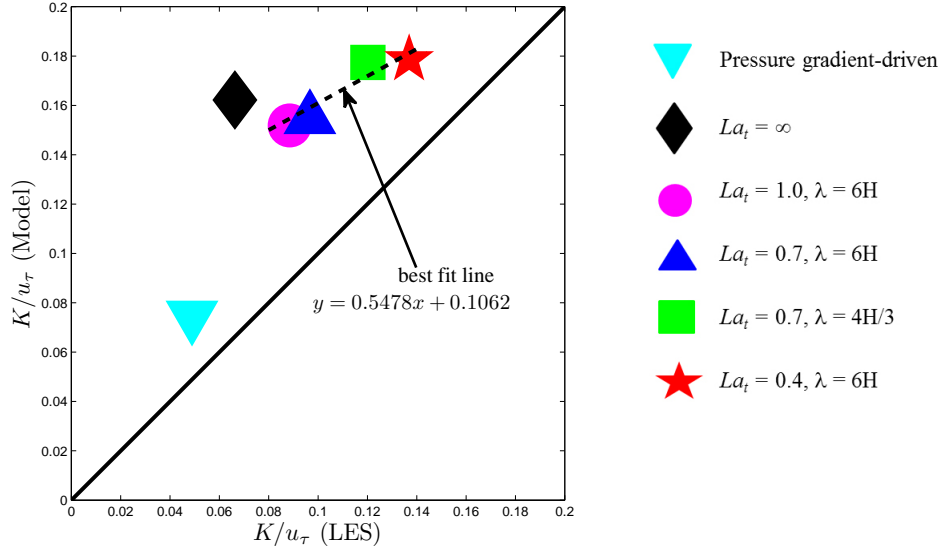


Figure 7.8: Comparison of transfer velocity evaluated through surface divergence model based on surface renewal theory with LES results.

Table 7.3: Values of surface divergence at the surface for different flows.

Case	$K_{LES}/u_\tau$	$\left(\frac{u_\tau^2 \langle \tilde{\beta}^2 \rangle}{\delta^2}\right)_{x_3=\delta}^{1/4}$
Pressure gradient-driven	0.049	2.089
$La_t = \infty$	0.066	4.540
$La_t = 1.0, \lambda = 6H$	0.081	4.252
$La_t = 0.7, \lambda = 6H$	0.097	4.324
$La_t = 0.7, \lambda = 4H/3$	0.120	4.966
$La_t = 0.4, \lambda = 6H$	0.137	5.002

to transfer velocity evaluated directly in LES in Fig. 7.8. From Eqn. 7.15, we see that with decreasing  $\langle \beta^2 \rangle^{1/2}$ , transfer velocity increases. The surface divergence model is able to correctly predict an increase in  $K$  with increasing coherency of LC (i.e. with decreasing  $La_t$ ). Furthermore, for a fixed  $La_t$ , this model is able to correctly predict the increasing trend in  $K$  with decreasing  $\lambda$ . However, the transfer velocity predicted by the surface divergence model is greater in wind driven flow without LC than in wind driven flows with LC (with  $La_t = 0.7$  and  $La_t = 1.0$ ). This results from the fact that  $\langle \beta^2 \rangle^{1/2}$  in the latter is smaller than

than in the former (See Fig. 7.7). Finally, note that the surface divergence model performs well for pressure gradient driven flow.

### 7.1.5 Errors

Comparisons of  $K$  predicted by models versus  $K$  recorded in LES are shown in Figs. 7.2 (Stokes drift shear model), 7.4 (large eddy model), 7.6 (small eddy model) and 7.8 (surface divergence model) of the dissertation. The average relative errors in these models are 36, 18, 29 and 22 percent, respectively. These errors are misleading. For example, the Stokes drift shear model has a higher average relative error than the small eddy model. However, from looking at Figure 7.5, it is clear that the dissipation of turbulent kinetic energy (TKE) at the surface (the key component in the small eddy model) has practically no correlation with the transfer velocity calculated in the LES, given that the slope of the best-fit line through the data points is negative. In other words, values of  $K$  predicted by the small eddy model are all nearly the same for all flows with LC characterized by different combinations of  $\lambda$  and  $La_t$ . However, as can be seen from the LES-computed  $K$  values,  $K$  depends strongly on  $\lambda$  and  $La_t$ . Thus, surface TKE dissipation rate should not be used as an indicator/measure of the impact of LC on  $K$ . On the other hand, the Stokes drift shear model is able to correctly capture the trends in  $K$  with changes in  $\lambda$  and  $La_t$ , yet it has the highest average relative error out of all the models considered. Although the present form of the Stokes drift shear model may not lead to accurate prediction of  $K$ , results do show that the Stokes drift shear model may be used as an indicator/measure of the impact of LC on  $K$ . Perhaps a  $K$  model based on a non-linear relationship with Stokes drift shear should

be proposed. Proper calibration of coefficients in such a model would require a suite of simulations covering a wide range of  $\lambda$  and  $La_t$  values.

## 7.2 Chapter Summary

In this chapter, four different parameterizations of transfer velocity were tested via comparison with transfer velocity obtained directly in the LES. Statistical analysis of LES results (presented in Chapter 5 and Chapter 6) showed that in wind-driven flows with LC both near surface small eddies and full-depth LC co-exist. In the absence of LC, near-surface small eddies contribute towards the mass transport at the air-water interface. The effect of these eddies is diminished by the presence of full-depth LC, especially within the upwelling limb of the cell.

The surface transfer velocity predicted by the large eddy model of Gulliver & Halverson [31]) based on surface renewal time scale given by characteristics of large streamwise vortices such as LC was found to be well-correlated with transfer velocity predicted by the LES for a fixed wavelength ( $\lambda$ ). However, this model predicts a decrease in transfer velocity for shorter wavelengths while keeping  $La_t$  fixed, whereas transfer velocity evaluated via LES predicts an increase.

Our results also indicated that even though the strength of LC becomes less intense for shorter wavelengths, Stokes drift shear increases at the surface and causes a disruption of near surface dynamics as large as in flows with stronger LC. Based on this fact, we introduced and tested a Stokes drift shear model which was able to capture the increasing trend in transfer velocity both with decreasing  $La_t$  and shorter wavelengths.

Furthermore, an increasing trend of LES-computed surface transfer velocity with increasing surface divergence magnitude was observed for sufficiently coherent large-scale structures, but not necessarily for the weakest of these structures. Finally, dissipation rate of turbulent kinetic energy at the surface associated with small scale eddies in LES of flows with LC did not correlate with transfer velocity evaluated directly in the LES.

## Chapter 8:

### Conclusions

In this dissertation a number of simulations varying surface gravity wave wavelength ( $\lambda$ ), turbulent Langmuir number ( $La_t$ ), Reynolds numbers ( $Re$ ) and Schmidt number ( $Sc$ ) have been performed in an attempt to gain understanding of the impact of Langmuir cells on near surface scalar transfer and also on scalar transport throughout the water column. Near surface scalar (gas) transfer has drawn considerable attention since significant amount of man-made  $CO_2$  (a sparingly soluble greenhouse gas) is absorbed by the oceans. Although there are numerous studies of scalar exchange that have focused on near-surface turbulence characteristics such as wind shear, wave-breaking etc., the effect of Langmuir cells have not been considered in these studies before.

In Chapter 5, we presented turbulence structure, mean velocity and as well as TKE budget results in large eddy simulation of full-depth LC in pressure gradient-driven flow and in wind driven flows with and without LC. The wind driven case with LC with  $La_t = 0.7$  and  $\lambda = 6H$  represents the conditions during field measurements of shallow water, full-depth LC of Gargett et al. [28] and Gargett & Wells [27]. This LES was shown to be able to capture the large-scale turbulent structure measured in the field (See Tejada- Martínez & Grosch [86] and Tejada-Martínez et al. [87]). Present simulations showed that for wind-driven flow with LC with ( $La_t = 0.7$ ,  $\lambda = 6H$ ) Langmuir turbulence leads to an increase

in transfer velocity (a measure of transfer efficiency across the air-water interface) by 46% relative to wind-driven flow without LC.

In general, we saw that decreasing  $La_t$  leading to more intense LC, while holding  $\lambda$  fixed, leads to higher transfer velocity. Moreover, for a fixed value of  $La_t$ , decreasing  $\lambda$  (i.e. shorter surface wave wavelength) leads to weaker LC characterized by intense surface convergence and downwellings. As emphasized in several chapters, shorter waves induce higher Stokes drift shear. Thus, even though the LC is weaker for smaller  $\lambda$ , vertical velocity fluctuations are enhanced which in return can increase transfer velocity.

We have found that, LC causes a deviation from classical log-law behavior in terms of mean downwind velocity and production and dissipation rates of TKE. The disruption or deviation is inversely proportional to  $La_t$  and  $\lambda$ , i.e. smaller  $La_t$  (for a fixed  $\lambda$ ) and smaller  $\lambda$  (for a fixed  $La_t$ ) leads to greater disruption.

Our LES results showed that in wind driven flows with LC, large scale eddies (i.e. full depth LC) are a major contributor to scalar transport at the surface as impact of near surface small eddies on near surface scalar transport tends to be diminished although still important. Specifically, around the mid-span region full-depth LC downwelling limb plays a more dominant role in scalar transport than the near surface small scale vortices. Everywhere else near surface small scale vortices are well-correlated with scalar transport.

In Chapter 7.1, transfer velocity results obtained from four different models were compared to transfer velocity obtained directly from our LES. This comparison is summarized in Fig. 8.1.

A model based on Stokes drift velocity shear at the surface was proposed based on statistical analysis of the turbulence in Chapter 6.1. Although the Stokes drift shear model



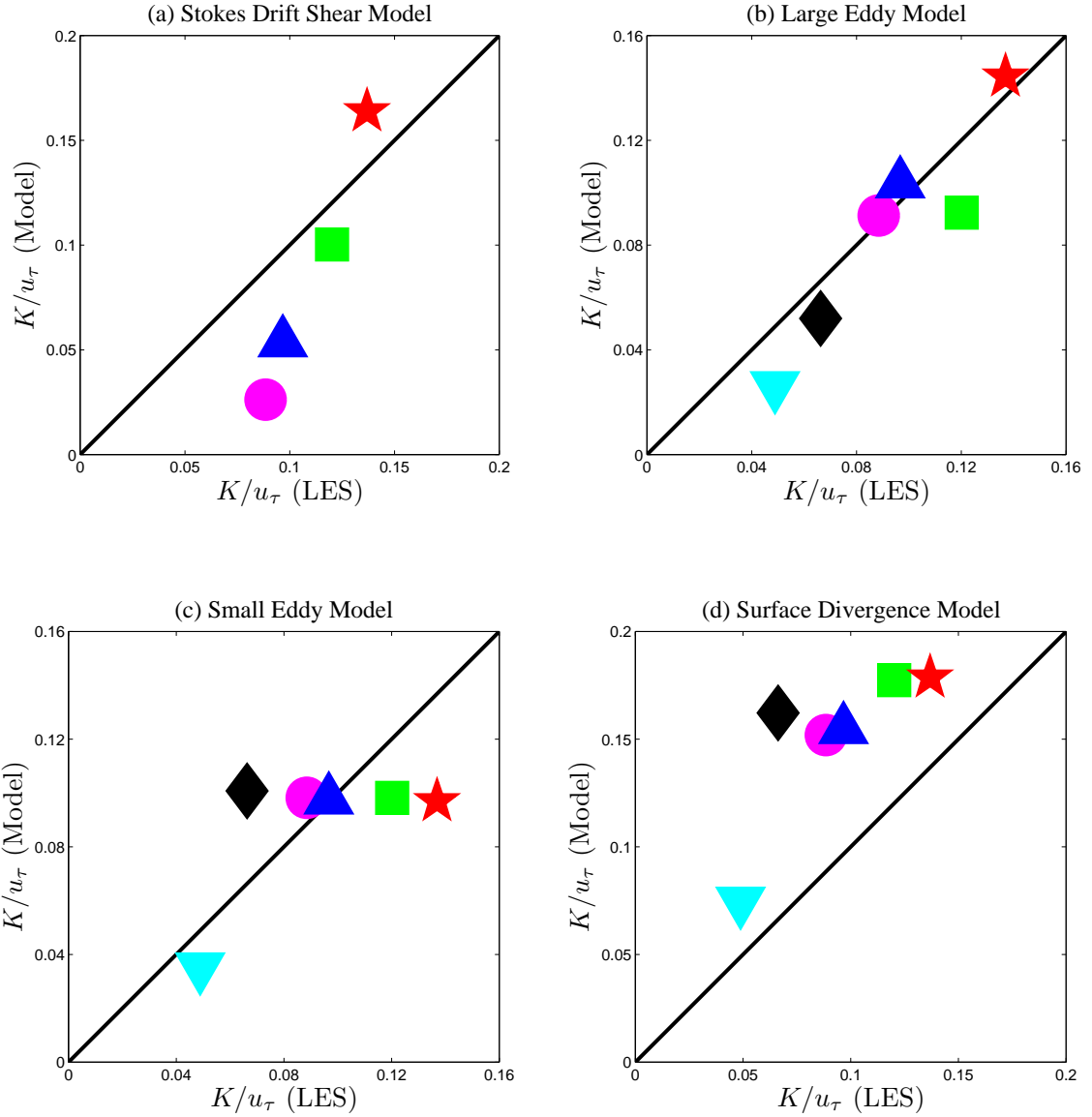


Figure 8.1: Comparison of transfer velocity evaluated through models based on surface renewal theory with LES results where cyan down triangle shows pressure gradient driven flow, black diamond shows  $La_t = \infty$ , magenta circle shows  $La_t = 1.0$ ,  $\lambda = 6H$ , blue up triangle shows  $La_t = 0.7$ ,  $\lambda = 6H$ , green square shows  $La_t = 0.7$ ,  $\lambda = 4H/3$  and red star shows  $La_t = 0.4$ ,  $\lambda = 6H$ .

is able to capture the trends with Langmuir turbulence, its average relative error is high. This suggests that perhaps a  $K$  model based on a non-linear relationship with Stokes drift shear should be proposed. Proper calibration of coefficients in such a model would require a suite of simulations covering a wide range of  $\lambda$  and  $La_t$  values, which should become feasible as computational power advances.

Large eddy model inspired by flume experiment results of Gulliver and Halverson [31] performed well while holding  $\lambda$  fixed but when tested for a different  $\lambda$ , this model seemed to underpredict the results as it is mainly based on the coherency of LC and LC becomes less intense with decreasing  $\lambda$ .

Surface divergence model is also able to capture the increase in transfer velocity in wind driven flows with LC. Nevertheless, this model predicts a higher transfer velocity value for wind driven flow without LC than in two flows with LC which is not consistent with our LES results.

Lastly, the small eddy model that is based on the TKE dissipation rate at the surface is not well-correlated with transfer velocity evaluated via LES when LC is present.

We have seen that increase in transfer velocity between these flows does not depend greatly on Reynolds number (see Appendix G). Further tests should be performed in the future as greater computational power allows for LES at higher Reynolds number. Moreover, our results from wind driven flows with LC obeys the theoretical law,  $K = Sc^{-0.5}$ . This was shown for cases with  $Sc = 1$  and  $Sc = 5$  (see Appendix F). As greater computational power becomes more accessible, LES with higher values of Schmidt number should be performed to further confirm this.

## 8.1 Future Work

As discussed in Section 4.3, results from (i) pressure gradient-driven flow and (ii) wind driven flow with and without LC are presented where the domain considered is in a shallow water region. Results from same type of flows have been recently obtained for deep water region but have not been analyzed yet. In shallow water LC extends over the full depth of water column whereas in deep water these cells extend to the depth of surface mixed layer, and not to the full depth of water column. The effect of LC on air-water mass transfer in deep water has not been studied before and will be the focus of future research.

In this dissertation we tested several parameterizations, but we were not able identify a parameterization that has a good prediction for all of the flows we simulated (for example 8.1). Thus, future research will also focus on combining different parameterizations that will be able to capture effects of different oceanic processes successfully.

We were not able to perform computations at Schmidt numbers greater than 5. One possible solution to this problem might be using Lagrangian scalar tracking (LST). This method has been applied to heat transfer problems in direct numerical simulations (DNS) of turbulent channel flows [64–66, 82] and enabled researchers to study scalar transport at high Prandtl numbers. Future research will also focus on implementing a technique such as LST to obtain results for higher Schmidt numbers.

The results of this dissertation are purely computational. These results suggest that future research should focus on making simultaneous field measurements of gas transfer across the air-sea interface and LC in order to understand the relative impact of Langmuir

turbulence on transfer velocity with respect to other processes such as micro-scale wave-breaking and full-scale wave-breaking.

Finally, computational results reported in this work were obtained using C-L vortex force parameterizing the interaction between surface wave-driven Stokes drift velocity and wind-driven shear current. This interaction generates LC and associated Langmuir turbulence. As computational power increases, future simulations should be performed resolving surface waves and thus resolving the LC generating mechanism directly without use of the C-L vortex force.

## References

- [1] S.W. Armfield and R. Street. Fractional step methods for the navier-stokes equations on non-staggered grids. *ANZIAM J.*, 42(E):C134–C156, 2000.
- [2] W. E. Asher, H. Liang, C. J. Zappa, M. R. Loewen, M. A. Mukto, T. M. Litchendorf, and A. T. Jessup. Statistics of surface divergence and their relation to air-water gas transfer velocity. *J. Geophys. Res.*, 117:C05035, 2012.
- [3] H. D. Baehr and K. Stephan. *Heat and Mass Transfer*. Springer, 2006.
- [4] S. Banerjee, D. Lakehal, and M. Fulgosi. Surface divergence models for scalar exchange between turbulent streams. *Int. J. Multiphase Flow*, 30(30):963–977, 2004.
- [5] S. Banerjee, D. S. Scott, and E. Rhodes. Mass transfer to falling wavy liquid films in turbulent flow. *Ind. Eng. Chem. Fundamentals*, 7:22–27, 1968.
- [6] Y. Bazilevs, V.M. Calo, J. A. Cottrell, T. J. R. Hughes, A. Reali, and G. Scovazzi. Variational multiscale residual-based turbulence modeling for large eddy simulation of incompressible flows. *Comput. Method Appl. M.*, 197:173–201, 2007.
- [7] J. Boutin, J. Etcheto, Merlivat L., and Y. Rangama. Influence of gas exchange coefficient parameterisation on seasonal and regional variability of co2 air-sea fluxes. *Geophys. Res. Lett.*, 29(8):1182, 2002.
- [8] P. Bradshaw. The best turbulence models for engineers. In M.D. Salas, J. N. Hefner, and L. Sakell, editors, *Modeling Complex Turbulent Flows - ICASE 1997 Symposium*. Kluwer, 1999.
- [9] I. Calmet and J. Magnaudet. Large eddy simulation of high-schmidt number mass transfer in a turbulent channel flow. *Phys. Fluids*, 9:438–455, 1997.
- [10] I. Calmet and J. Magnaudet. High-schmidt number mass transfer through turbulent gas-liquid interfaces. *Int. J. Heat Fluid Flow*, 19:522–532, 1998.

- [11] I. Calmet and J. Magnaudet. Statistical structure of high-reynolds-number close to the free surface of an open-channel flow. *J. Fluid Mech.*, 474:355–378, 2003.
- [12] M.H. Carpenter, D. Gottlieb, and S. Abarbanel. The stability of numerical boundary treatments for compact high-order finite difference schemes. *J. Comput. Phys.*, 108:272–292, 1993.
- [13] J. Castanga and Y. Yao. Development of a multi-block high-order dns code for turbulent flow simulations. In *IOP Conference Series: Materials Science and Engineering*, volume 10, pages 1757–8981, 2010.
- [14] A. D. D. Craik and S. Leibovich. A rational model for langmuir circulation. *J. Fluid Mech.*, 73:401–426, 1976.
- [15] P.V. Danckwerts. Significance of liquid-film coefficients in gas absorbtion. *Ind. Eng. Chem.*, 43:1460–1467, 1951.
- [16] B. Debusschere and C.J. Rutland. Turbulent scalar transport nechanisms in plane channel and couette flows. *Int. J. Heat Mass Transfer*, 47:1771–1781, 2004.
- [17] P. E. Dimotakis, R. C. Miake-Lye, and D. A. Papantoniou. Structure and dynamics of round turbulent jets. *Phys. Fluids*, 26:3185–3192, 1983.
- [18] M. A. Donelan and R. Wanninkhof. *Gas Transfer at Water Surfaces: Concepts and Issues*, volume 127. Geophys. Monogr. Ser., AGU, Washington, D. C, 2002.
- [19] S. Doney. Irreversible thermodynamics and air-sea exchange. *J. Geophys. Res.*, 100:8541–8553, 1995.
- [20] S. Doney. Marine chemistry: Dissolved gases and air-sea exchange. <http://ocw.mit.edu/courses/earth-atmospheric-and-planetary-sciences/12-742-marine-chemistry-fall-2006/lecture-notes/>, 2006.
- [21] S.C. Doney. The dangers of ocean acidification. *Scientific American*, 294:58–65, 2006.
- [22] Y.H Dong, X.Y. Lu, and L.X. Zhuang. Large eddy simulation of turbulent channel flow with mass transfer at high-schmidt numbers. *Int. J. Heat Mass Transfer*, 46:1529–1539, 2003.
- [23] P.A. Durbin and B.A. Petterson Reif. *Statistical Theory and Modeling for Turbulent Flow*. Wiley, 2 edition, 2011.

- [24] A.J. Faller and E.A. Caponi. Laboratory studies of wind-driven langmuir circulations. *J. Geophys. Res.*, 83:3617–3633, 1978.
- [25] O.B. Fringer, S.W. Armfield, and R. L. Street. A nonstaggered curvilinear grid pressure correction method applied to interfacial waves. In *2nd International Conference on Heat Transfer, Fluid Mechanics, and Thermodynamics (HEFAT)*, page FO1, Victoria Falls, Zambia, 2003.
- [26] A.E. Gargett and D.K. Savidge. The role of langmuir supercells in seasonally tuned cross-shelf transport of bioactive material. In *Abstracts, AGU Ocean Sciences Meeting*, Orlando, Florida, 2008.
- [27] A.E. Gargett and J.R. Wells. Langmuir turbulence in shallow water: Part i. observations. *J. Fluid Mech.*, 576:27–61, 2007.
- [28] A.E. Gargett, J.R. Wells, A.E. Tejada-Martínez, and C.E. Grosch. Langmuir supercells: a mechanism for sediment resuspension and transport in shallow seas. *Science*, 306:1925–1928, 2004.
- [29] B. Geurts. *Elements of Direct and Large Eddy Simulatio*. Edwards, 2004.
- [30] C. Gualtieri and D.P. Doria. *Fluid Mechanics of Environmental Interfaces*. Taylor and Francis, 2008.
- [31] J. S. Gulliver and M. J. Halverson. Air-water gas transfer in open channels. *Water Resources Res.*, 25:1783–1793, 1989.
- [32] J.M. Hamilton, J. Kim, and F. Waleffe. Regeneration mechanisms of near-wall turbulence structures. *J. Fluid Mech.*, 287:317–348, 1995.
- [33] R. R. Harcourt and E. A. D’Asaro. Large-eddy simulation of langmuir turbulence in pure wind seas. *J. Phys. Oceanogr.*, 38:1542–1562, 2007.
- [34] Y. Hasegawa and N. Kasagi. The effect of schmidt number on air-water interface mass transfer. In *Proc. 4th Int. Conf. on Multiphase Flow*, 2001.
- [35] R. Higbie. The rate of absorption of a pure gas into a still liquid during a short time of exposure. *Trans. Am. Inst. Chem. Eng.*, 31:365–389, 1935.
- [36] D.D. Holm. The ideal craik-leibovich equations. *Physica D: Nonlinear Phenomena*, 98:415–441, 1996.

- [37] T. J. R. Hughes, J. A. Cottrell, and Y. Bazilevs. Isogeometric analysis: Cad, finite elements, nurbs, exact geometry and mesh refinement. *Comput. Method Appl. M.*, 194:4135–4195, 2005.
- [38] R. E. Hunter and G. W. Hill. Nearshore current pattern off south texas - an interpretation from aerial photographs. *Remote Sens. Environ.*, 10:115–134, 1980.
- [39] B. Jahne and H. Haussecker. Air-water gas exchange. *Annu. Rev. Fluid Mech.*, 30(1):443–468, 1998.
- [40] B. Jahne, P. Libner, R. Fischer, T. Billen, and E. J. Plate. Investigating the transfer processes across the free aqueous viscous boundary layer by the controlled flux method. *Tellus*, 41B:177–195, 1989.
- [41] B. Jahne, K. O. Munnich, R. Bosinger, A. Dutzi, W. Huber, and P. Libner. On the parameters influencing air-water gas exchange. *J. Geophys. Res.*, 92(C2):1937–1949, 1987.
- [42] X. Jiang and C.-H. Lai. *Numerical Techniques for Direct and Large-Eddy Simulations*. CRC, 2009.
- [43] J Jiménez and A. Pinelli. The autonomous cycle of near-wall turbulence. *J. Fluid Mech.*, 389:335–359, 1999.
- [44] T. Kawamura. Numerical investigation of turbulence near a sheared air-water interface. part 2: Interaction of turbulent shear flow with surface waves. *J. Mar. Sci. Technol.*, 5:161–175, 2000.
- [45] J. Kim, P. Moin, and R. Moser. Turbulence statistics in fully developed channel flow at low reynolds number. *J. Fluid Mech.*, 177:133–166, 1987.
- [46] S. J. Kline, W.C. Reynolds, F.A. Schraub, and P.W. Runstadler. The structure of turbulent boundary layers. *J. Fluid Mech.*, 30:741–773, 1967.
- [47] T. Kukulka, A.J. Plueddemann, J.H. Trowbridge, and P.P. Sullivan. Significance of langmuir circulation in upper ocean mixing: Comparison of observations and simulations. *Geophys. Res. Lett.*, 36:L10603, 2009.
- [48] J. C. Lamont and D. S. Scott. An eddy cell model of mass transfer into the surface of a turbulent liquid. *AIChE J.*, 16(4):513–519, 1970.



- [49] I. Langmuir. Surface motion of water induced by wind. *Science*, 87:119–123, 1938.
- [50] P.H. Leblond and L.A. Mysak. *Waves in the Ocean*. Elsevier, 1978.
- [51] S. K. Lele. Vorticity form of turbulence transport equations. *Phys. Fluids*, 4:1767–1772, 1992.
- [52] A. Leonard. Energy cascade in large eddy simulation of turbulent fluid flow. *Adv. Geophys.*, 18A:237–248, 1974.
- [53] W.K. Lewis and W. Whitman. Principles of gas absorption. *Ind. Eng. Chem.*, 16:1215–1224, 1924.
- [54] M. Li, C. Garrett, and E. Skillingstad. A regime diagram for classifying turbulent large eddies in the upper ocean. *Deep-Sea Res. Part I*, 52(259-278):259–278, 2005.
- [55] P. S. Liss and L. Merlivat. Air-sea gas exchange rates: introduction and synthesis. In P.B. Menard, editor, *The Role of Air-sea Exchange in Geochemical Cycling*, pages 113–128. D.Reidel Publishing Company, Dordrecht, 1986.
- [56] J. Malm, P. Schlatter, and N.D. Sandham. A vorticity stretching diagnostic for turbulent and transitional flows. *Theor. Comput. Fluid Dyn.*, 1:1–15, 2011.
- [57] G. O. Marmorino, G. B. Smith, and G. J. Lindemann. Infrared imagery of large-aspect-ratio langmuir circulation. *Cont. Shelf Res.*, 25:1–6, 2004.
- [58] M.J. McCready, E. Vassiliadou, and T.J. Hanratty. Computer simulation of turbulent mass transfer at a mobile interface. *AIChE J.*, 32(7):1108–1115, 1986.
- [59] McGillis W.R. McKenna, S.P. *Gas Transfer at Water Surfaces: Concepts and Issues*, volume 127, chapter Surface divergence and air-water gas transfer, pages 129–134. Geophys. Monogr. Ser., AGU, Washington, D. C, 2002.
- [60] J. C. McWilliams, P. P. Sullivan, and C.-H. Moeng. Langmuir turbulence in the ocean. *J. Fluid Mech.*, 334:1–30, 1997.
- [61] F.M. Najjar and D.K. Tafti. Study of discrete test filters and finite difference approximations for the dynamic subgrid-scale stress model. *Phys. Fluids*, 8(4):1076–1088, 1996.

- [62] P. D. Nightingale, G. Malin, C.S. Law, A.J. Watson, P.S. Liss, M.I. Liddicoat, J. Boutin, and R. C. Upstill-Goddard. In-situ evaluation of air-sea gas exchange parameterisations using novel conservative and volatile tracers. *Global Biogeochem. Cycles*, 14:373–387, 2000.
- [63] Y. Noh, H. S. Min, and S. Raasch. Large eddy simulation of the ocean mixed layer: The effects of wave breaking and langmuir circulation. *J. Phys. Ocean.*, 34:720–735, 2004.
- [64] D. V. Papavassiliou. Scalar dispersion from an instantaneous line source at the wall of a turbulent channel for medium and high prandtl number fluids. *Int. J. Heat Fluid Flow*, 23:161–172, 2002.
- [65] D.V. Papavassiliou and T.J. Hanratty. The use of lagrangian methods to describe turbulent transport of heat from a wall. *Ind. Eng. Chem.*, 34:3359–3367, 1995.
- [66] D.V. Papavassiliou and Hanratty T.J. Interpretation of large-scale structures observed in a turbulent plane couette flow. *Int. J. Heat Fluid Flow*, 18:55–69, 1997.
- [67] O. M. Phillips. *Dynamics of the Upper Ocean*. Cambridge Univ. Press, 1967.
- [68] S.B. Pope. *Turbulent Flows*. Cambridge University Press, Cambridge, U.K., 2000.
- [69] C. Pozrikidis. *Fluid Dynamics: Theory, Computation*,. Springer, 2 edition, 2009.
- [70] C Rader. Discrete fourier transforms when the number of data samples is prime. *Proceedings of the IEEE*, 56:1107–1108, 1968.
- [71] A. Rasheed. Turbulence modeling: Large eddy simulation. web, May 2011.
- [72] K. Richter and B. Jahne. A laboratory study of the schmidt number dependency of air-water gas transfer. In W. & Kurose R. Komori, S.; McGillis, editor, *Gas Transfer at Water Surfaces 2010*. Kyoto University Press, 2011.
- [73] P. Sagaut. *Encyclopedia of Computational Mechanics*, volume 3. Wiley, 2004.
- [74] P. Sagaut. *Large-Eddy Simulation for Acoustics*. Cambridge Univ. Press, 2007.
- [75] J.T. Scott, G.E. Myer, R. Stewart, and E.G. Walther. On the mechanism of langmuir circulations and their role in epilimnion mixing. *Limnol. Oceanogr.*, 14:493–503, 1969.

- [76] E. D. Skillingstad, W. D. Smyth, J. N. Moum, and H. Wijesekera. Upper-ocean turbulence during a westerly wind burst: A comparison of large-eddy simulation results and microstructure measurements. *J. Phys. Oceanogr.*, 29:5–28, 1999.
- [77] E.D. Skillingstad and D.W. Denbo. An ocean large-eddy simulation of langmuir circulations and convection in the surface mixed layer. *J. Geophys. Res.*, 100(C5):8501–8522, 1995.
- [78] D. N. Slinn and J. J. Riley. A model for the simulation of turbulent boundary layers in an incompressible stratified flow. *J. Comput. Phys.*, 144:550–602, 1998.
- [79] C.R. Smith and S.P. Metzler. The characteristics of low-speed streaks in the near-wall region of the turbulent boundary layer. *J. Fluid Mech.*, 129:27–54, 1983.
- [80] J.A. Smith. *Fluid Mechanics and the Environment: Dynamical Approaches*, volume 566, chapter Observations and theories of Langmuir circulation: a story of mixing, pages 295–314. Springer, 2001.
- [81] Y. Socolofsky and G.H. Jirka. Environmental fluid mechanics 1: Mass transfer and diffusion. Lecture Notes.
- [82] C. Srinivasan and D. V. Papavassiliou. Prediction of turbulent prandtl number in wall flows with lagrangian simulations. *Ind. Eng. Chem. Res.*, 50(15):8881–8891, 2011.
- [83] P. P. Sullivan, J. C. McWilliams, and W. K. Melville. The oceanic boundary layer driven by wave breaking with stochastic variability, part 1. direct numerical simulations. *J. Fluid Mech.*, 507:143–174, 2004.
- [84] T. Takahashi, S.C. Sutherland, R. Wanninkhof, C. Sweeney, R.A. Feely, D.W. Chipman, B. Hales, Friederich. G., Chavez F., C. Sabine, A. Watson, D.C.E. Bakker, U. Schuster, N. Metzl, H. Yoshikawa-Inoue, M. Ishii, T. Midorikawa, Y. Nojiri, A. Körtzinger, T. Steinhoff, Hoppema. M., J. Olafsson, T.S. Arnarson, B. Tilbrook, T. Johannessen, A. Olsen, R. Bellerby, C.S. Wong, B. Delille, N.R. Bates, and H.J.W. de Baar. Climatological mean and decadal change in surface ocean pco<sub>2</sub>, and net sea-air co<sub>2</sub> flux over the global oceans. *Deep Sea Research Part II: Topical Studies in Oceanography*, 56(8-10):554 – 577, 2009.
- [85] A. Tejada-Martínez. *Dynamic subgrid-scale modeling for large-eddy simulation of turbulent flows with a stabilized finite element method*. PhD thesis, Rensselaer Polytechnic Institute, November 2002.

- [86] A.E. Tejada-Martínez and C.E. Grosch. Langmuir turbulence in shallow water: Part ii. large-eddy simulation. *J. Fluid Mech.*, 576:63–108, 2007.
- [87] A.E. Tejada-Martínez, C.E. Grosch, A.E. Gargett, J.A Polton, J.A. Smith, and J.A. MacKinnon. A hybrid spectral/finite-difference large-eddy simulator of turbulent processes in the upper ocean. *Ocean Model.*, 30:115–142, 2009.
- [88] M. Tennekes and J.L. Lumley. *A First Course in Turbulence*. The MIT Press, 1972.
- [89] S.A. Thorpe. Langmuir circulation. *Annu. Rev. Fluid Mech.*, 36:55, 2004.
- [90] W.-T. Tsai. On the formation of streaks on wind-driven water surfaces. *Geophys. Res. Lett.*, 28(20):3959–3962, 2001.
- [91] W.-T. Tsai, S.-M. Chen, M.-Y. Lin, and L.-P. Hung. Molecular sublayers beneath the air-sea interface relative to momentum, heat and gas transports. *Geophys. Res. Lett.*, 30(18):1969, 2003.
- [92] W.-T. Tsai, S.-M. Chen, and C.-H. Moeng. A numerical study on the evolution and structure of a stress-driven, free-surface turbulent shear flow. *J. Fluid Mech.*, 545:163–192, 2005.
- [93] M. van Dyke. *An Album of Fluid Motion*. The Parabolic Press, 1982.
- [94] R. Wanninkhof. Relationship between wind speed and gas exchange over the ocean. *J. Geophys. Res.*, 97:7373–7382, 1992.
- [95] R. Wanninkhof, W.E. Asher, D.T. Ho, C.S. Sweeney, and W.R. McGillis. Advances in quantifying air-sea gas exchange and environmental forcing. *Annu. Rev. Mar. Sci.*, 1:213–244, 2009.
- [96] R. Wanninkhof and W.R. McGillis. A cubic relationship between air-sea co<sub>2</sub> exchange and wind speed. *Geophys. Res. Lett.*, 26:1889–1892, 1999.
- [97] B. Ward, R. Wanninkhof, W. R. McGillis, A. T. Jessup, M. D. DeGrandpre, J. E. Hare, and J. B. Edson. Biases in the air-sea flux of co<sub>2</sub> resulting from ocean surface temperature gradients. *J. Geophys. Res.*, 109:C08S08, 2004.
- [98] D.C. Wilcox. *Turbulence Modeling for CFD*. DCW. Industries Inc., La Canada, CA, 1994.

- [99] Z.F. Xu, B.C. Khoo, and Carpenter K. Mass transfer across the turbulent gas-water interface. *AIChE J.*, 52(10):3363–3374, 2006.
- [100] C.J. Zappa, W.R. McGillis, P. A. Raymond, J. B. Edson, E. J. Hints, H. J. Zemelink, J. W. Dacy, and D. T Ho. Environmental turbulent mixing controls on air-water gas exchange in marine and aquatic systems. *Geophys. Res. Lett.*, 34:L10601, 2007.

## **Appendices**

## Appendix A: Numerical Method

In this dissertation, we used spectral methods in the horizontal direction and higher order finite differences in the vertical direction for spatial discretization. The reason for this is the accuracy afforded by these methods, especially in their good approximation of the smaller resolved scales (see Section A.5 for detailed discussion).

Temporal and spatial discretization methods used for this dissertation are given in detail in Sections A.2 and A.2 and accuracy of the methods are discussed in Section A.5.

### A.1 Temporal Discretization

Armfield [1] investigated the solution of N-S equations on a non-staggered grid using a semi-implicit fractional step method. This method requires momentum equations to be solved first and then the some form of a Poisson equation for pressure. Since the Poisson equation is obtained using the continuity and momentum equations, the solution of this equation provides the pressure and also acts to enforce continuity.

#### A.1.1 Momentum Equation

We describe this solution procedure following closely Tejada-Martínez and Grosch [86] and Tejada-Martínez et al. [87]. For simplicity, the advection, gradient of the subgrid-scale stress and the C-L vortex force terms (in Eqn. 4.5) are gathered into function  $H_i$  as

$$H_i(\bar{u}_k) = \bar{u}_j \frac{\partial \bar{u}_i}{\partial x_j} - \frac{\partial \tau_{ij}^d}{\partial x_j} - \varepsilon_{ijk} \frac{1}{La_\tau^2} \phi_j^2 \bar{\omega}_k \quad (\text{A.1})$$

## Appendix A: (Continued)

Using vector notation (i.e.  $\bar{\mathbf{u}} = (\bar{u}_1, \bar{u}_2, \bar{u}_3)$ ,  $\nabla = (\partial_{x_1}, \partial_{x_2}, \partial_{x_3})$ ,  $\mathbf{H} = (H_1, H_2, H_3)$  and so on) the terms in Eqn. A.1 are explicitly discretized using the second-order time accurate Adams - Bashforth (A-B) scheme as

$$\mathbf{N}(\bar{\mathbf{u}}^n, \bar{\mathbf{u}}^{n-1}) = \frac{3}{2}\mathbf{H}(\bar{\mathbf{u}}^n) - \frac{1}{2}\mathbf{H}(\bar{\mathbf{u}}^{n-1}) \quad (\text{A.2})$$

where the superscripts refer to time steps  $n$  and  $n-1$ . Using the second-order time accurate Crank-Nicolson (C-N) scheme to discretize the viscous term (i.e. the term inversely proportional to  $Re_\tau$  in Eqn. 4.5) together with the previous A-B scheme, the discretized momentum equation may be re-expressed as

$$\left( \frac{1}{\Delta t} + \frac{1}{2Re} \nabla^2 \right) \Delta \bar{\mathbf{u}}_*^{n+1} = -N(\bar{\mathbf{u}}^n, \bar{\mathbf{u}}^{n-1}) + \frac{1}{Re} \nabla^2 \bar{\mathbf{u}}^n - \nabla \bar{\Pi}^n \quad \text{in } \Omega \quad (\text{A.3a})$$

$$\mathbf{t}_i \cdot \bar{\mathbf{u}}_*^{n+1} = 0 \quad \text{for } i = 1, 2 \quad \text{on } \partial\Omega_1 \quad (\text{A.3b})$$

$$(\mathbf{n} \cdot \nabla)(\bar{u}_{1*}^{n+1}, \bar{u}_{2*}^{n+1}) = (Re, 0) \quad \text{on } \partial\Omega_2 \quad (\text{A.3c})$$

$$\bar{\mathbf{u}}_*^{n+1} = \bar{\mathbf{u}}^n + \Delta \bar{\mathbf{u}}_*^{n+1} \quad \text{in } \Omega + \partial\Omega \quad (\text{A.3d})$$

where  $\bar{\mathbf{u}}_*^{n+1} = (\bar{u}_{1*}^{n+1}, \bar{u}_{2*}^{n+1}, \bar{u}_{3*}^{n+1})$ ,  $\Delta t$  is the time step,  $\mathbf{n}$  is the unit normal vector to either the bottom or top boundary,  $\partial\Omega_1$  denotes the bottom boundary and  $\partial\Omega_2$  denotes the top boundary. Furthermore,  $\Omega$  denotes the interior of the domain excluding the boundaries and  $\partial\Omega$  denotes both bottom and top boundaries. Note that the boundary condition in Eqn. A.3c is appropriate for the wind-driven shear flow configuration described earlier (Figure 4.1(a)). In the case of a pressure-gradient driven flow with zero stress at the surface (Figure



## Appendix A: (Continued)

4.1(b)), the right hand side of the  $x_1$  equation in A.3 is augmented by a constant body force (i.e. pressure gradient) driving the flow in the positive  $x_1$  direction. Furthermore, the boundary condition given in Eqn. A.3c is replaced by  $(\mathbf{n} \cdot \nabla)(\bar{u}_{1*}^{n+1}, \bar{u}_{2*}^{n+1}) = (0, 0)$ . Spatial discretization in  $x_3$  direction uses high-order finite differences which lets us using Dirichlet, Neumann or periodic boundary conditions at the top and bottom surfaces of our domain. In all our flows the boundary condition on  $x_3$  component of the velocity  $\bar{u}_{3*}^{n+1}$  is zero wherever we have Dirichlet or Neumann boundary conditions ([87]).

Vectors  $\mathbf{t}_1$  and  $\mathbf{t}_2$  are linearly independent unit vectors normal to  $\mathbf{n}$ . The solution of Equation A.3 at time  $t_{n+1}$ , intermediate solution  $\bar{\mathbf{u}}_*^{n+1}$ , does not satisfy the continuity equation. To enforce the divergence-free condition, the following Poisson equation for pressure is first solved:

$$\nabla^2(\Delta\bar{\Pi}^{n+1}) = \frac{1}{\Delta t} \nabla \cdot \bar{\mathbf{u}}_*^{n+1} \quad \text{in } \Omega + \partial\Omega \quad (\text{A.4a})$$

$$\frac{\partial \Delta\bar{p}^{n+1}}{\partial n} = \frac{1}{\Delta t} \mathbf{n} \cdot \bar{\mathbf{u}}_*^{n+1} \quad \text{on } \partial\Omega \quad (\text{A.4b})$$

$$\bar{\Pi}^{n+1} = \bar{\Pi}^n + \Delta\bar{\Pi}^{n+1} \quad \text{in } \Omega + \partial\Omega \quad (\text{A.4c})$$

The divergence free velocity is finally obtained as

$$\bar{\mathbf{u}}^{n+1} = \bar{\mathbf{u}}_*^{n+1} - \Delta t \nabla(\Delta\bar{\Pi}^{n+1}) \quad \text{in } \Omega + \partial\Omega \quad (\text{A.5})$$

## Appendix A: (Continued)

### A.1.2 Scalar Equation

Similar grouping as in Eqn. A.1 can be made for the scalar equation as follows

$$H_c(\bar{C}) = \frac{1}{La_t^2} \phi_j^s \frac{\partial \bar{C}}{\partial x_j} - \frac{1}{ReSc} \frac{\partial^2 \bar{C}}{\partial x_j^2} - \frac{\partial q_j^{res}}{\partial x_j} \quad (\text{A.6})$$

Explicitly discretizing the terms in Eqn. A.6 using the second-order time accurate A-B scheme leads to

$$N_c(\bar{C}^n, \bar{C}^{n-1}) = \frac{3}{2}H_c(\bar{C}^n) - \frac{1}{2}H_c(\bar{C}^{n-1}) \quad (\text{A.7})$$

where again the superscripts refer to time steps  $n$  and  $n-1$ . We can re-express scalar equation using second-order time accurate C-N scheme to discretize the viscous term together with the previous A-B scheme as

$$\left( \frac{1}{\Delta t} + \frac{1}{2ReSc} \nabla^2 \right) \Delta \bar{C}^{n+1} = -N_c(\bar{C}^n, \bar{C}^{n-1}) + \frac{1}{ReSc} \nabla^2 \bar{C}^n \quad \text{in } \Omega \quad (\text{A.8a})$$

$$\bar{C}^{n+1} = \bar{C}^n + \Delta \bar{C}^{n+1} \quad \text{in } \Omega + \partial\Omega \quad (\text{A.8b})$$

## A.2 Spatial Discretization

The spatial discretization is hybrid, as it makes use of fast Fourier transforms in the horizontal direction ( $x_1$  and  $x_2$ ) and high-order finite differences in the vertical direction ( $x_3$ ).

Taking the two-dimensional Fourier transform of the temporally discrete momentum equa-

## Appendix A: (Continued)

tion in Equation A.3 and concentration equation in Equation A.8 and denoting a Fourier transformed quantity with an over-hat,  $\widehat{\cdot}$ , leads to

$$\left( \frac{1}{\Delta t} + \frac{1}{2Re} |\mathbf{k}_h|^2 - \frac{1}{2Re} \frac{\delta^2}{\delta x_3^2} \right) \widehat{\Delta \bar{\mathbf{u}}_*}^{n+1} = -\widehat{N}(\bar{\mathbf{u}}^n, \bar{\mathbf{u}}^{n-1}) - \nabla_s \widehat{p}^n + \frac{1}{Re} \left\{ -|\mathbf{k}_h|^2 + \frac{\delta^2}{\delta x_3^2} \right\} \widehat{\bar{\mathbf{u}}}^n \quad \text{in } \Omega \quad (\text{A.9a})$$

$$(\widehat{u}_{1*}^{n+1}, \widehat{u}_{2*}^{n+1}) = (0, 0) \quad \text{on } \partial\Omega_1 \quad (\text{A.9b})$$

$$\left( \frac{\delta \widehat{u}_{1*}^{n+1}}{\delta x_3}, \frac{\delta \widehat{u}_{2*}^{n+1}}{\delta x_3} \right) = (Re, 0) \quad \text{on } \partial\Omega_2 \quad (\text{A.9c})$$

$$\widehat{\bar{\mathbf{u}}_*}^{n+1} = \widehat{\bar{\mathbf{u}}}^n + \widehat{\Delta \bar{\mathbf{u}}_*}^{n+1} \quad \text{in } \Omega \quad (\text{A.9d})$$

$$\left( \frac{1}{\Delta t} + \frac{1}{2ReSc} |\mathbf{k}_h|^2 - \frac{1}{2ReSc} \frac{\delta^2}{\delta x_3^2} \right) \widehat{\Delta \bar{C}}_*^{n+1} = -\widehat{N}(\bar{C}^n, \bar{C}^{n-1}) + \frac{1}{ReSc} \left\{ -|\mathbf{k}_h|^2 - \frac{\delta^2}{\delta x_3^2} \right\} \widehat{\bar{C}}^n \quad \text{in } \Omega \quad (\text{A.10a})$$

$$\widehat{\bar{C}}^{n+1} = -1/2 \quad \text{on } \partial\Omega_1 \quad (\text{A.10b})$$

$$\widehat{\bar{C}}^{n+1} = 1/2 \quad \text{on } \partial\Omega_2 \quad (\text{A.10c})$$

$$\widehat{\bar{C}}^{n+1} = \widehat{\bar{C}}^n + \widehat{\Delta \bar{C}}_*^{n+1} \quad \text{in } \Omega \quad (\text{A.10d})$$

where  $\mathbf{k}_h = k_1 \mathbf{e}_1 + k_2 \mathbf{e}_2$  and  $k_1$  (resp.  $\mathbf{e}_1$ ) and  $k_2$  (resp.  $\mathbf{e}_2$ ) are the wavenumbers (resp. unit vectors) in the  $x_1$  and  $x_2$  directions. Operators  $\delta/\delta x_3$  and  $\delta^2/\delta x_3^2$  denote the finite-difference approximations of  $\partial/\partial x_3$  and  $\partial^2/\partial x_3^2$  and  $\nabla_s = (ik_1, ik_2, \delta/\delta x_3)$ . The interested reader is directed to [86] for the finite-difference approximations used. Taking the two-

## Appendix A: (Continued)

dimensional Fourier transport of the Poisson equation in Equation A.4c leads to

$$\left(-|\mathbf{k}_h|^2 + \frac{\delta^2}{\delta x_3^2}\right) \widehat{\Delta \bar{p}}^{n+1} = \frac{1}{\Delta t} \left( ik_1 \widehat{u}_{1*}^{n+1} + ik_2 \widehat{u}_{2*}^{n+1} + \frac{\delta}{\delta x_3} \widehat{u}_{3*}^{n+1} \right) \quad \text{in } \Omega + \partial\Omega \quad (\text{A.11a})$$

$$\frac{\delta \widehat{\Delta \bar{\Pi}}^{n+1}}{\delta x_3} = \frac{1}{\Delta t} \widehat{u}_{3*}^{n+1} \quad \text{on } \partial\Omega \quad (\text{A.11b})$$

$$\widehat{\bar{\Pi}}^{n+1} = \widehat{\bar{p}}^n + \widehat{\Delta \bar{p}}^{n+1} \quad \text{in } \Omega + \partial\Omega \quad (\text{A.11c})$$

The velocity at time step  $n+1$  becomes

$$\widehat{u}_1^{n+1} = \widehat{u}_{1*}^{n+1} - i\Delta t k_1 \widehat{\bar{\Pi}}^{n+1} \quad \text{in } \Omega + \partial\Omega \quad (\text{A.12a})$$

$$\widehat{u}_2^{n+1} = \widehat{u}_{2*}^{n+1} - i\Delta t k_2 \widehat{\bar{\Pi}}^{n+1} \quad \text{in } \Omega + \partial\Omega \quad (\text{A.12b})$$

$$\widehat{u}_3^{n+1} = \widehat{u}_{3*}^{n+1} - \Delta t \frac{\delta}{\delta x_3} \widehat{\bar{\Pi}}^{n+1} \quad \text{in } \Omega + \partial\Omega \quad (\text{A.12c})$$

At the end of the time step, after the final velocity is computed via Equation A.12,  $\widehat{u}_3^{n+1}$  is set to zero on  $\partial\Omega$  (the bottom and top boundaries). This is also done for  $\widehat{u}_1^{n+1}$  and  $\widehat{u}_2^{n+1}$  on  $\partial\Omega_1$  (the bottom boundary).

### A.3 Grid Stretching

Our simulations need to resolve the strong gradients in the  $x_3$  direction near the bottom boundary and the top surface. To achieve this, a large number of points are assembled near these two regions. This is accomplished via stretching is done following [86] and [87].

## Appendix A: (Continued)

Consider a set of equidistant points at locations  $\xi_i$  discretizing the vertical direction ( $x_3$ ). Then, clustering or stretching of these points may be accomplished through a mapping hyperbolic function (with existing real inverse) such as

$$z_i = (1/b)\tanh [\xi_i \tanh^{-1}(b)] \quad (\text{A.13})$$

This function takes the set of  $N$  equispaced points  $\xi_i$  discretizing the interval  $[-1, 1]$  and maps them to the set of  $N$  non-uniformly spaced points  $z_i$  in  $[-1, 1]$ . The points  $z_i$  are clustered near the upper and lower bounds of the interval. Coefficient  $b$  is a measure of the clustering.

The finite-difference approximations of  $\partial/\partial x_3$  and  $\partial^2/\partial x_3^2$  used here can be applied only over points which are equidistant. Thus, derivatives on the non-uniform grid are computed in terms of derivatives on the equidistant grid and derivatives of the inverse of the mapping function as

$$\frac{df}{dz} = \frac{df}{d\xi} \frac{d\xi}{dz}, \quad \frac{d^2f}{dz^2} = \frac{d^2f}{d\xi^2} \left( \frac{d\xi}{dz} \right)^2 + \frac{df}{d\xi} \frac{d^2\xi}{dz^2} \quad (\text{A.14})$$

where  $z$  and  $\xi$  denote  $z_i$  and  $\xi_i$ , respectively, in Eqn. A.13. Note that this approach to clustering leads to non-uniformly spaced grid points in the vertical direction only. The grid points are uniformly spaced in the horizontal directions.

## Appendix A: (Continued)

### A.4 Accuracy of the Numerical Method

For all simulations performed, conservation of momentum and conservation of mass (continuity) equations were satisfied up to  $O(\Delta t^2)$  at every time step, consistent with theoretical analysis described further below. Time step size satisfied a stability (CFL) condition obtained from von Neumann analysis. Stability of the method used has been considered by Slinn and Riley (1998) [78]. The stability limits of the combined time and space differencing schemes may be analyzed by performing a von Neumann stability analysis of the linearized system of governing equations. This analysis results in limits on the maximum time step for the numerical simulation.

Furthermore, internal consistency checks were made for all simulations (see Appendix B) ensuring that statistics presented satisfied the Reynolds-averaged (ensemble-averaged) LES equations.

In this dissertation all the simulations were performed on a  $32 \times 64 \times 97$  grid. Tejada-Martínez and Grosch (2007) [86] presented results in flows with Langmuir circulation with different grid resolutions including the  $32 \times 64 \times 97$  grid used and a finer grid and found no significant differences between the turbulence structure resolved and turbulence statistics. Thus we have performed all of the simulations described in the thesis on the  $32 \times 64 \times 97$  grid.

Spatial discretization of the method involves Fast Fourier Transforms (FFT) in two directions and high order (5th and 6th) order accurate compact finite difference stencils in the third direction. Truncation errors for the finite difference schemes based on Taylor series

## Appendix A: (Continued)

analysis are given by Lele (1992) [51] and Carpenter et al. (1993) [12]. The spatial discretization (including the finite difference stencils) is described in detail in the referenced literature (Tejada-Martínez and Grosch, 2007 [86] and Tejada-Martínez et al., 2009 [87]).

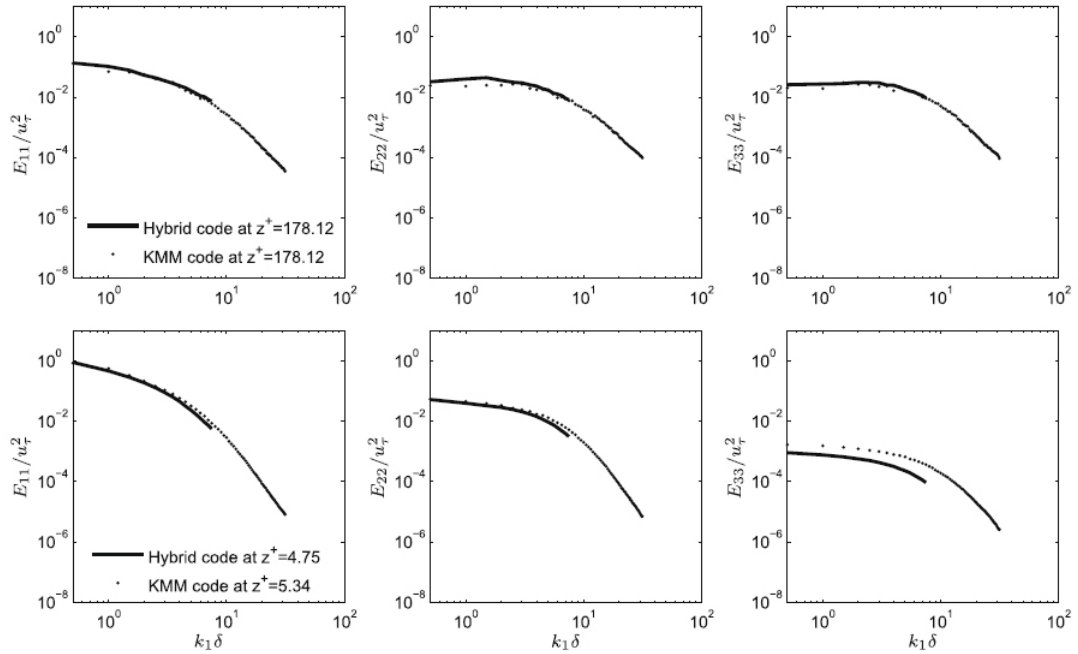


Figure A.1: Downwind 1D energy spectra in LES of turbulent channel flow. [87] Reprinted with permission from Ocean Modeling, 30, A.E. Tejada-Martínez, C.E. Grosch, A.E. Gargett, J.A Polton, J.A. Smith, and J.A. MacKinnon. A hybrid spectral/finite-difference large-eddy simulator of turbulent processes in the upper ocean, 115-142, 2009. Copyright (2009), with permission from Elsevier.

High order spatial methods were chosen because of their ability to capture all of the turbulent scales accurately. This can be observed in terms of energy spectra. Energy spectra measure energy as a function of wavenumber, where wavenumber is inversely proportional to the spatial scales of the turbulence. Thus, the energy at large wavenumbers corresponds to the energy contained by small scales and vice-versa. High order spatial methods have been shown to accurately capture energy spectra in a turbulent flow down to the smallest

## **Appendix A: (Continued)**

scale resolved by the grid (see Fig. A.1). In Fig. A.1, dotted curves correspond to energy spectra in direct numerical simulation (DNS) of Kim et al. (1987) [45]. Solid curves correspond to energy spectra in LES with the method used in the present dissertation. Note that the DNS resolves down to the smallest scales of the turbulence. The LES resolves down to the largest scales due to a coarser grid.

Lower order methods resolve the energy in the largest scales accurately but underestimate the energy in the smaller scales (see Fig. A.2). Note that, in Fig. A.2, open circles correspond to energy spectra in direct numerical simulation (DNS) of Kim et al. (1987) [45]. Other curves correspond to energy spectra in simulations performed with low order methods employed by Najjar and Tafti [61]. Cases 9, 10 and 11 correspond to LES on the same grid as the high order LES in Fig. A.1.

The temporal discretization in the numerical method employed consists of the explicit, second order Adams-Bashforth scheme for nonlinear terms and the implicit, second order Crank-Nicholson scheme for linear viscous terms and a second order fractional step scheme for sequential solution of momentum equations and a Poisson equation for pressure. More specifically, the fractional step algorithm consists of the pressure correction method on a non-staggered grid (see [1]). The non-staggered grid is attractive as it avoids interpolations from grid points to cell centers and vice versa, while achieving second-order accuracy for momentum and continuity. Fractional-step algorithms require solution of the momentum equation leading to an intermediate, non-solenoidal velocity followed by a Poisson equation for pressure leading to a velocity correction enforcing continuity. Details of the fractional step scheme were shown in Section A.2. Armfield and Street (2000) [1] and



## Appendix A: (Continued)

Tejada-Martínez et al. (2009) [87] showed that this method results in 2nd order accuracy in momentum and continuity for various flow examples. Fringer et al. (2003) [25] performed theoretical analysis showing that the fractional step scheme is 2nd order.

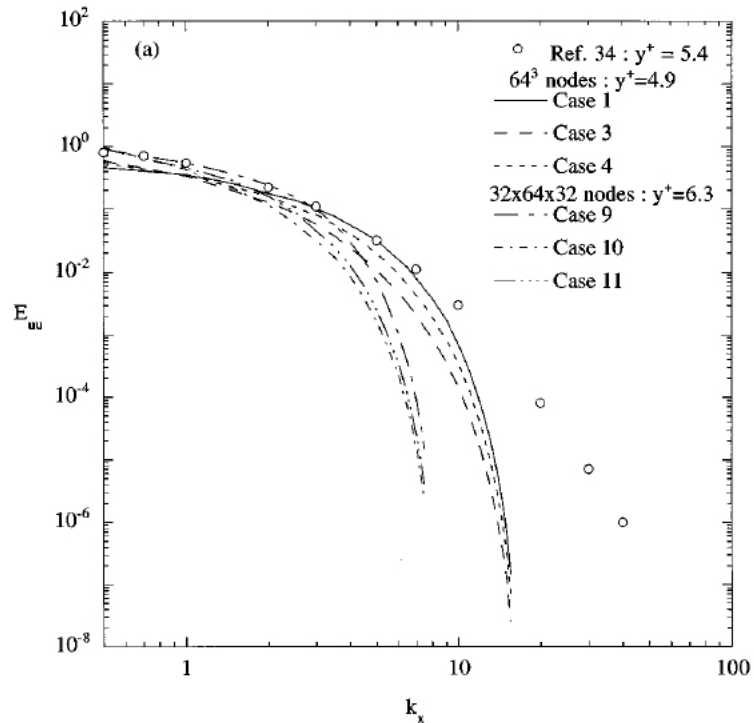


Figure A.2: Downwind 1D energy spectra in LES of a turbulent channel flow close to channel walls. [61] Reprinted with permission from F.M. Najjar and D.K. Tafti, Study of discrete test filters and finite difference approximations for the dynamic subgrid-scale stress model. *Phys. Fluids*, 8(4):1076-1088, 1996. Copyright 1996, American Institute of Physics

Use of spectral methods in the horizontal directions limits us to certain number of grid points. However, the spectral method employed uses Fourier series which lead to higher accuracy compared to lower order methods. Thus, even though the number of grid points is constrained, higher accuracy is reached, as seen earlier in terms of energy spectra.

## **Appendix A: (Continued)**

If number of grids points is a prime number (not power of 2), it is still possible to perform FFT according to Rader (1968) [70]. Still, there is a restriction on number of grid points. The need to perform simulations with high order methods capable of accurately resolving the turbulence while at the same time resolving complex boundaries with unrestricted numbers of grid points has led to the development of the variational formulation of Hughes et al. (2005) [37] and Bazilevs et al. (2007) [6] using NURBS (non-uniform rational B-splines) as basis functions. Cubic and quadratic NURBS have been shown to be more accurate than linear finite elements for obtaining turbulence statistics such as root mean square of velocity in turbulent channel flow (see [6]). However, energy spectra analysis in the form of Figures 1 and 2 above has yet to be done for this recent method.

As described previously, treatment of nonlinear terms is explicit and solution of momentum and continuity equations is split following a fractional step scheme. This allows for a simple-to-code and computationally fast algorithm per time step compared to implicit treatment of nonlinear terms together and a monolithic (i.e. without the time-splitting fractional step scheme) solution of momentum and continuity. However, the disadvantage of the present approach is that it requires smaller time steps for stability compared to a monolithic, fully implicit approach.

## Appendix B: Momentum and Scalar Balances

Averaging of turbulent quantities is performed over sufficiently long time such that averaged momentum and averaged scalar transport equations are satisfied. Satisfaction of these equations demonstrates that LES solutions are accurate.

### B.1 Momentum Balance

For the momentum balance of pressure driven flow, we start with the non-dimensional  $x_1$  momentum equation:

$$\frac{\partial \bar{u}_1}{\partial t} + \frac{\partial \bar{u}_1 \bar{u}_j}{\partial x_j} = \frac{\partial \bar{\Pi}}{\partial x_i} + \frac{1}{Re_\tau} \frac{\partial \tau_{1j}^v}{\partial x_j} + \frac{\partial \tau_{1j}^{SGS}}{\partial x_j} + f_1 \delta_{11} \quad (\text{B.1})$$

where  $f_1$  is the body force per unit volume representing the pressure gradient.

Averaging in time and over  $x_1$  and  $x_2$  directions (crosswind and vertical directions) together with the Reynolds decomposition leads to

$$\frac{\partial}{\partial x_3} \langle \bar{u}'_1 \bar{u}'_3 \rangle - \frac{\partial \langle \bar{\Pi} \rangle}{\partial x_i} - \frac{1}{Re_\tau} \frac{\partial \langle \tau_{13}^v \rangle}{\partial x_3} - \frac{\partial \langle \tau_{13}^{SGS} \rangle}{\partial x_3} - f_1 = 0 \quad (\text{B.2})$$

Integrating with respect to  $x_3$  results in

$$\int \frac{\partial}{\partial x_3} \langle \bar{u}'_1 \bar{u}'_3 \rangle dx_3 - \int \frac{\partial \langle \bar{\Pi} \rangle}{\partial x_i} dx_3 - \frac{1}{Re_\tau} \int \frac{\partial \langle \tau_{13}^v \rangle}{\partial x_3} dx_3 - \int \frac{\partial \langle \tau_{13}^{SGS} \rangle}{\partial x_3} dx_3 - \int f_1 dx_3 = 0 \quad (\text{B.3})$$

$$\langle \bar{u}'_1 \bar{u}'_3 \rangle - \langle \bar{\Pi} \rangle - \frac{1}{Re_\tau} \langle \tau_{13}^v \rangle - \langle \tau_{13}^{SGS} \rangle - f_1 x_3 = c \quad (\text{B.4})$$

## Appendix B: (Continued)

where  $c$  is an integration constant.

$\langle \bar{u}_3 \rangle = 0$  and  $\langle \bar{p} \rangle = 0$  at  $x_3 = -\delta$ . Also,  $\langle \tau_{13}^{SGS} \rangle$  vanishes at the top and bottom wall. Thus

we get

$$c = -\frac{1}{Re_\tau} \langle \tau_{13}^v \rangle \Big|_{x_3=-\delta} - f_1(-\delta) \quad (\text{B.5})$$

Note that

$$\langle \tau_{13}^v \rangle \Big|_{x_3=-\delta} = \frac{\partial \langle u_1 \rangle}{\partial x_3} \Big|_{x_3=-\delta} + \frac{\partial \langle u_3 \rangle}{\partial x_1} \Big|_{x_3=-\delta} \quad (\text{B.6})$$

and

$$\frac{\partial \langle u_1 \rangle}{\partial x_3} \Big|_{x_3=-\delta} = 2Re_\tau f_1 \delta \quad (\text{B.7})$$

Thus,  $c$  becomes

$$c = -2f_1 \delta + f_1 \delta = -f_1 \delta \quad (\text{B.8})$$

Inserting  $c$  into Eqn. B.4 leads to

$$\begin{aligned} \langle \bar{u}'_1 \bar{u}'_3 \rangle - \frac{1}{Re_\tau} \langle \tau_{13}^v \rangle - \langle \tau_{13}^{SGS} \rangle - f_1 x_3 &= -f_1 \delta \\ \langle \bar{u}'_1 \bar{u}'_3 \rangle - \frac{1}{Re_\tau} \langle \tau_{13}^v \rangle - \langle \tau_{13}^{SGS} \rangle &= f_1 (x_3 - \delta) \end{aligned} \quad (\text{B.9})$$

Dividing both sides by  $f_1$  gives

$$\frac{1}{f_1} \langle \bar{u}'_1 \bar{u}'_3 \rangle - \frac{1}{f_1 Re_\tau} \langle \tau_{13}^v \rangle - \frac{1}{f_1} \langle \tau_{13}^{SGS} \rangle = (x_3 - \delta) \quad (\text{B.10})$$

Using the space and time-dependent numerical solution of the LES equations in Section

## Appendix B: (Continued)

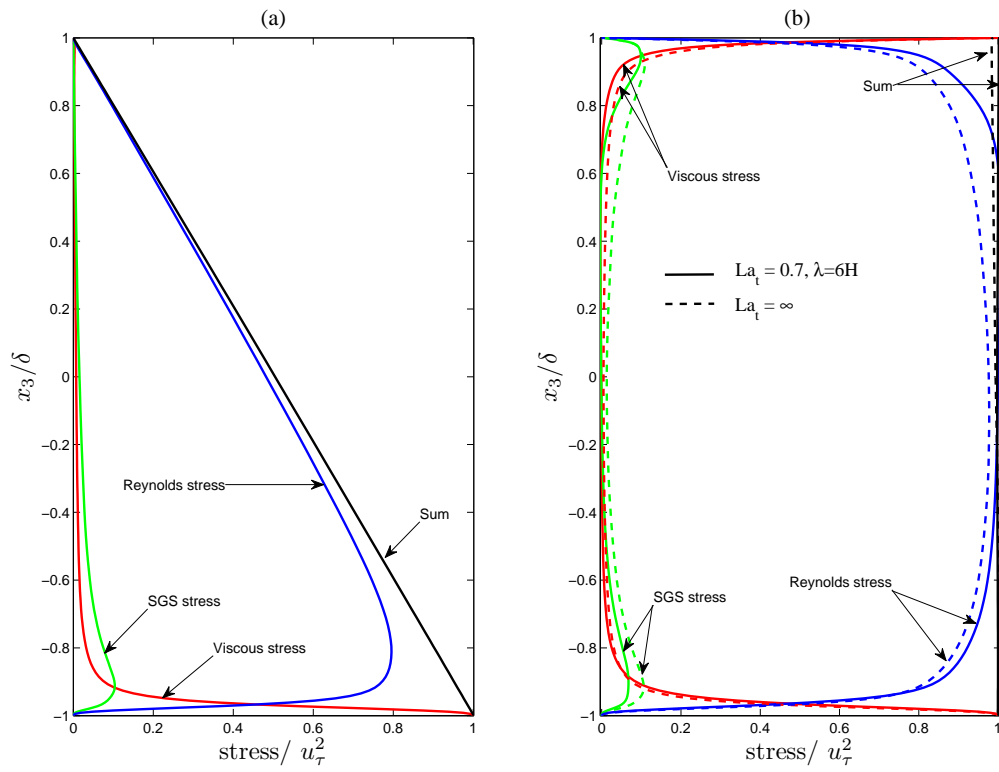


Figure B.1: Momentum balance for (a) pressure driven flow (b) wind driven flows with and without LC where  $\langle \bar{u}'_i \bar{u}'_3 \rangle$  is the Reynolds stress;  $\langle \tau_{13}^{SGS} \rangle$  is the SGS stress and is the  $\langle \tau_{13}^V \rangle$  is the viscous stress

## Appendix B: (Continued)

4.1.2, each of the terms in the right hand side of Eqn. B.10 were computed and plotted in Fig. B.1a for pressure-gradient driven flow. For a sufficiently long time average, the sum of these terms results in a straight line varying between 1 at the top of the domain and 0 at the bottom. This result is expected as dictated by Eqn. B.10. Also, we see that near the wall viscous stress dominates. This is because the no-slip boundary condition at the wall makes all Reynolds stresses go to zero at the wall. As we go far from the wall Reynolds stress and SGS stress become more important. Also, note that effect of SGS stress is very small compared to Reynolds stress. Thus, the LES is resolving the majority of the turbulence.

Similarly, for wind driven flow with and without LC we can write

$$\frac{\partial \bar{u}_1}{\partial t} + \frac{\partial \bar{u}_1 \bar{u}_j}{\partial x_j} = \frac{\partial \bar{p}}{\partial x_i} + \frac{1}{Re_\tau} \frac{\partial \tau_{1j}^v}{\partial x_j} + \frac{\partial \tau_{1j}^{SGS}}{\partial x_j} \quad (\text{B.11})$$

Note the absence of the body force as in this case the surface wind stress drives the flow. Averaging in time and over  $x_1$  and  $x_2$  directions (crosswind and vertical directions) together with the Reynolds decomposition leads to

$$0 = -\frac{\partial}{\partial x_3} \langle \bar{u}'_1 \bar{u}'_3 \rangle + \frac{\partial \langle \bar{p} \rangle}{\partial x_i} + \frac{1}{Re_\tau} \frac{\partial \langle \tau_{13}^v \rangle}{\partial x_3} + \frac{\partial \langle \tau_{13}^{SGS} \rangle}{\partial x_3} \quad (\text{B.12})$$

Integrating with respect to  $x_3$  leads to

$$c = -\langle \bar{u}'_1 \bar{u}'_3 \rangle + \langle \bar{p} \rangle + \frac{1}{Re_\tau} \langle \tau_{13}^v \rangle + \langle \tau_{13}^{SGS} \rangle \quad (\text{B.13})$$

where  $c$  is an integration constant.

## Appendix B: (Continued)

$\langle \bar{u}_3 \rangle = 0$  and  $\langle \bar{p} \rangle = 0$  at  $x_3 = -\delta$ , thus we get

$$c = \frac{1}{Re_\tau} \langle \tau_{13}^v \rangle_{x_3=-\delta} \quad (\text{B.14})$$

Dividing both sides by  $c$  we get:

$$1 = -\frac{\langle \bar{u}'_i \bar{u}'_3 \rangle}{c} + \frac{1}{Re_\tau} \frac{\langle \tau_{13}^v \rangle}{c} + \frac{\langle \tau_{13}^{SGS} \rangle}{c} \quad (\text{B.15})$$

Using the space and time-dependent numerical solution of the LES equations each of the terms in the right hand side of equation 4.12 were computed and plotted in Fig. B.1b for wind-driven flows with and without LC. For a sufficiently long time average, the sum of these terms is constant, as dictated by Eqn. B.15. Note that in the presence of LC, SGS stress is smaller but Reynolds stress is greater than the flow without LC. Moreover, we see that viscous effects dominates both wall and surface regions where in pressure driven case viscous effects go to zero as we approach the surface. Similar to pressure driven flow, Reynolds stress and SGS stress are also zero at the wall and at the surface.

## B.2 Scalar Balance

We start with the non-dimensional scalar equation:

$$\frac{\partial \bar{C}}{\partial t} + \frac{\partial \bar{C} \bar{u}_j}{\partial x_j} = \frac{1}{Re_\tau Sc} \frac{\partial^2 \bar{C}}{\partial x_j^2} + \frac{\partial q_j}{\partial x_j} \quad (\text{B.16})$$

## Appendix B: (Continued)

Averaging in time and over  $x_1$  and  $x_2$  directions (crosswind and vertical directions) together with the Reynolds decomposition leads to

$$0 = \frac{1}{Re_\tau Sc} \frac{\partial^2 \langle \bar{C} \rangle}{\partial x_3^2} + \frac{\partial \langle q_3 \rangle}{\partial x_3} - \frac{\partial \langle \bar{u}'_3 \bar{C}' \rangle}{\partial x_3} \quad (\text{B.17})$$

Integrating with respect to  $x_3$  leads to

$$\frac{1}{Re_\tau Sc} \frac{\partial \langle \bar{C} \rangle}{\partial x_3} + \langle q_3 \rangle - \langle \bar{u}'_3 \bar{C}' \rangle = c \quad (\text{B.18})$$

where  $c$  is an integration constant.

$\langle u_3 \rangle = 0$  at  $x_3 = -\delta$ , thus we get

$$c = \frac{1}{Re_\tau Sc} \frac{\partial \langle \bar{C} \rangle}{\partial x_3} \Big|_{x_3 = -\delta} \quad (\text{B.19})$$

Dividing both sides by  $c$  results in

$$\frac{1}{c} \frac{1}{Re_\tau Sc} \frac{\partial \langle \bar{C} \rangle}{\partial x_3} + \frac{\langle q_3 \rangle}{c} - \frac{\langle \bar{u}'_3 \bar{C}' \rangle}{c} = 1 \quad (\text{B.20})$$

The terms obtained from scalar equation for pressure gradient driven flow, wind driven flow with and without LC are shown in Fig. B.2. Similar to shear stresses obtained from momentum equation, SGS flux and vertical turbulent scalar flux are zero at the wall and at the surface where the vertical diffusive flux dominates.



Appendix B: (Continued)

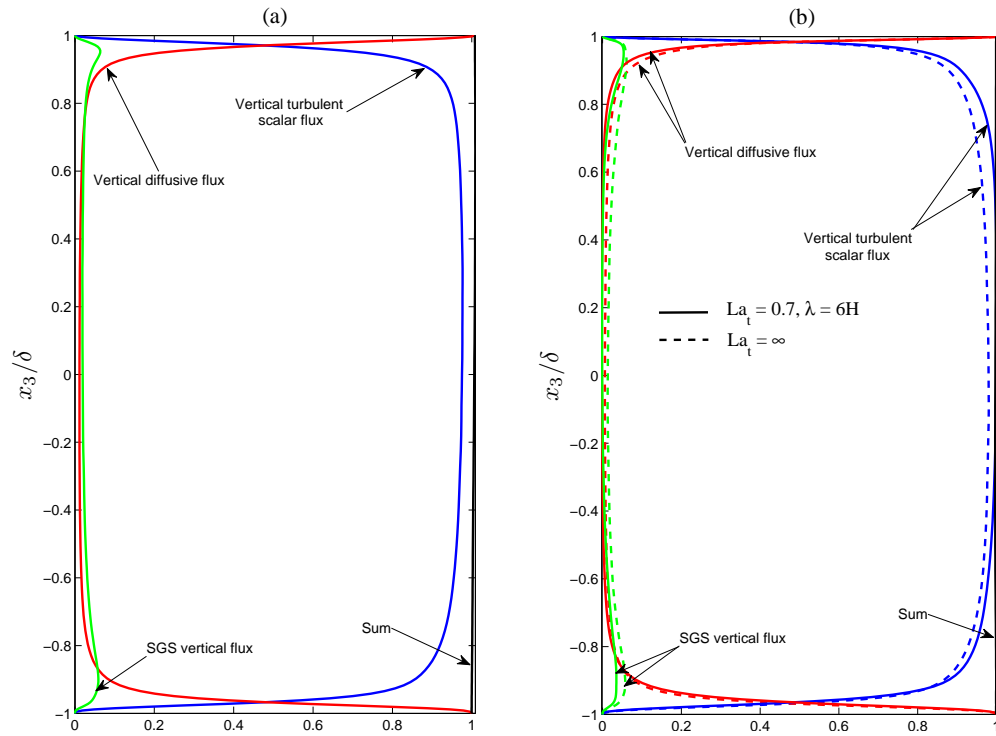


Figure B.2: Scalar balance for (a) pressure driven flow (b) wind driven flows with and without LC where  $\langle \bar{u}'_3 \bar{C}' \rangle$  is the Reynolds stress;  $\langle q_3 \rangle$  is the SGS stress and  $\frac{\partial \langle C \rangle}{\partial x_3}$  is the vertical diffusive flux

**Appendix B: (Continued)**

## Appendix C: Resolved Turbulent Kinetic Energy

Following the Reynolds decomposition,  $\bar{u}_i = \langle \bar{u}_i \rangle + \bar{u}'_i$ , the transport equation for mean resolved turbulent kinetic energy,  $\bar{q} \equiv \langle \bar{u}'_i \bar{u}'_i \rangle / 2$  can be expressed as

$$\frac{\partial \bar{q}}{\partial t} + \langle \bar{u}_k \rangle \frac{\partial \bar{q}}{\partial x_k} = P + L + T + T^{\text{SGS}} + D + A + \varepsilon + \varepsilon^{\text{SGS}} \quad (\text{C.1})$$

Definition of these terms are given in Table C.1.

Table C.1: Budgets of turbulent kinetic energy

P	=	$-\langle \bar{u}'_i \bar{u}'_j \rangle \frac{\partial \langle \bar{u}_i \rangle}{\partial x_j}$	mean shear production rate
L	=	$-\frac{1}{La_t^2} \langle \bar{u}'_i \bar{u}'_j \rangle \frac{\partial \phi_i^s}{\partial x_j}$	Stokes drift production rate
T	=	$-\frac{\partial}{\partial x_j} \langle \bar{q} \bar{u}'_j \rangle$	turbulent transport rate
$T^{\text{SGS}}$	=	$\frac{\partial}{\partial x_j} \langle \bar{u}'_i \tau_{ij}^{d'} \rangle$	SGS transport rate
D	=	$\frac{1}{\text{Re}} \frac{\partial^2 \bar{q}}{\partial x_j^2}$	viscous diffusion rate
A	=	$-\frac{\partial}{\partial x_j} \langle \bar{p}' \bar{u}'_j \rangle$	pressure transport rate
$\varepsilon$	=	$-\frac{1}{\text{Re}} \left\langle \frac{\partial \bar{u}'_i}{\partial x_j} \frac{\partial \bar{u}'_i}{\partial x_j} \right\rangle$	viscous dissipation rate
$\varepsilon^{\text{SGS}}$	=	$-\left\langle \tau_{ij}^{d'} \bar{S}'_{ij} \right\rangle$	SGS dissipation rate

## Appendix D: Budgets of $\langle \bar{C}^2 \rangle$

We now examine the budgets of resolved concentration variance  $\langle \bar{c}_f \rangle \equiv \frac{1}{2} \langle \bar{C}^2 \rangle$  which is depicted in Figs. D.1 and D.2. Following the Reynolds decomposition,  $\bar{C} = \langle \bar{C} \rangle + \bar{C}'$ , the transport equation for mean resolved concentration variance,  $\langle \bar{c}_f \rangle \equiv \frac{1}{2} \langle \bar{C}^2 \rangle$ , can be written as:

$$\frac{\partial \langle \bar{c}_f \rangle}{\partial t} = P + L + T + T^{\text{SGS}} + D + \varepsilon + \varepsilon^{\text{SGS}} \quad (\text{D.1})$$

Definition of these terms are given in Table D.1.

Table D.1: Budgets of  $\langle \bar{C}' \bar{C}' \rangle$

P	=	$-\langle \bar{C}' \bar{u}'_3 \rangle \frac{\partial \langle \bar{C} \rangle}{\partial x_3}$	production rate
L	=	$-\frac{1}{La_t^2} \phi_j^s \langle \bar{C}' \frac{\partial \bar{C}'}{\partial x_j} \rangle$	Stokes drift production rate
T	=	$-\frac{\partial}{\partial x_3} \langle \bar{c}_f \bar{u}'_3 \rangle$	turbulent transport rate
$T^{\text{SGS}}$	=	$\frac{\partial}{\partial x_3} \langle \bar{C}' q'_3 \rangle$	SGS transport rate
D	=	$\frac{1}{Sc Re} \frac{\partial^2 \bar{c}_f}{\partial x_3^2}$	viscous diffusion rate
$\varepsilon^{\text{SGS}}$	=	$-\langle q'_j \frac{\partial \bar{C}'}{\partial x_j} \rangle$	SGS dissipation rate

Near the free surface, the production (red line) and turbulent transport (black line) decreases to balance the viscous loss in all cases. In wind driven flows with LC, production and transport rates increase relative to pressure gradient-driven flow and wind driven flow

## Appendix D: (Continued)

without LC. Also, wind driven flow with LC with  $La_t = 0.4$  has the highest production and transport rates.

Note that neither the C-L vortex force nor the Stokes drift velocity appear explicitly in the equation. Relative to wind-driven flow without LC, the impact of LC on the budgets of  $\langle \bar{C}'\bar{C}' \rangle$  within the surface diffusive and buffer regions occurs through increases in molecular diffusion (green line), molecular dissipation (dark blue line) and production by vertical gradient of mean concentration (red line) (see Fig. D.1). Note that the contribution of subgrid-scale dissipation (black dashed line) is negligible here given the high grid resolution in this region as described earlier. In the near surface log-layer region of the wind-driven flow without LC, the production  $\langle \bar{C}'\bar{C}' \rangle$  by the gradient of mean concentration is primarily balanced by molecular and subgrid-scale dissipation (Fig. D.2). In flows with LC this log-layer balance is disrupted as vertical turbulent transport plays a significant role in this balance, reaching values comparable to molecular and subgrid-scale dissipation in the  $La_t = 0.7$ ,  $\lambda = 6H$  and  $La_t = 1$ ,  $\lambda = 6H$  cases. This disruption is consistent with the log-layer disruption described earlier in terms of mean velocity, TKE budgets and mean concentration.

Appendix D: (Continued)

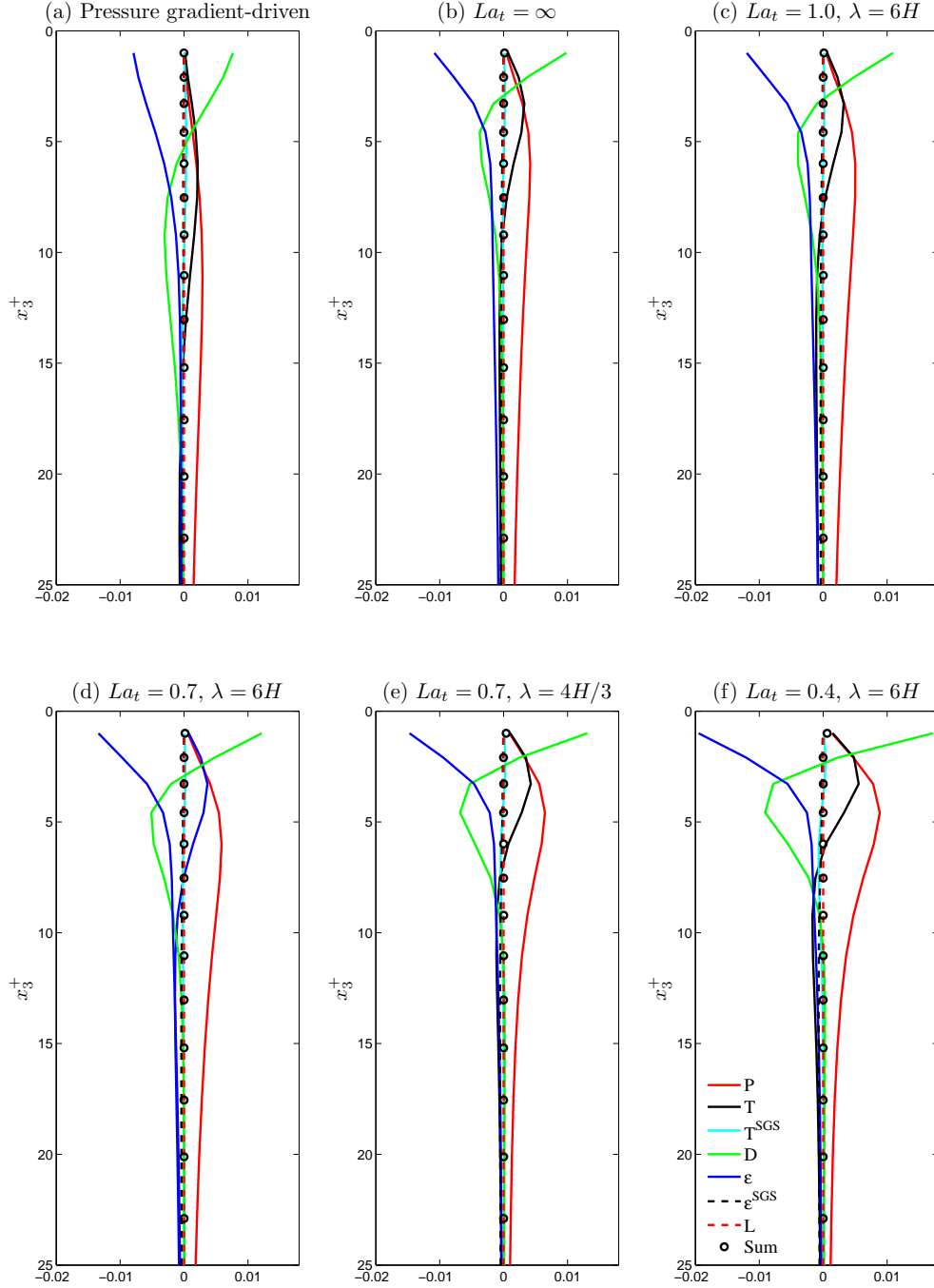


Figure D.1: Dimensionless budgets of  $\langle \bar{C}'\bar{C}' \rangle$  within surface diffusive and buffer regions.

## Appendix D: (Continued)

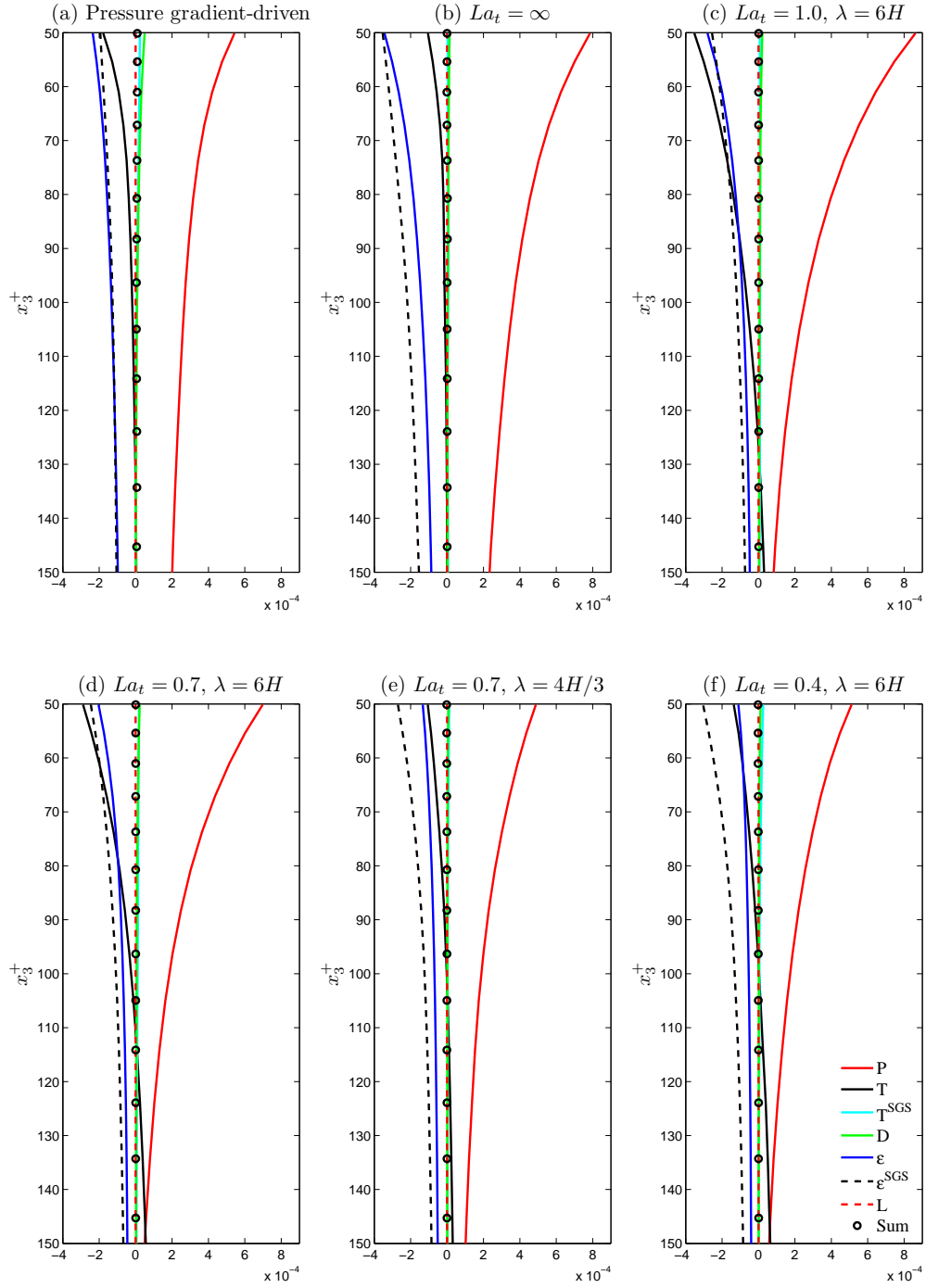


Figure D.2: Dimensionless budgets of  $\langle \bar{C}'\bar{C}' \rangle$  within surface log-layer.

## Appendix E: Budgets of $\langle \bar{C}' u'_3 \rangle$

Fig. E.1 shows budgets of  $-\langle \bar{C}' u'_3 \rangle$  within surface diffusive and buffer regions. Following the Reynolds decomposition,  $\bar{C} = \langle \bar{C} \rangle + \bar{C}'$ , the transport equation for  $-\langle \bar{C}' u'_3 \rangle$  can be written as:

$$-\frac{\partial \langle \bar{C}' u'_3 \rangle}{\partial t} = P^1 + P^2 + T + T^{\text{sgs1}} + T^{\text{sgs2}} + PC + D^1 + D^2 + \varepsilon + \varepsilon^{\text{sgs1}} + \varepsilon^{\text{sgs2}} + SP \quad (\text{E.1})$$

Definition of these terms are given in Table E.1.

Table E.1: Budgets of  $\langle \bar{C}' u'_3 \rangle$

$P^1$	$= \langle \bar{u}'_3 \bar{u}'_3 \rangle \frac{\partial \langle \bar{C} \rangle}{\partial x_3}$	production by mean concentration gradient
$P^2$	$= \langle \bar{C}' \bar{u}'_3 \rangle \frac{\partial \langle \bar{u}'_3 \rangle}{\partial x_3}$	production by mean velocity gradient
$T$	$= \frac{\partial}{\partial x_3} \langle \bar{C}' \bar{u}'_3 \bar{u}'_3 \rangle$	turbulent transport
$T^{\text{sgs1}}$	$= -\frac{\partial}{\partial x_3} \langle \bar{u}'_3 q'_3 \rangle$	transport of SGS scalar flux
$T^{\text{sgs2}}$	$= \frac{\partial}{\partial x_3} \langle \bar{C}' \tau'_{33} \rangle$	transport of SGS stresses
$PC$	$= \langle \bar{C}' \frac{\partial \bar{p}'}{\partial x_3} \rangle$	scalar pressure-gradient correlation
$D^1$	$= -\frac{1}{\text{Re}} \frac{\partial}{\partial x_3} \langle \bar{C}' \frac{\partial \bar{u}'_3}{\partial x_3} \rangle$	diffusion by velocity gradients
$D^2$	$= -\frac{1}{\text{Sc Re}} \frac{\partial}{\partial x_3} \langle \bar{u}'_3 \frac{\partial \bar{C}'}{\partial x_3} \rangle$	diffusion by concentration gradients



## Appendix E: (Continued)

Table E.1 (Continued)

$\varepsilon$	$= \left( \frac{1}{\text{Re}} + \frac{1}{\text{Sc Re}} \right) \left\langle \frac{\partial \bar{C}'}{\partial x_j} \frac{\partial \bar{u}'_3}{\partial x_j} \right\rangle$	viscous dissipation
$\varepsilon^{\text{SGS1}}$	$= \left\langle q'_j \frac{\partial \bar{u}'_3}{\partial x_j} \right\rangle$	dissipation by SGS scalar flux
$\varepsilon^{\text{SGS2}}$	$= \left\langle \tau'_{3j} \frac{\partial \bar{C}'}{\partial x_j} \right\rangle$	dissipation by SGS stresses
SP	$= \frac{1}{La_t^2} \left\langle \bar{C}' \bar{u}'_j \right\rangle \frac{\partial \phi_j^s}{\partial x_3}$	Stokes drift production rate

In the surface diffusive region budget terms in the pressure gradient-driven flow behave vastly different than in the wind-driven flows with and without LC. For example, in pressure gradient driven flow, scalar pressure-gradient correlation (black line) changes sign from sink to source as the surface is approached. Meanwhile, in all wind-driven flows, this term remains as a sink. At the surface in pressure gradient-driven flow, molecular dissipation (green line) and subgrid-scale (SGS) dissipation (black dashed line) are balanced by diffusion by velocity gradients (light blue line), diffusion by scalar concentration gradients (dark blue dashed line) and transport of SGS scalar flux (light blue dashed line). All wind-driven flows are characterized by a similar balance, except that the SGS dissipation and transport of SGS scalar flux are negligible.

The effect of parameter  $La_t$  on budgets of  $-\langle \bar{C}' u'_3 \rangle$  within the surface diffusive ( $x_3^+ < 5$ ) and buffer regions ( $5 < x_3^+ < 30$ ) in wind-driven flows with LC can be seen in Fig. E.1. Recall that this parameter is inversely proportional to wave forcing relative to wind forcing.

### Appendix E: (Continued)

As  $La_t$  drops to 0.4 from 0.7 while holding  $\lambda$  fixed, production by Stokes drift shear (dark blue line) becomes significant (Figs. E.1c,d). This trend is also seen with decreasing  $\lambda$  (the wavelength of surface waves) while holding  $La_t$  fixed, but not as pronounced as when varying  $La_t$ . For example, in the flow with  $La_t = 0.7$  and  $\lambda = 6H$ , production by Stokes drift shear is practically zero (Fig. E.1d) while in the flow with  $La_t = 0.7$  and  $\lambda = 4H/3$ , this term is noticeably larger.

Fig. E.2 shows budgets of  $-\langle \tilde{C}'u'_3 \rangle$  within the surface log-layer. In the case of wind driven flow without LC (Fig. E.2b) there is an almost perfect balance between production by mean scalar concentration gradient and concentration-pressure gradient correlation. This balance is disrupted in flows with LC in which production by mean scalar concentration gradient and production by Stokes drift shear are balanced by concentration-pressure gradient correlation and turbulent transport. Note that in the wind driven flows with LC, turbulent transport acts as a sink while in the pressure gradient-driven flow this term acts as a source.

## Appendix E: (Continued)

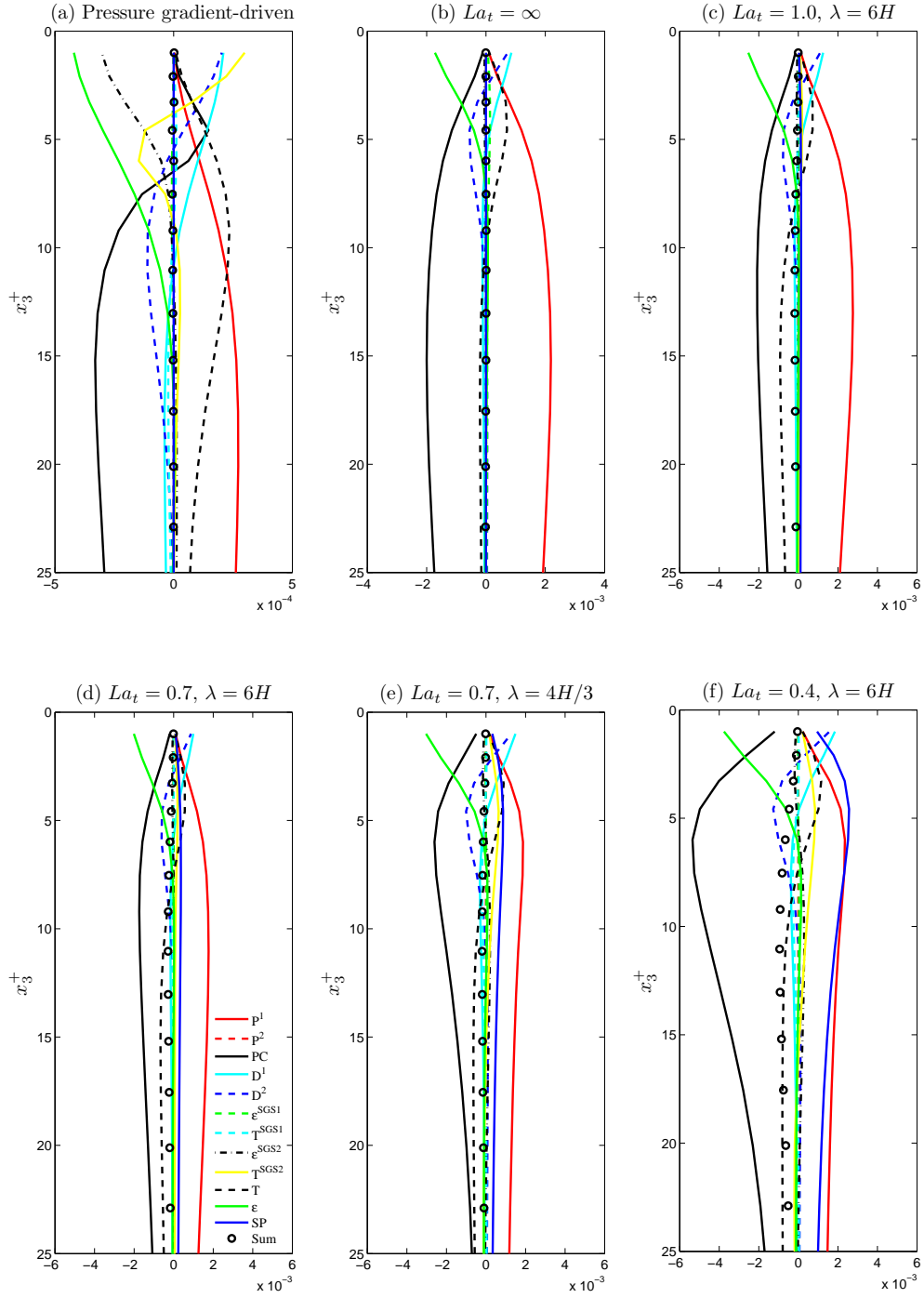


Figure E.1: Dimensionless budgets of  $\langle \bar{C}'\bar{u}'_3 \rangle$  within surface diffusive and buffer regions.

## Appendix E: (Continued)

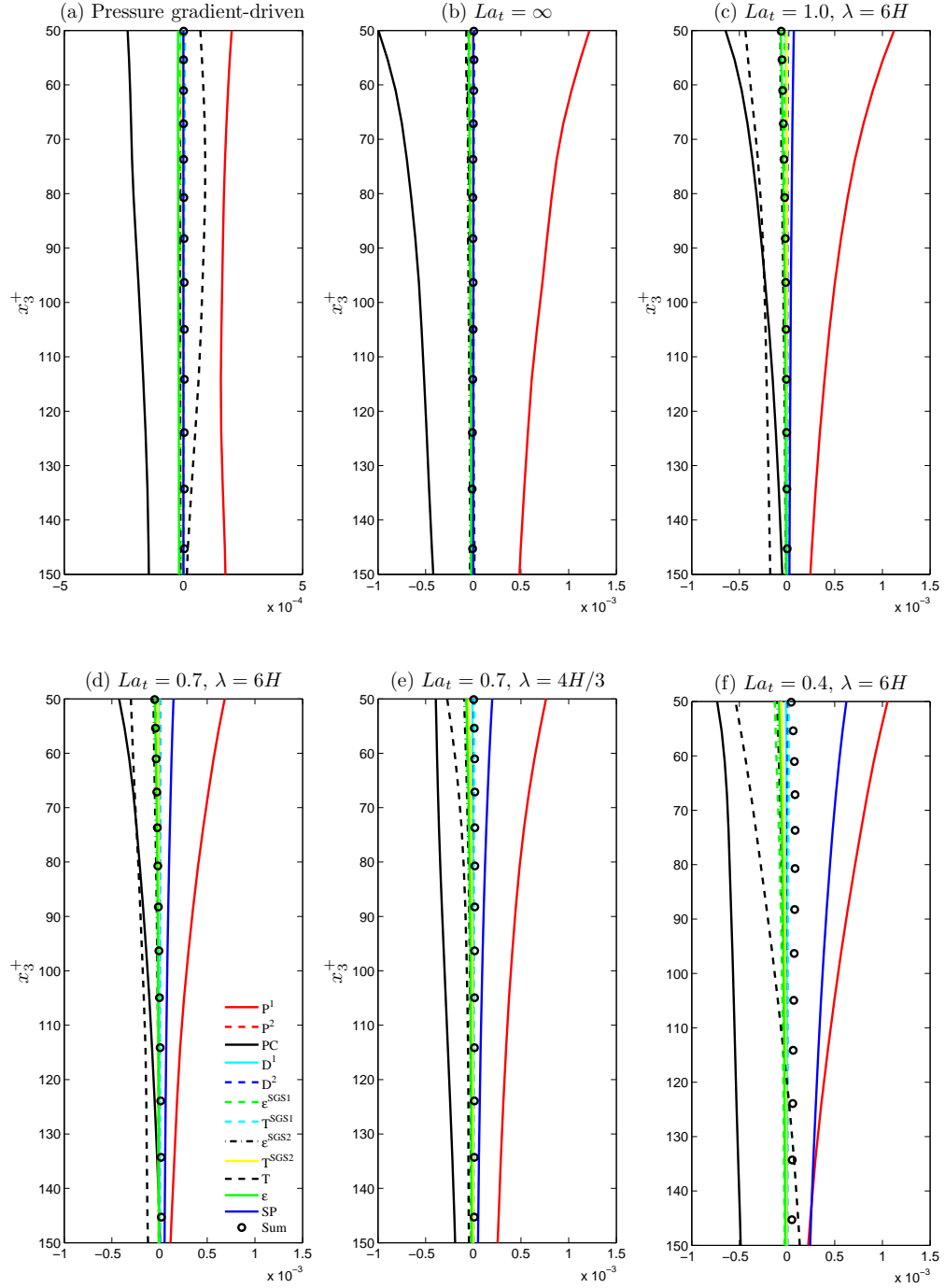


Figure E.2: Dimensionless budgets of  $\langle \bar{C}'\bar{u}'_3 \rangle$  within surface log-layer.

## Appendix F: Schmidt Number Dependence

We now examine the Schmidt number dependence of our LES results on transfer velocity. For this purpose, wind driven flows with and without LC at two different Schmidt numbers are simulated. As explained previously in Chapter 4, Schmidt number represents the ratio of momentum diffusivity (viscosity) to mass diffusivity. Mass transfer at very high Schmidt numbers is significant because of the concern on exchange of sparingly soluble gases through the air-water interface. For example, Schmidt number of  $\text{CO}_2$  in seawater is  $\approx 600$  [34].

Recall that transfer velocity is a measure of transfer velocity and it is given in dimensionless form as

$$K/u_\tau = \frac{1}{Re_t Sc \Delta C} \left( \frac{d\langle \bar{C} \rangle}{dx_3} \right)_{x_3=\delta} \quad (\text{F.1})$$

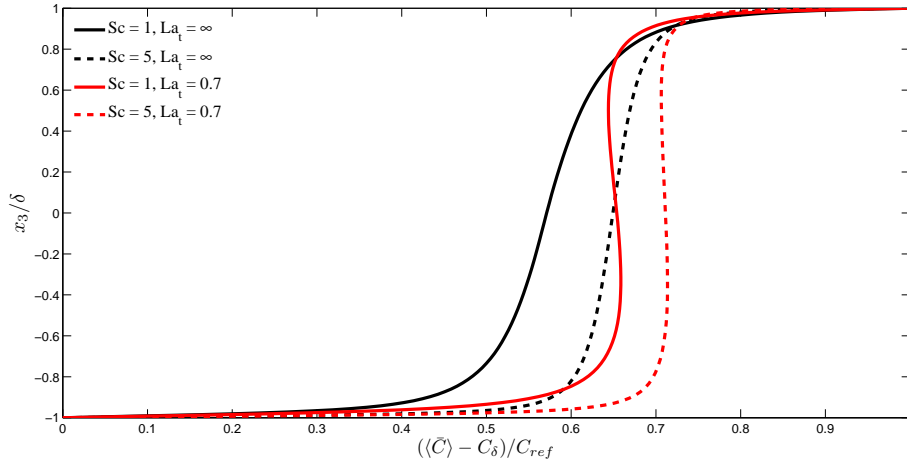


Figure F.1: Mean concentration in flows with and without LC at different Schmidt numbers.

In Fig. F.1, mean concentration profiles in flows with and without LC at different Schmidt numbers are shown. As the Schmidt number increases, the concentration boundary layer becomes thinner and mean scalar concentration increases. As a consequence,  $\Delta C$ , the

## Appendix F: (Continued)

difference in concentration between the surface and the bulk of the flow, decreases leading to an increase in transfer velocity (See Eqn. F.1).

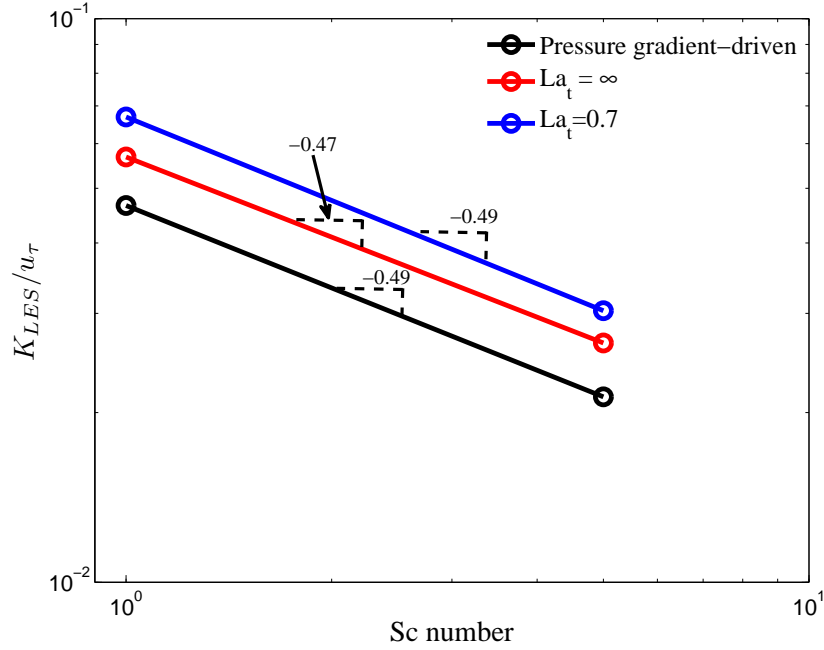


Figure F.2: Transfer velocity,  $K_{LES}/u_{\tau}$  at different  $Sc$  numbers.

Fig. F.2 shows the comparison of transfer velocity at different  $Sc$  numbers. It can be seen that LES of flows with and without LC follow a dependency close to  $Sc^m$  with  $m \approx -0.5$ . This is very close to the theoretical law  $K/u_{\tau} \approx Sc^{-1/2}$ . Thus, LC does not alter this classical result.

Recall that the number of grid points required to capture the smallest scales grows with  $Re_t$  and  $Sc$  like  $Sc^3 Re_t^{9/4}$  [10]. Thus, the LES performed is limited to low  $Sc$  and  $Re_t$  numbers in order to make computations feasible. The fact that heat ( $Pr = 7$ ) may be used as a tracer proxy for a scalar with a high value of  $Sc$  (e.g.  $CO_2$  with  $Sc = 660$ ) in order to measure the  $K$  of the latter (see 1.1 in Chapter 1 and related text) suggests

## **Appendix F: (Continued)**

that the turbulence has similar impact on the  $K$  for a low- $Sc$  scalar as it does on the  $K$  for a high- $Sc$  scalar. In other words, this suggests that the impact of the turbulence on  $K$  is universal across a wide range of  $Sc$  values. This might suggest that the Langmuir turbulence dependencies found at low  $Sc$  should also be valid at high  $Sc$ . Nevertheless, this should be confirmed in the future via simulations or lab/field measurements.

## Appendix G: Reynolds Number Dependence

In this Appendix, results from wind driven flows with and without LC at Reynolds numbers are presented in order to analyze the impact of Reynolds number on transfer velocity.

Fig. G.1 shows the mean concentration profiles in flows with and without LC at different Reynolds numbers. There is not a significant difference between the wind driven cases with LC in terms of mean concentration profiles whereas the difference is more pronounced in wind driven flows without LC.

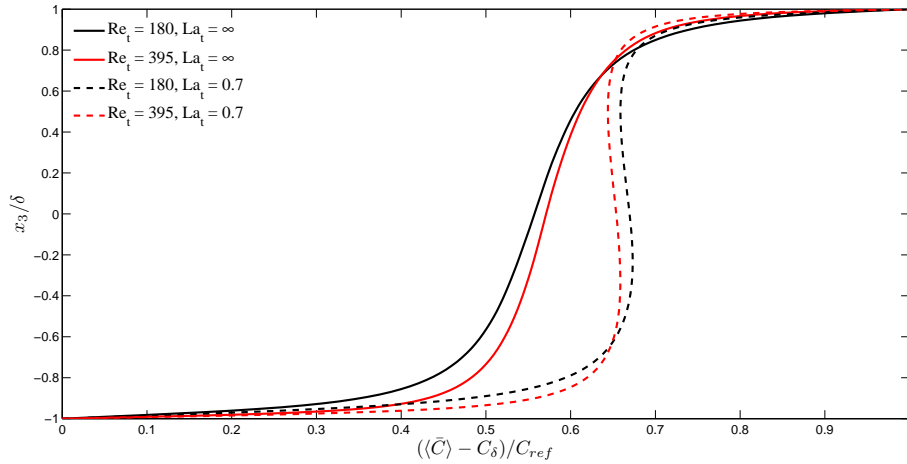


Figure G.1: Mean concentration in flows with and without LC at different Reynolds numbers.

According to LES results, transfer velocity,  $K$ , is  $\approx 68\%$  higher in wind driven flow with LC (with  $La_t = 0.7$ ,  $\lambda = 6H$ ) than in wind driven flow without LC for  $Re_\tau = 180$  whereas this increase is  $\approx 46\%$  for  $Re_\tau = 395$ . The comparison of the results are summarized in Table G.1.

Further investigation was made by performing another simulation at a higher Reynolds number ( $Re_\tau = 590$ ). Based on all the simulations, we found that for wind-driven flow without LC,  $K/u_\tau \sim Re_\tau^{-0.11}$  and for wind-driven flows with LC ( $\lambda = 6H$ ,  $La_t = 0.7$ )



## Appendix G: (Continued)

Table G.1: Comparison of  $K_{LES}$ ,  $C_{\text{bulk}}$ ,  $\Delta C$  and vertical gradient of concentration at the surface for in flows with and without LC at different Reynolds numbers scaled by  $C_{\text{ref}}$ .

Case	$K_{LES}/u_\tau$	$\frac{C_{\text{bulk}}}{C_{\text{ref}}}$	$\frac{\Delta C}{C_{\text{ref}}}$	$\frac{\delta}{C_{\text{ref}}} \left( \frac{\partial \langle \bar{C} \rangle}{\partial x_3} \right)_{x_3=\delta}$
$La_t = \infty, Re_t = 180$	0.070	0.557	0.443	5.588
$La_t = \infty, Re_t = 395$	0.066	0.571	0.429	11.224
$La_t = 0.7, Re_t = 180$	0.118	0.670	0.330	7.039
$La_t = 0.7, Re_t = 395$	0.097	0.654	0.346	13.219

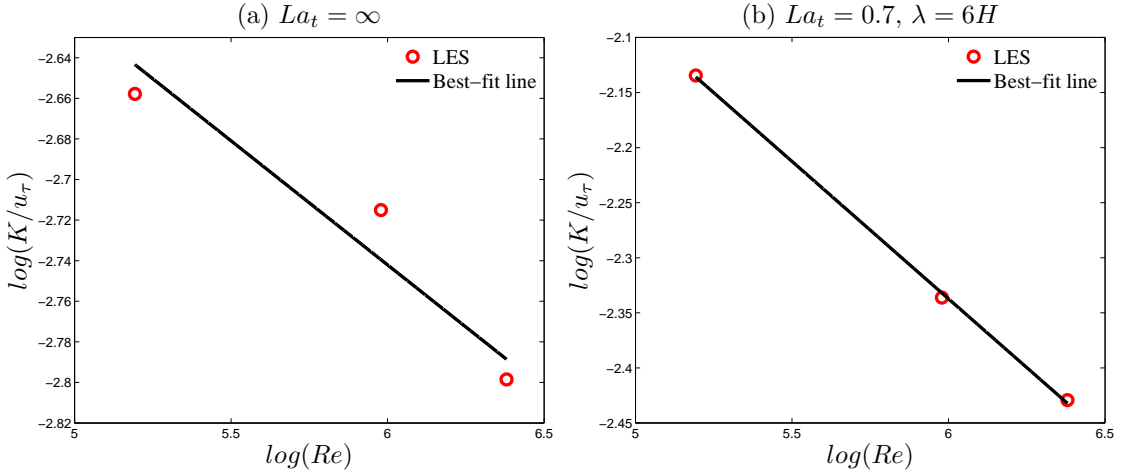


Figure G.2: Comparison transfer velocity ( $K$ ) at different Reynolds numbers in flows with ( $La_t = 0.7, \lambda = 6H$ ) and without LC.

$K/u_\tau \sim Re_\tau^{-0.25}$  (see Figs. G.2a and G.2b). These dependencies on  $Re_\tau$  are only based on three different Reynolds numbers, and additional measurements would have to be made to confirm these trends at higher Reynolds numbers. Measurements would have to come from laboratory or field experiments in order to reach significantly higher Reynolds numbers as computations would not be feasible.

Recall from Chapter 6 that Sherwood number is given as  $Sh = St Re_\tau Sc$ , where  $St = K/u_\tau$ . Our results imply that  $Sh$  scales as  $Re_\tau^{0.89}$  and  $Re_\tau^{0.75}$  for flows without LC and with LC ( $\lambda = 6H, La_t = 0.7$ ), respectively.

## Appendix G: (Continued)

An experimental study characterized by full-depth turbulent structures is the air-water gas transfer experiment of Gulliver and Halverson [31] performed in an open channel. Here the flow was driven by a moving bottom-bed and the surface was characterized by zero shear stress, unlike our wind-driven flows. Note though that this experimental flow is characterized by full-depth streamwise cells similar to LC but much weaker in intensity. For this laboratory setup, Gulliver and Halverson tracked  $K$  as a function of  $Re$  and found that  $K/u_\tau \sim Re^{-1/4}$ .

Recall that the turbulent Langmuir number,  $La_t$  is proportional to wind forcing relative to wave forcing. Present LES has been performed at the same values of  $La_t$  as observed in the field. Thus, although at the high  $Re$  numbers of the field conditions the wind forcing is much stronger than in the simulations, so is the wave forcing. In other words, since the wave forcing relative to wind forcing has been chosen to be the same in the simulations as it is in the field, it is expected that Langmuir circulation alters the turbulence structure and molecular boundary layer dynamics at high  $Re_\tau$  to the same extent that it does at low  $Re_\tau$ . Initial evidence of this is given by Tejada-Martínez et al. (2009) [87] having shown that the intensity of the full-depth LC structure resolved in simulations at low  $Re$  scales up to the intensity of the full-depth LC measured in the field by Gargett et al. (2004) [28] and Gargett and Wells (2007) [27] at much higher  $Re_\tau$ .

## Appendix H: Rights and Permissions

### H.1 Permissions to Use the Figures in Chapter 1

#### H.1.1 Permission to Use Figure 1.2

RightsLink - Your Account

<https://s100.copyright.com/MyAccount/viewPrintableLic...>

### ELSEVIER LICENSE TERMS AND CONDITIONS

Jun 22, 2012

This is a License Agreement between Cigdem Akan ("You") and Elsevier ("Elsevier") provided by Copyright Clearance Center ("CCC"). The license consists of your order details, the terms and conditions provided by Elsevier, and the payment terms and conditions.

**All payments must be made in full to CCC. For payment instructions, please see information listed at the bottom of this form.**

Supplier	Elsevier Limited The Boulevard, Langford Lane Kidlington, Oxford, OX5 1GB, UK
Registered Company Number	1982084
Customer name	Cigdem Akan
Customer address	717 SW 4th Street #2 Corvallis, OR 97333
License number	2934280277701
License date	Jun 22, 2012
Licensed content publisher	Elsevier
Licensed content publication	Deep Sea Research Part II: Topical Studies in Oceanography
Licensed content title	Climatological mean and decadal change in surface ocean pCO <sub>2</sub> , and net sea-air CO <sub>2</sub> flux over the global oceans
Licensed content author	Taro Takahashi, Stewart C. Sutherland, Rik Wanninkhof, Colm Sweeney, Richard A. Feely, David W. Chipman, Burke Hales, Gernot Friederich, Francisco Chavez, Christopher Sabine, Andrew Watson, Dorothee C.E. Bakker, Ute Schuster, Nicolas Metz, et al.
Licensed content date	April 2009
Licensed content volume number	56
Licensed content issue number	8-10
Number of pages	24
Start Page	554
End Page	577
Type of Use	reuse in a thesis/dissertation
Portion	figures/tables/illustrations
Number of figures/tables/illustrations	1
Format	electronic
Are you the author of this Elsevier article?	No
Will you be translating?	No
Order reference number	None
Title of your thesis/dissertation	Surface Mass Transfer in Large Eddy Simulation (LES) of Langmuir Turbulence
Expected completion date	Aug 2012

## Appendix H: (Continued)

RightsLink - Your Account

<https://s100.copyright.com/MyAccount/viewPrintableLic...>

Estimated size (number of pages)	145
Elsevier VAT number	GB 494 6272 12
Permissions price	0.00 USD
VAT/Local Sales Tax	0.0 USD / 0.0 GBP
<b>Total</b>	<b>0.00 USD</b>
<a href="#">Terms and Conditions</a>	

### INTRODUCTION

1. The publisher for this copyrighted material is Elsevier. By clicking "accept" in connection with completing this licensing transaction, you agree that the following terms and conditions apply to this transaction (along with the Billing and Payment terms and conditions established by Copyright Clearance Center, Inc. ("CCC"), at the time that you opened your Rightslink account and that are available at any time at <http://myaccount.copyright.com>).

### GENERAL TERMS

2. Elsevier hereby grants you permission to reproduce the aforementioned material subject to the terms and conditions indicated.

3. Acknowledgement: If any part of the material to be used (for example, figures) has appeared in our publication with credit or acknowledgement to another source, permission must also be sought from that source. If such permission is not obtained then that material may not be included in your publication/copies. Suitable acknowledgement to the source must be made, either as a footnote or in a reference list at the end of your publication, as follows:

"Reprinted from Publication title, Vol /edition number, Author(s), Title of article / title of chapter, Pages No., Copyright (Year), with permission from Elsevier [OR APPLICABLE SOCIETY COPYRIGHT OWNER]." Also Lancet special credit - "Reprinted from The Lancet, Vol. number, Author(s), Title of article, Pages No., Copyright (Year), with permission from Elsevier."

4. Reproduction of this material is confined to the purpose and/or media for which permission is hereby given.

5. Altering/Modifying Material: Not Permitted. However figures and illustrations may be altered/adapted minimally to serve your work. Any other abbreviations, additions, deletions and/or any other alterations shall be made only with prior written authorization of Elsevier Ltd. (Please contact Elsevier at [permissions@elsevier.com](mailto:permissions@elsevier.com))

6. If the permission fee for the requested use of our material is waived in this instance, please be advised that your future requests for Elsevier materials may attract a fee.

7. Reservation of Rights: Publisher reserves all rights not specifically granted in the combination of (i) the license details provided by you and accepted in the course of this licensing transaction, (ii) these terms and conditions and (iii) CCC's Billing and Payment terms and conditions.

8. License Contingent Upon Payment: While you may exercise the rights licensed immediately upon issuance of the license at the end of the licensing process for the transaction, provided that you have disclosed complete and accurate details of your proposed use, no license is finally effective unless and until full payment is received from you (either by publisher or by CCC) as provided in CCC's Billing and Payment terms and conditions. If full payment is not received on a timely basis, then any license preliminarily granted shall be deemed automatically revoked and shall be void as if never granted. Further, in the event that you breach any of these terms and conditions or any of CCC's Billing and Payment terms and conditions, the license is automatically revoked and shall be void as if never granted. Use of materials as described in a revoked license, as well as any use of the materials beyond the scope of an unrevoked license, may constitute copyright infringement and publisher reserves the right to take any and all action to protect its copyright in the materials.

9. Warranties: Publisher makes no representations or warranties with respect to the licensed material.

10. Indemnity: You hereby indemnify and agree to hold harmless publisher and CCC, and their respective officers, directors, employees and agents, from and against any and all claims arising out of your use of the licensed material other than as specifically authorized pursuant to this license.

11. No Transfer of License: This license is personal to you and may not be sublicensed, assigned, or transferred by you to any other person without publisher's written permission.

12. No Amendment Except in Writing: This license may not be amended except in a writing signed by both parties (or, in the case of publisher, by CCC on publisher's behalf).

13. Objection to Contrary Terms: Publisher hereby objects to any terms contained in any purchase order, acknowledgment, check endorsement or other writing prepared by you, which terms are inconsistent with these terms and conditions or CCC's Billing and Payment terms and conditions. These terms and conditions, together with CCC's Billing and Payment terms and conditions (which are incorporated herein), comprise the entire agreement between you and publisher (and CCC) concerning this licensing transaction. In the event of any conflict between your obligations established by these terms and conditions and those established by CCC's Billing and Payment terms and conditions, these terms and conditions shall control.

14. Revocation: Elsevier or Copyright Clearance Center may deny the permissions described in this License at their sole discretion, for any reason or no reason, with a full refund payable to you. Notice of such denial will be made using the contact information provided by you. Failure to receive such notice will not alter or invalidate the denial. In no event will Elsevier or Copyright Clearance Center be responsible or liable for any costs, expenses or damage incurred by you as a result of a denial of your permission request, other than a refund of the amount(s) paid by you to Elsevier and/or Copyright Clearance Center for

2 of 4

06/22/2012 10:01 AM

## Appendix H: (Continued)

RightsLink - Your Account

<https://s100.copyright.com/MyAccount/viewPrintableLic...>

denied permissions.

### LIMITED LICENSE

The following terms and conditions apply only to specific license types:

15. **Translation:** This permission is granted for non-exclusive world **English** rights only unless your license was granted for translation rights. If you licensed translation rights you may only translate this content into the languages you requested. A professional translator must perform all translations and reproduce the content word for word preserving the integrity of the article. If this license is to re-use 1 or 2 figures then permission is granted for non-exclusive world rights in all languages.

16. **Website:** The following terms and conditions apply to electronic reserve and author websites:

**Electronic reserve:** If licensed material is to be posted to website, the web site is to be password-protected and made available only to bona fide students registered on a relevant course if:

This license was made in connection with a course,

This permission is granted for 1 year only. You may obtain a license for future website posting.

All content posted to the web site must maintain the copyright information line on the bottom of each image.

A hyper-text must be included to the Homepage of the journal from which you are licensing at <http://www.sciencedirect.com/science/journal/xxxxx> or the Elsevier homepage for books at <http://www.elsevier.com> , and

Central Storage: This license does not include permission for a scanned version of the material to be stored in a central repository such as that provided by Heron/XanEdu.

17. **Author website** for journals with the following additional clauses:

All content posted to the web site must maintain the copyright information line on the bottom of each image, and the permission granted is limited to the personal version of your paper. You are not allowed to download and post the published electronic version of your article (whether PDF or HTML, proof or final version), nor may you scan the printed edition to create an electronic version. A hyper-text must be included to the Homepage of the journal from which you are licensing at

<http://www.sciencedirect.com/science/journal/xxxxx> . As part of our normal production process, you will receive an e-mail notice when your article appears on Elsevier's online service ScienceDirect ([www.sciencedirect.com](http://www.sciencedirect.com)). That e-mail will include the article's Digital Object Identifier (DOI). This number provides the electronic link to the published article and should be included in the posting of your personal version. We ask that you wait until you receive this e-mail and have the DOI to do any posting.

Central Storage: This license does not include permission for a scanned version of the material to be stored in a central repository such as that provided by Heron/XanEdu.

18. **Author website** for books with the following additional clauses:

Authors are permitted to place a brief summary of their work online only.

A hyper-text must be included to the Elsevier homepage at <http://www.elsevier.com> . All content posted to the web site must maintain the copyright information line on the bottom of each image. You are not allowed to download and post the published electronic version of your chapter, nor may you scan the printed edition to create an electronic version.

Central Storage: This license does not include permission for a scanned version of the material to be stored in a central repository such as that provided by Heron/XanEdu.

19. **Website** (regular and for author): A hyper-text must be included to the Homepage of the journal from which you are licensing at <http://www.sciencedirect.com/science/journal/xxxxx> , or for books to the Elsevier homepage at <http://www.elsevier.com>

20. **Thesis/Dissertation:** If your license is for use in a thesis/dissertation your thesis may be submitted to your institution in either print or electronic form. Should your thesis be published commercially, please reapply for permission. These requirements include permission for the Library and Archives of Canada to supply single copies, on demand, of the complete thesis and include permission for UMI to supply single copies, on demand, of the complete thesis. Should your thesis be published commercially, please reapply for permission.

21. **Other Conditions:**

v1.6

If you would like to pay for this license now, please remit this license along with your payment made payable to "COPYRIGHT CLEARANCE CENTER" otherwise you will be invoiced within 48 hours of the license date. Payment should be in the form of a check or money order referencing your account number and this invoice number RLNK500804843. Once you receive your invoice for this order, you may pay your invoice by credit card. Please follow instructions provided at that time.

**Make Payment To:**  
Copyright Clearance Center  
Dept 001  
P.O. Box 843006  
Boston, MA 02284-3006

For suggestions or comments regarding this order, contact RightsLink Customer Support: [customer@copyright.com](mailto:customer@copyright.com)

## Appendix H: (Continued)

RightsLink - Your Account

<https://s100.copyright.com/MyAccount/viewPrintableLic...>

or +1-877-622-5543 (toll free in the US) or +1-978-646-2777.

Gratis licenses (referencing S0 in the Total field) are free. Please retain this printable license for your reference. No payment is required.

---

---

## Appendix H: (Continued)

### H.1.2 Permission to Use Figure 1.4

Rightslink Printable License

<https://s100.copyright.com/App/PrintableLicenseFrame.j...>

#### ELSEVIER LICENSE TERMS AND CONDITIONS

Jun 22, 2012

---

This is a License Agreement between Cigdem Akan ("You") and Elsevier ("Elsevier") provided by Copyright Clearance Center ("CCC"). The license consists of your order details, the terms and conditions provided by Elsevier, and the payment terms and conditions.

**All payments must be made in full to CCC. For payment instructions, please see information listed at the bottom of this form.**

Supplier	Elsevier Limited The Boulevard, Langford Lane Kidlington, Oxford, OX5 1GB, UK
Registered Company Number	1982084
Customer name	Cigdem Akan
Customer address	717 SW 4th Street #2 Corvallis, OR 97333
License number	2934310208269
License date	Jun 22, 2012
Licensed content publisher	Elsevier
Licensed content publication	Continental Shelf Research
Licensed content title	Infrared imagery of large-aspect-ratio Langmuir circulation
Licensed content author	G.O. Marmorino, G.B. Smith, G.J. Lindemann
Licensed content date	January 2005
Licensed content volume number	25
Licensed content issue number	1
Number of pages	6
Start Page	1
End Page	6
Type of Use	reuse in a thesis/dissertation
Intended publisher of new work	other
Portion	figures/tables/illustrations
Number of figures/tables /illustrations	1
Format	electronic
Are you the author of this Elsevier article?	No
Will you be translating?	No
Order reference number	
Title of your thesis/dissertation	Surface Mass Transfer in Large Eddy Simulation (LES) of Langmuir Turbulence

1 of 6

06/22/2012 10:05 AM

## Appendix H: (Continued)

Rightslink Printable License

<https://s100.copyright.com/App/PrintableLicenseFrame.j...>

Expected completion date	Aug 2012
Estimated size (number of pages)	145
Elsevier VAT number	GB 494 6272 12
Permissions price	0.00 USD
VAT/Local Sales Tax	0.0 USD / 0.0 GBP
Total	0.00 USD
<a href="#">Terms and Conditions</a>	

### INTRODUCTION

1. The publisher for this copyrighted material is Elsevier. By clicking "accept" in connection with completing this licensing transaction, you agree that the following terms and conditions apply to this transaction (along with the Billing and Payment terms and conditions established by Copyright Clearance Center, Inc. ("CCC"), at the time that you opened your Rightslink account and that are available at any time at <http://myaccount.copyright.com>).

### GENERAL TERMS

2. Elsevier hereby grants you permission to reproduce the aforementioned material subject to the terms and conditions indicated.

3. Acknowledgement: If any part of the material to be used (for example, figures) has appeared in our publication with credit or acknowledgement to another source, permission must also be sought from that source. If such permission is not obtained then that material may not be included in your publication/copies. Suitable acknowledgement to the source must be made, either as a footnote or in a reference list at the end of your publication, as follows:

"Reprinted from Publication title, Vol /edition number, Author(s), Title of article / title of chapter, Pages No., Copyright (Year), with permission from Elsevier [OR APPLICABLE SOCIETY COPYRIGHT OWNER]." Also Lancet special credit - "Reprinted from The Lancet, Vol. number, Author(s), Title of article, Pages No., Copyright (Year), with permission from Elsevier."

4. Reproduction of this material is confined to the purpose and/or media for which permission is hereby given.

5. Altering/Modifying Material: Not Permitted. However figures and illustrations may be altered/adapted minimally to serve your work. Any other abbreviations, additions, deletions and/or any other alterations shall be made only with prior written authorization of Elsevier Ltd. (Please contact Elsevier at [permissions@elsevier.com](mailto:permissions@elsevier.com))



## Appendix H: (Continued)

Rightslink Printable License

<https://s100.copyright.com/App/PrintableLicenseFrame.j...>

6. If the permission fee for the requested use of our material is waived in this instance, please be advised that your future requests for Elsevier materials may attract a fee.

7. Reservation of Rights: Publisher reserves all rights not specifically granted in the combination of (i) the license details provided by you and accepted in the course of this licensing transaction, (ii) these terms and conditions and (iii) CCC's Billing and Payment terms and conditions.

8. License Contingent Upon Payment: While you may exercise the rights licensed immediately upon issuance of the license at the end of the licensing process for the transaction, provided that you have disclosed complete and accurate details of your proposed use, no license is finally effective unless and until full payment is received from you (either by publisher or by CCC) as provided in CCC's Billing and Payment terms and conditions. If full payment is not received on a timely basis, then any license preliminarily granted shall be deemed automatically revoked and shall be void as if never granted. Further, in the event that you breach any of these terms and conditions or any of CCC's Billing and Payment terms and conditions, the license is automatically revoked and shall be void as if never granted. Use of materials as described in a revoked license, as well as any use of the materials beyond the scope of an unrevoked license, may constitute copyright infringement and publisher reserves the right to take any and all action to protect its copyright in the materials.

9. Warranties: Publisher makes no representations or warranties with respect to the licensed material.

10. Indemnity: You hereby indemnify and agree to hold harmless publisher and CCC, and their respective officers, directors, employees and agents, from and against any and all claims arising out of your use of the licensed material other than as specifically authorized pursuant to this license.

11. No Transfer of License: This license is personal to you and may not be sublicensed, assigned, or transferred by you to any other person without publisher's written permission.

12. No Amendment Except in Writing: This license may not be amended except in a writing signed by both parties (or, in the case of publisher, by CCC on publisher's behalf).

13. Objection to Contrary Terms: Publisher hereby objects to any terms contained in any purchase order, acknowledgment, check endorsement or other writing prepared by you, which terms are inconsistent with these terms and conditions or CCC's Billing and Payment terms and conditions. These terms and conditions, together with CCC's Billing and

3 of 6

06/22/2012 10:05 AM

## Appendix H: (Continued)

Rightslink Printable License

<https://s100.copyright.com/App/PrintableLicenseFrame.j...>

Payment terms and conditions (which are incorporated herein), comprise the entire agreement between you and publisher (and CCC) concerning this licensing transaction. In the event of any conflict between your obligations established by these terms and conditions and those established by CCC's Billing and Payment terms and conditions, these terms and conditions shall control.

14. **Revocation:** Elsevier or Copyright Clearance Center may deny the permissions described in this License at their sole discretion, for any reason or no reason, with a full refund payable to you. Notice of such denial will be made using the contact information provided by you. Failure to receive such notice will not alter or invalidate the denial. In no event will Elsevier or Copyright Clearance Center be responsible or liable for any costs, expenses or damage incurred by you as a result of a denial of your permission request, other than a refund of the amount(s) paid by you to Elsevier and/or Copyright Clearance Center for denied permissions.

### LIMITED LICENSE

The following terms and conditions apply only to specific license types:

15. **Translation:** This permission is granted for non-exclusive world **English** rights only unless your license was granted for translation rights. If you licensed translation rights you may only translate this content into the languages you requested. A professional translator must perform all translations and reproduce the content word for word preserving the integrity of the article. If this license is to re-use 1 or 2 figures then permission is granted for non-exclusive world rights in all languages.

16. **Website:** The following terms and conditions apply to electronic reserve and author websites:

**Electronic reserve:** If licensed material is to be posted to website, the web site is to be password-protected and made available only to bona fide students registered on a relevant course if:

This license was made in connection with a course,

This permission is granted for 1 year only. You may obtain a license for future website posting,

All content posted to the web site must maintain the copyright information line on the bottom of each image,

A hyper-text must be included to the Homepage of the journal from which you are licensing at <http://www.sciencedirect.com/science/journal/xxxx> or the Elsevier homepage for books at <http://www.elsevier.com> , and

Central Storage: This license does not include permission for a scanned version of the material to be stored in a central repository such as that provided by Heron/XanEdu.

## Appendix H: (Continued)

17. **Author website** for journals with the following additional clauses:

All content posted to the web site must maintain the copyright information line on the bottom of each image, and the permission granted is limited to the personal version of your paper. You are not allowed to download and post the published electronic version of your article (whether PDF or HTML, proof or final version), nor may you scan the printed edition to create an electronic version. A hyper-text must be included to the Homepage of the journal from which you are licensing at <http://www.sciencedirect.com/science/journal/xxxxx> . As part of our normal production process, you will receive an e-mail notice when your article appears on Elsevier's online service ScienceDirect (www.sciencedirect.com). That e-mail will include the article's Digital Object Identifier (DOI). This number provides the electronic link to the published article and should be included in the posting of your personal version. We ask that you wait until you receive this e-mail and have the DOI to do any posting.

Central Storage: This license does not include permission for a scanned version of the material to be stored in a central repository such as that provided by Heron/XanEdu.

18. **Author website** for books with the following additional clauses: Authors are permitted to place a brief summary of their work online only.

A hyper-text must be included to the Elsevier homepage at <http://www.elsevier.com> . All content posted to the web site must maintain the copyright information line on the bottom of each image. You are not allowed to download and post the published electronic version of your chapter, nor may you scan the printed edition to create an electronic version.

Central Storage: This license does not include permission for a scanned version of the material to be stored in a central repository such as that provided by Heron/XanEdu.

19. **Website** (regular and for author): A hyper-text must be included to the Homepage of the journal from which you are licensing at <http://www.sciencedirect.com/science/journal/xxxxx> . or for books to the Elsevier homepage at <http://www.elsevier.com>

20. **Thesis/Dissertation**: If your license is for use in a thesis/dissertation your thesis may be submitted to your institution in either print or electronic form. Should your thesis be published commercially, please reapply for permission. These requirements include permission for the Library and Archives of Canada to supply single copies, on demand, of the complete thesis and include permission for

## Appendix H: (Continued)

Rightslink Printable License

<https://s100.copyright.com/App/PrintableLicenseFrame.j...>

UMI to supply single copies, on demand, of the complete thesis. Should your thesis be published commercially, please reapply for permission.

### 21. Other Conditions:

v1.6

If you would like to pay for this license now, please remit this license along with your payment made payable to "COPYRIGHT CLEARANCE CENTER" otherwise you will be invoiced within 48 hours of the license date. Payment should be in the form of a check or money order referencing your account number and this invoice number RLNK500804898.  
Once you receive your invoice for this order, you may pay your invoice by credit card. Please follow instructions provided at that time.

Make Payment To:  
Copyright Clearance Center  
Dept 001  
P.O. Box 843006  
Boston, MA 02284-3006

For suggestions or comments regarding this order, contact RightsLink Customer Support:  
[customercare@copyright.com](mailto:customercare@copyright.com) or +1-877-622-5543 (toll free in the US) or +1-978-646-2777.

Gratis licenses (referencing \$0 in the Total field) are free. Please retain this printable license for your reference. No payment is required.

---

---

## Appendix H: (Continued)

### H.2 Permissions to Use the Figures in Chapter 2

#### H.2.1 Permission to Use Figure 2.1

Rightslink Printable License

<https://s100.copyright.com/App/PrintableLicenseFrame.j...>

#### AMERICAN INSTITUTE OF PHYSICS LICENSE TERMS AND CONDITIONS

Jun 22, 2012

**All payments must be made in full to CCC. For payment instructions, please see information listed at the bottom of this form.**

License Number	2934341224786
Order Date	Jun 22, 2012
Publisher	American Institute of Physics
Publication	Physics of Fluids 1958-1988
Article Title	Structure and dynamics of round turbulent jets
Author	Paul E. Dimotakis, Richard C. Miake-Lye, Dimitris A. Papantoniou
Online Publication Date	Nov 1, 1983
Volume number	26
Issue number	11
Type of Use	Thesis/Dissertation
Requestor type	Student
Format	Electronic
Portion	Figure/Table
Number of figures/tables	1
Title of your thesis / dissertation	Surface Mass Transfer in Large Eddy Simulation (LES) of Langmuir Turbulence
Expected completion date	Aug 2012
Estimated size (number of pages)	145
Total	0.00 USD

#### Terms and Conditions

American Institute of Physics -- Terms and Conditions: Permissions Uses

American Institute of Physics ("AIP") hereby grants to you the non-exclusive right and license to use and/or distribute the Material according to the use specified in your order, on a one-time basis, for the specified term, with a maximum distribution equal to the number that you have ordered. Any links or other content accompanying the Material are not the subject of this license.

1. You agree to include the following copyright and permission notice with the reproduction of the Material: "Reprinted with permission from [FULL CITATION]. Copyright [PUBLICATION YEAR], American Institute of Physics." For an article, the copyright and permission notice must be printed on the first page of the article or book chapter. For photographs, covers, or tables, the copyright and permission notice may appear with the Material, in a footnote, or in the reference list.
2. If you have licensed reuse of a figure, photograph, cover, or table, it is your responsibility to ensure that the material is original to AIP and does not contain the copyright of another entity, and that the copyright notice of the figure, photograph, cover, or table does not indicate that it was reprinted by AIP, with permission, from another

## Appendix H: (Continued)

Rightslink Printable License

<https://s100.copyright.com/App/PrintableLicenseFrame.j...>

source. Under no circumstances does AIP, purport or intend to grant permission to reuse material to which it does not hold copyright.

3. You may not alter or modify the Material in any manner. You may translate the Material into another language only if you have licensed translation rights. You may not use the Material for promotional purposes. AIP reserves all rights not specifically granted herein.
4. The foregoing license shall not take effect unless and until AIP or its agent, Copyright Clearance Center, receives the Payment in accordance with Copyright Clearance Center Billing and Payment Terms and Conditions, which are incorporated herein by reference.
5. AIP or the Copyright Clearance Center may, within two business days of granting this license, revoke the license for any reason whatsoever, with a full refund payable to you. Should you violate the terms of this license at any time, AIP, American Institute of Physics, or Copyright Clearance Center may revoke the license with no refund to you. Notice of such revocation will be made using the contact information provided by you. Failure to receive such notice will not nullify the revocation.
6. AIP makes no representations or warranties with respect to the Material. You agree to indemnify and hold harmless AIP, American Institute of Physics, and their officers, directors, employees or agents from and against any and all claims arising out of your use of the Material other than as specifically authorized herein.
7. The permission granted herein is personal to you and is not transferable or assignable without the prior written permission of AIP. This license may not be amended except in a writing signed by the party to be charged.
8. If purchase orders, acknowledgments or check endorsements are issued on any forms containing terms and conditions which are inconsistent with these provisions, such inconsistent terms and conditions shall be of no force and effect. This document, including the CCC Billing and Payment Terms and Conditions, shall be the entire agreement between the parties relating to the subject matter hereof.

This Agreement shall be governed by and construed in accordance with the laws of the State of New York. Both parties hereby submit to the jurisdiction of the courts of New York County for purposes of resolving any disputes that may arise hereunder.

**If you would like to pay for this license now, please remit this license along with your payment made payable to "COPYRIGHT CLEARANCE CENTER" otherwise you will be invoiced within 48 hours of the license date. Payment should be in the form of a check or money order referencing your account number and this invoice number RLNK500804945.**

**Once you receive your invoice for this order, you may pay your invoice by credit card. Please follow instructions provided at that time.**

**Make Payment To:**

## Appendix H: (Continued)

Rightslink Printable License

<https://s100.copyright.com/App/PrintableLicenseFrame.j...>

Copyright Clearance Center  
Dept 001  
P.O. Box 843006  
Boston, MA 02284-3006

For suggestions or comments regarding this order, contact RightsLink Customer Support:  
[customercare@copyright.com](mailto:customercare@copyright.com) or +1-877-622-5543 (toll free in the US) or +1-978-646-2777.



Gratis licenses (referencing \$0 in the Total field) are free. Please retain this printable license for your reference. No payment is required.

---

---


## Appendix H: (Continued)

### H.2.2 Permission to Use Figure 2.2

 **adil.rasheed**  3:38 PM (22 minutes ago) ☆ ↶ ▾  
to me ▾

Dear Cigdem. Thanks a lot for informing me about your desire to include the slide in your presentation. Go ahead and use it. All the best for your defense.

adil  
\*\*\*

On 27 June 2012 21:01, Cigdem Akan < > wrote:  
Dear Adil Rasheed,

I am currently a PhD candidate at University of South Florida working towards to obtain my degree by August, 2012. I respectfully ask to use the figure on slide 4 of your power point presentation titled "Turbulence Modelling: Large Eddy Simulation" (which is attached), in my USF Dissertation titled "Surface Mass Transfer in Large Eddy Simulation (LES) of Langmuir Turbulence". Please note that I found this presentation online, from your personal webpage:

<http://www.adilrasheed.com/blog/>



I would be really glad if you could let me know by July, 1 which is the deadline to submit my dissertation. I appreciate your help on this.

Kind Regards,



## Appendix H: (Continued)

### H.2.3 Permission to Use Figure 2.3

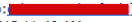

 Tejada-Martinez, Andres  Jun 26 (1 day ago) ☆ ↶ ▾  
to me ▾

Cigdem,

Yes, please use it.

Andres

---

**From:** Cigdem Akan [mailto:  
**Sent:** Tuesday, June 26, 2012 11:40 AM  
**To:** Tejada-Martinez, Andres  
**Subject:** Copyright  


Dr. Tejada,

I need to obtain copyright for every previously published figure/table that I used in my dissertation. Thus, I respectfully ask to use the figure 1.2 on page 11 of your PhD dissertation title "Dynamic Subgrid-scale Modeling for Large-Eddy Simulation of Turbulent Flows with a Stabilized Finite Element Method", in my USF Dissertation titled "Surface Mass Transfer in Large Eddy Simulation (LES) of Langmuir Turbulence".

Please do let me know and I appreciate your help!

--  
Cigdem AKAN

## Appendix H: (Continued)

Terms & Conditions - ProQuest

<http://search.proquest.com.ezproxy.lib.usf.edu/info/term...>

[Basic Search](#) [Advanced](#) [Publications](#) [Browse](#) [Preferences](#) [English](#) [Help](#)



### Terms & Conditions

#### Terms and Conditions

[Chadwyck-Healey](#) | [COS](#) | [CSA](#) | [eLibrary](#) | [HeritageQuest](#) | [ProQuest](#) | [Micromedia ProQuest](#) | [RefWorks](#) | [Serials Solutions](#) | [UMI Dissertation Publishing](#) | [UMI Microfilm](#)

By accessing the Product(s), you, the Institution listed on the Order Form, agree that you and your Authorized Users are bound as follows:

1. **License Grant.** Subject to the terms of this Agreement, ProQuest LLC ("ProQuest") hereby grants you a non-exclusive, non-transferable license to access and use the products listed on your approved Order Form, invoice or purchase order (the "Products") solely at your principal location and those locations listed on the Additional Sites/Member Libraries Schedule. Any remote access rights and/or limits on simultaneous users are specified on the Order Form. Except as expressly set forth in this Agreement, you do not acquire any intellectual property rights in the Products or any associated software, systems, documentation or other materials. All such rights and interests remain in ProQuest and its licensors.
2. **Authorized Users.** By "Authorized User" we mean only: (1) For public libraries: library staff, individual residents of your reasonably defined geographic area served and walk-in patrons while they are on-site; (2) For schools and other academic institutions: currently enrolled students, faculty, staff, visiting scholars and walk-in patrons while they are on-site; and (3) For other types of organizations: your employees, independent contractors and other temporary workers while they are performing duties within the scope of their employment or assignment.
3. **Remote Access.** If your subscription allows you to provide remote access to a Product, you will strictly limit such access to Authorized Users through the use of passwords, IP addresses or other secure method of user verification. You will not share access with other schools, libraries, institutions or third parties either directly or indirectly, unless such school, library, institution, or third party is listed on the Additional Sites/Member Libraries Schedule. You will immediately notify us if you believe your security has been compromised.
4. **No Redistribution.** ProQuest endorses the Interlibrary Loan and Scholarly Sharing provisions below. Beyond these uses, you may not redistribute any material retrieved from the Products nor allow any use that will infringe the copyright or other proprietary right of ProQuest or its licensors. You may not use the Products to create products or perform services which compete or interfere with those of ProQuest or its licensors.
5. **Permitted Uses.** The Products may be used for your internal research or educational purposes, as follows:
  - a. **Research and Analysis.** You and your Authorized Users are permitted to display and use information contained in the Products for educational, scientific, or research purposes, including illustration, explanation, example, comment, criticism, teaching, research or analysis, provided that in doing so you or your Authorized Users do not violate an express provision of this Agreement.
  - b. **Digital and Print Copies.** You and your Authorized Users may download or create printouts of a reasonable portion of the articles or other works contained in the Products so long as each work is retrieved directly from the on-line database system in a manner that causes a "hit" to be registered on the on-line system for each and every print or digital copy. All reproduction and distribution of such printouts, and all downloading and electronic storage of materials retrieved through the Products shall be for your own internal or personal use as allowed under the doctrines of "fair use" and "fair dealing". Downloading of all or parts of a Product in a systematic or regular manner or so as to create a collection of materials comprising all or a material subset of a Product is strictly prohibited whether such collection is in electronic or print form.
  - c. **Electronic Reserves.** Articles or other works contained in a Product may be included in your electronic reserves systems so long as such use employs durable links to the Products so that a "hit" is registered on ProQuest's on-line platform each time a student views the work on reserve.
  - d. **Fair Use/Fair Dealing.** Nothing in this agreement restricts your use of the materials contained within the Products under the doctrines of "fair use" or "fair dealing" as defined under the laws of the United States or England, respectively.
  - e. **Interlibrary Loan (ILL).** Interlibrary Loan of materials retrieved from the Products is allowed provided that the loan is not done in a manner or magnitude that would replace the recipient library's own subscription to either the Products or the purchase of the underlying Work (e.g., newspaper, magazine or book), and that you comply with any special terms imposed by specific content providers or licensors as required under Section 6(c). With respect to our ProQuest® Dissertations & Theses product and other electronic archives such as Early English Books Online, Interlibrary Loan is restricted to one *printed* copy of the specifically requested dissertation, book or pamphlet loaned out at any one time.
  - f. **Scholarly Sharing.** You and your Authorized Users may provide to a third party colleague minimal, insubstantial amounts of materials retrieved from the Products for personal use or scholarly, educational or scientific research use in hard copy or electronically, provided that in no case any such sharing is done in a manner or magnitude as to act as a replacement for the recipient's or recipient institution's own subscription to either the Products or the purchase of the underlying Work.
  - g. **MARC Records.** You may load ProQuest's MARC record Products into your Online Public Access Catalog (OPAC) containing your library holdings provided such records are not loaded into a shared online catalog system such as WorldCat without ProQuest's prior written consent.
  - h. **Scholar/Researcher Profiles.** The data contained within scholar profiles within our products are for use in facilitating research and collaboration amongst colleagues. Neither you nor your Authorized Users may export or otherwise exploit the scholar profiles for mass mailings or similar marketing purposes.
6. **Supplemental Terms.**
  - a. **Updates.** ProQuest will announce any substantial additions, deletions or modifications of information, databases, materials, capabilities or services within the Products on its electronic mailing list service. These shall be subject to the terms and conditions of this Agreement at the time they are added to the Products, but shall not materially alter your use of the Products.
  - b. **Systems Usage.** To protect the Products for the research and educational use of Authorized Users, automated searches against ProQuest's systems are not permitted with the exception of nonburdensome federated search services. Data mining is prohibited.
  - c. **Content Provider Supplemental Terms.** Individual content licensors occasionally have conditions of use applicable solely to their content. Links to such content-specific conditions are clearly displayed with the associated content and will not materially alter your use of the Products. With respect to third-party databases delivered through the Illumina platform, any supplemental terms and conditions are clearly hypertext linked on each search screen.
7. **Fees and Payments.** You agree pay the fees for the Products as shown on the order form, attached invoice, or accepted purchase order within thirty (30) days of your receipt of ProQuest's invoice. Firm U.S. Government orders require a valid purchase order and advance payment or payment in accordance with FAR 52.213.2.
8. **Term and Termination.**
  - a. **Term.** For subscription-based Products, the term of your rights and access shall continue from the Start Date until the Expiration Date as those are listed on the Order Form or an accepted purchase order for each such Product, plus any renewal term(s) agreed to.

## Appendix H: (Continued)

Terms & Conditions - ProQuest

<http://search.proquest.com.ezproxy.lib.usf.edu/info/term...>

For CD-ROM, FTP databases, and other tangible media, you are granted a perpetual license to the most current version purchased, subject to the continued application of Acceptable Use Provisions of this Agreement (Section 1-6, above). This Agreement shall continue in force for so long as you are within the term of at least one ProQuest Product.

b. **Termination for Breach.** If a party breaches any material term of this Agreement and does not cure after 30 days written notice, the Agreement may immediately be terminated in whole or as to the affected Product. In the event the license granted under this agreement is terminated you shall disable all Products in your possession. This includes the destruction of any CD-ROMs, FTP databases or any software as well as any downloaded copies retrieved from the Products. In addition, ProQuest reserves the right to pursue any other legal remedy available to it.

c. **Remedial Action.** Without limiting the above, ProQuest may suspend delivery of Product(s) to you if it reasonably determines that your failure to comply with the Acceptable Use Provisions may cause irreparable harm to it or its licensors under the specific circumstances. If delivery is suspended, ProQuest will work with you in good faith to restore your access as soon as possible.

9. **Privacy.** The Products do not require the entering or capture of personally identifiable user information. ProQuest makes no representation as to whether any federal, state or local laws may regulate your administration of Authorized Users' access to the Products or require you to obtain consent from any Authorized User (or, in the case of minors, the parent or guardian of such user).

### 10. **Access and Use.**

a. ProQuest® CD-ROM Products may include software to be used in connection with the Products. It may not be reverse engineered or used for any other purpose.

b. You are responsible for local telecommunication connections if they are needed and any related third party charges.

c. ProQuest may seek to assist you from time to time regarding hardware and software compatibility with the Products, however PROQUEST SPECIFICALLY DISCLAIMS ANY RESPONSIBILITY FOR DETERMINING THE COMPATIBILITY OF ANY HARDWARE OR SOFTWARE NOT SUPPLIED BY PROQUEST WITH THE PRODUCTS AND PROVIDES NO WARRANTY WITH RESPECT TO THE OPERATION OF SUCH HARDWARE OR SOFTWARE WITH THE PRODUCTS.

### 11. **U.S. Government Restricted Rights.**

The Products include materials that are commercial technical data and/or computer databases and/or commercial computer software, as applicable, which were developed exclusively at private expense by ProQuest LLC (f/k/a ProQuest Information and Learning Company and/or Cambridge Scientific Abstracts LP and/or ProQuest-CSA LLC) 789 E. Eisenhower Parkway, Ann Arbor, MI 48108. U.S. Government rights to use, modify, reproduce, release, perform, display, or disclose these technical data and/or computer databases and/or computer software are subject to the limited rights restrictions of DFARS 252.227-7202-3 (June 2005) Rights in Computer Software and Computer Software Documentation and/or subject to the restrictions of DFARS 252.227-7019 (June 1995) Validation of Asserted Restrictions - Computer Software, as applicable for U.S. Department of Defense procurements and the limited rights restrictions of FAR 52.227-14 (June 1987) Rights in Data-General, FAR 52.227-20(c)(2-3) (March 1994) Rights in Data-SBIR Program and/or subject to the restricted rights provisions of FAR 52.227-15 (May 1999) Representation of Limited Rights Data and Restricted Computer Software and FAR 52.227-19 (June 1987) Commercial Computer Software-Restricted Rights, as applicable, and any applicable agency FAR Supplements, for non-Department of Defense Federal procurement.

12. **EEOC Statement.** ProQuest agrees to comply with all provisions of Executive Order 11246 of September 24, 1965, and all rules, regulations and relevant orders of the Secretary of Labor related to equality of employment opportunity which Executive Order, rules, regulations and orders are incorporated herein by reference.

13. **Limited Warranty and Disclaimer of Warranty.** ProQuest warrants that it has all rights necessary to enter into this Agreement and to provide the Products to you. EXCEPT AS PROVIDED IN THE PRECEDING SENTENCE, THE PRODUCTS AND ALL EQUIPMENT AND SOFTWARE PROVIDED BY PROQUEST TO YOU ARE PROVIDED "AS IS" AND "AS AVAILABLE." THE WARRANTIES IN THIS AGREEMENT ARE IN LIEU OF ALL OTHER WARRANTIES, EXPRESS OR IMPLIED, INCLUDING WITHOUT LIMITATION, ANY WARRANTIES OF MERCHANTABILITY, OR FITNESS FOR A PARTICULAR PURPOSE. WITHOUT LIMITING THE FOREGOING, NEITHER PROQUEST NOR ANY PROVIDER OF INFORMATION OR SOFTWARE IN THE PRODUCTS WARRANTS THE USE OF THE PRODUCTS OR THAT THE SOFTWARE OR SYSTEMS WILL BE UNINTERRUPTED OR ERROR-FREE OR MAKES ANY WARRANTY AS TO THE AVAILABILITY OF THE PRODUCTS, THE ACCURACY, TIMELINESS, CORRECTNESS, RELIABILITY, CURRENCY OR COMPLETENESS OF THE INFORMATION OR THE RESULTS OF YOUR USE OF THE PRODUCTS, THE SOFTWARE OR THE INFORMATION, EVEN IF ASSISTED BY PROQUEST.

14. **Limitation of Liability.** THE MAXIMUM LIABILITY OF PROQUEST AND ITS LICENSORS ARISING OUT OF ANY CLAIM RELATED TO THE PRODUCTS WHETHER IN CONTRACT, TORT OR OTHERWISE SHALL BE LIMITED TO THE TOTAL AMOUNT OF FEES RECEIVED BY PROQUEST FROM YOU FOR THE PRODUCT AT ISSUE UP TO THE TIME THE CAUSE OF ACTION GIVING RISE TO SUCH LIABILITY OCCURRED. IN NO EVENT SHALL PROQUEST OR ITS LICENSORS BE LIABLE TO YOU FOR ANY LOST PROFITS, OR ANY OTHER INDIRECT, INCIDENTAL, CONSEQUENTIAL, PUNITIVE OR SPECIAL DAMAGES RELATED TO THE USE OF THE PRODUCTS OR PROQUEST'S FAILURE TO PERFORM ITS OBLIGATIONS UNDER THIS AGREEMENT, REGARDLESS OF WHETHER PROQUEST OR ITS LICENSORS ARE DEEMED NEGLIGENT, EVEN IF IT IS ADVISED OF THE POSSIBILITY OF SUCH DAMAGES.

### 15. **Miscellaneous.**

a. **Place.** ProQuest's principal place of business where this contract is formed and all services will be deemed performed is located at 789 E. Eisenhower Pkwy, Ann Arbor, MI 48108.

b. **Assignment.** You may not assign this Agreement or any right granted hereunder without the prior written consent of ProQuest, which consent shall not unreasonably be withheld.

c. **Taxes.** Except to the extent that you are tax-exempt as to the tax in question, you are responsible for any sales, use, VAT, personal property or other local taxes (except those based on ProQuest's income) or import duties imposed on the Products.

d. **Waiver.** Failure to enforce any provision of this Agreement shall not be construed to be a waiver of such provision.

e. **Force Majeure.** Neither Party shall be liable in damages or have the right to terminate this Agreement for any delay or default in performing hereunder if such delay or default is caused by conditions beyond its control including, but not limited to acts of God, Government Restrictions (including the denial or cancellation of any export or other necessary license), wars, acts of terrorism and/or any other cause beyond the reasonable control of the party whose performance is affected.

f. **Interruption of On-line Products.** Neither ProQuest nor its licensors shall be liable or deemed in default of this Agreement for any failure or delay or interruption in the on-line Products or any failure of any equipment or telecommunications resulting from any cause or circumstance beyond the reasonable control of ProQuest.

g. **Entire Agreement.** This Agreement constitutes the entire agreement between the parties hereto with respect to its subject matter and supersedes any and all previous and contemporaneous understandings or agreements between the parties with respect to the same subject matter and may not be amended, except in a writing signed by the parties. The terms of your Purchase Orders, if any, are for your convenience and do not supersede any term or condition of this Agreement.

h. **Severability.** If any provision of this Agreement is found invalid or unenforceable pursuant to a decree or decision of competent jurisdiction, the remainder of this Agreement shall remain valid and enforceable according to its terms.

011409

[Contact Us](#) [Privacy Policy](#) [Accessibility](#) [Sitemap](#)

Copyright © 2012 ProQuest LLC. All rights reserved. Terms and Conditions

## Appendix H: (Continued)

### H.3 Permission to Use the Figure in Chapter 3

#### H.3.1 Permission to Use Figure 3.1

Scott A. Socolofsky, Scott [REDACTED] 10:49 PM (17 hours ago) ☆ ↶ ▾  
to me ▾

Yes, you may use this figure.

-----  
Scott A. Socolofsky, Associate Professor and Division Head,  
Coastal and Ocean Engineering Division  
Zachry Department of Civil Engineering  
Texas A&M University  
[REDACTED]  
[REDACTED]  
-----  
[REDACTED]

On Jun 26, 2012, at 10:52 AM, "Cigdem Akan" <[REDACTED]><mailto:[REDACTED]>> wrote:

Dear Dr. Socolofsky,

I am currently a PhD candidate at University of South Florida working towards to obtain my degree by August, 2012. I respectfully ask to use the figure 5.1 on page 84 of your Environmental Fluid Mechanics 1 Lecture Notes( which is attached), in my USF Dissertation titled "Surface Mass Transfer in Large Eddy Simulation (LES) of Langmuir Turbulence". Please note that I found the lecture notes online, from website of University of Karlsruhe:

[http://www.ifh.uni-karlsruhe.de/lehre/envflu\\_i/lecture\\_notes/lecture\\_notes.htm](http://www.ifh.uni-karlsruhe.de/lehre/envflu_i/lecture_notes/lecture_notes.htm)

I would be really glad if you could let me know by July, 1 which is the deadline to submit my dissertation. I appreciate your help on this.

Kind Regards,

## Appendix H: (Continued)

### H.4 Permissions to Use the Figures in Appendix A

#### H.4.1 Permission to Use Figure A.1

Rightslink Printable License

[https://s100.copyright.com/CustomerAdmin/PLF.jsp?ID=2012061\\_13...](https://s100.copyright.com/CustomerAdmin/PLF.jsp?ID=2012061_13...)

#### ELSEVIER LICENSE TERMS AND CONDITIONS

Jun 27, 2012

---

---

This is a License Agreement between Cigdem Akan ("You") and Elsevier ("Elsevier") provided by Copyright Clearance Center ("CCC"). The license consists of your order details, the terms and conditions provided by Elsevier, and the payment terms and conditions.

**All payments must be made in full to CCC. For payment instructions, please see information listed at the bottom of this form.**

Supplier	Elsevier Limited The Boulevard, Langford Lane Kidlington, Oxford, OX5 1GB, UK
Registered Company Number	1982084
Customer name	Cigdem Akan
Customer address	717 SW 4th Street #2 Corvallis, OR 97333
License number	2937220540452
License date	Jun 27, 2012
Licensed content publisher	Elsevier
Licensed content publication	Ocean Modelling
Licensed content title	A hybrid spectral/finite-difference large-eddy simulator of turbulent processes in the upper ocean
Licensed content author	Andrés E. Tejada-Martínez, Chester E. Grosch, Ann E. Gargett, Jeff A. Polton, Jerome A. Smith, J.A. MacKinnon
Licensed content date	2009
Licensed content volume number	30
Licensed content issue number	2-3
Number of pages	28
Start Page	115
End Page	142
Type of Use	reuse in a thesis/dissertation
Intended publisher of new work	other
Portion	figures/tables/illustrations
Number of figures/tables /illustrations	1
Format	electronic
Are you the author of this Elsevier article?	No

1 of 6

6/27/2012 3:25 PM

## Appendix H: (Continued)

Rightslink Printable License

[https://s100.copyright.com/CustomerAdmin/PLF.jsp?IID=2012061\\_13...](https://s100.copyright.com/CustomerAdmin/PLF.jsp?IID=2012061_13...)

Will you be translating?	No
Order reference number	
Title of your thesis/dissertation	Surface Mass Transfer in Large Eddy Simulation (LES) of Langmuir Turbulence
Expected completion date	Aug 2012
Estimated size (number of pages)	145
Elsevier VAT number	GB 494 6272 12
Permissions price	0.00 USD
VAT/Local Sales Tax	0.0 USD / 0.0 GBP
Total	0.00 USD
Terms and Conditions	

### INTRODUCTION

1. The publisher for this copyrighted material is Elsevier. By clicking "accept" in connection with completing this licensing transaction, you agree that the following terms and conditions apply to this transaction (along with the Billing and Payment terms and conditions established by Copyright Clearance Center, Inc. ("CCC"), at the time that you opened your Rightslink account and that are available at any time at <http://myaccount.copyright.com>).

### GENERAL TERMS

2. Elsevier hereby grants you permission to reproduce the aforementioned material subject to the terms and conditions indicated.

3. Acknowledgement: If any part of the material to be used (for example, figures) has appeared in our publication with credit or acknowledgement to another source, permission must also be sought from that source. If such permission is not obtained then that material may not be included in your publication/copies. Suitable acknowledgement to the source must be made, either as a footnote or in a reference list at the end of your publication, as follows:

"Reprinted from Publication title, Vol /edition number, Author(s), Title of article / title of chapter, Pages No., Copyright (Year), with permission from Elsevier [OR APPLICABLE SOCIETY COPYRIGHT OWNER]." Also Lancet special credit - "Reprinted from The Lancet, Vol. number, Author(s), Title of article, Pages No., Copyright (Year), with permission from Elsevier."

4. Reproduction of this material is confined to the purpose and/or media for which permission is hereby given.

5. Altering/Modifying Material: Not Permitted. However figures and illustrations may be altered/adapted minimally to serve your work. Any other abbreviations, additions, deletions and/or any other alterations shall be made only with prior written authorization of Elsevier Ltd. (Please contact Elsevier at [permissions@elsevier.com](mailto:permissions@elsevier.com))

2 of 6

6/27/2012 3:25 PM

## Appendix H: (Continued)

Rightslink Printable License

[https://s100.copyright.com/CustomerAdmin/PLF.jsp?IID=2012061\\_13...](https://s100.copyright.com/CustomerAdmin/PLF.jsp?IID=2012061_13...)

6. If the permission fee for the requested use of our material is waived in this instance, please be advised that your future requests for Elsevier materials may attract a fee.

7. Reservation of Rights: Publisher reserves all rights not specifically granted in the combination of (i) the license details provided by you and accepted in the course of this licensing transaction, (ii) these terms and conditions and (iii) CCC's Billing and Payment terms and conditions.

8. License Contingent Upon Payment: While you may exercise the rights licensed immediately upon issuance of the license at the end of the licensing process for the transaction, provided that you have disclosed complete and accurate details of your proposed use, no license is finally effective unless and until full payment is received from you (either by publisher or by CCC) as provided in CCC's Billing and Payment terms and conditions. If full payment is not received on a timely basis, then any license preliminarily granted shall be deemed automatically revoked and shall be void as if never granted. Further, in the event that you breach any of these terms and conditions or any of CCC's Billing and Payment terms and conditions, the license is automatically revoked and shall be void as if never granted. Use of materials as described in a revoked license, as well as any use of the materials beyond the scope of an unrevoked license, may constitute copyright infringement and publisher reserves the right to take any and all action to protect its copyright in the materials.

9. Warranties: Publisher makes no representations or warranties with respect to the licensed material.

10. Indemnity: You hereby indemnify and agree to hold harmless publisher and CCC, and their respective officers, directors, employees and agents, from and against any and all claims arising out of your use of the licensed material other than as specifically authorized pursuant to this license.

11. No Transfer of License: This license is personal to you and may not be sublicensed, assigned, or transferred by you to any other person without publisher's written permission.

12. No Amendment Except in Writing: This license may not be amended except in a writing signed by both parties (or, in the case of publisher, by CCC on publisher's behalf).

13. Objection to Contrary Terms: Publisher hereby objects to any terms contained in any purchase order, acknowledgment, check endorsement or other writing prepared by you, which terms are inconsistent with these terms and conditions or CCC's Billing and Payment terms and conditions. These terms and conditions, together with CCC's Billing and Payment terms and conditions (which are incorporated herein), comprise the entire agreement between you and publisher (and CCC) concerning this licensing transaction. In the event of any conflict between your obligations established by these terms and conditions and those established by CCC's Billing and Payment terms and conditions, these terms and conditions shall control.

14. Revocation: Elsevier or Copyright Clearance Center may deny the permissions described in this License at their sole discretion, for any reason or no reason, with a full refund payable

3 of 6

6/27/2012 3:25 PM

## Appendix H: (Continued)

Rightslink Printable License

[https://s100.copyright.com/CustomerAdmin/PLF.jsp?IID=2012061\\_13...](https://s100.copyright.com/CustomerAdmin/PLF.jsp?IID=2012061_13...)

to you. Notice of such denial will be made using the contact information provided by you. Failure to receive such notice will not alter or invalidate the denial. In no event will Elsevier or Copyright Clearance Center be responsible or liable for any costs, expenses or damage incurred by you as a result of a denial of your permission request, other than a refund of the amount(s) paid by you to Elsevier and/or Copyright Clearance Center for denied permissions.

### LIMITED LICENSE

The following terms and conditions apply only to specific license types:

15. **Translation:** This permission is granted for non-exclusive world **English** rights only unless your license was granted for translation rights. If you licensed translation rights you may only translate this content into the languages you requested. A professional translator must perform all translations and reproduce the content word for word preserving the integrity of the article. If this license is to re-use 1 or 2 figures then permission is granted for non-exclusive world rights in all languages.

16. **Website:** The following terms and conditions apply to electronic reserve and author websites:

**Electronic reserve:** If licensed material is to be posted to website, the web site is to be password-protected and made available only to bona fide students registered on a relevant course if:

This license was made in connection with a course,

This permission is granted for 1 year only. You may obtain a license for future website posting,

All content posted to the web site must maintain the copyright information line on the bottom of each image,

A hyper-text must be included to the Homepage of the journal from which you are licensing at <http://www.sciencedirect.com/science/journal/xxxxx> or the Elsevier homepage for books at <http://www.elsevier.com>, and

Central Storage: This license does not include permission for a scanned version of the material to be stored in a central repository such as that provided by Heron/XanEdu.

17. **Author website** for journals with the following additional clauses:

All content posted to the web site must maintain the copyright information line on the bottom of each image, and the permission granted is limited to the personal version of your paper. You are not allowed to download and post the published electronic version of your article (whether PDF or HTML, proof or final version), nor may you scan the printed edition to create an electronic version. A hyper-text must be included to the Homepage of the journal from which you are licensing at <http://www.sciencedirect.com/science/journal/xxxxx>. As part of our normal production process, you will receive an e-mail notice when your article appears on Elsevier's online service ScienceDirect ([www.sciencedirect.com](http://www.sciencedirect.com)). That e-mail will include the article's Digital Object Identifier (DOI). This number provides the electronic link to the published article and should be included in the posting of your personal version. We ask that you wait until you receive this e-mail and have the DOI to do any posting.



## Appendix H: (Continued)

Rightslink Printable License

[https://s100.copyright.com/CustomerAdmin/PLF.jsp?IID=2012061\\_13...](https://s100.copyright.com/CustomerAdmin/PLF.jsp?IID=2012061_13...)

Central Storage: This license does not include permission for a scanned version of the material to be stored in a central repository such as that provided by Heron/XanEdu.

18. **Author website** for books with the following additional clauses:

Authors are permitted to place a brief summary of their work online only.

A hyper-text must be included to the Elsevier homepage at <http://www.elsevier.com> . All content posted to the web site must maintain the copyright information line on the bottom of each image. You are not allowed to download and post the published electronic version of your chapter, nor may you scan the printed edition to create an electronic version.

Central Storage: This license does not include permission for a scanned version of the material to be stored in a central repository such as that provided by Heron/XanEdu.

19. **Website** (regular and for author): A hyper-text must be included to the Homepage of the journal from which you are licensing at <http://www.sciencedirect.com/science/journal/xxxx> . or for books to the Elsevier homepage at <http://www.elsevier.com>

20. **Thesis/Dissertation**: If your license is for use in a thesis/dissertation your thesis may be submitted to your institution in either print or electronic form. Should your thesis be published commercially, please reapply for permission. These requirements include permission for the Library and Archives of Canada to supply single copies, on demand, of the complete thesis and include permission for UMI to supply single copies, on demand, of the complete thesis. Should your thesis be published commercially, please reapply for permission.

21. **Other Conditions**:

v1.6

If you would like to pay for this license now, please remit this license along with your payment made payable to "COPYRIGHT CLEARANCE CENTER" otherwise you will be invoiced within 48 hours of the license date. Payment should be in the form of a check or money order referencing your account number and this invoice number RLNK500807894.

Once you receive your invoice for this order, you may pay your invoice by credit card. Please follow instructions provided at that time.

Make Payment To:  
Copyright Clearance Center  
Dept 001  
P.O. Box 843006  
Boston, MA 02284-3006

For suggestions or comments regarding this order, contact RightsLink Customer Support: [customercare@copyright.com](mailto:customercare@copyright.com) or +1-877-622-5543 (toll free in the US) or +1-978-646-2777.

Gratis licenses (referencing \$0 in the Total field) are free. Please retain this printable license for your reference. No payment is required.

5 of 6

6/27/2012 3:25 PM

## Appendix H: (Continued)

### H.4.2 Permission to Use Figure A.2

Rightslink Printable License

<https://s100.copyright.com/App/PrintableLicenseFrame.jsp?publisherID...>

#### AMERICAN INSTITUTE OF PHYSICS LICENSE TERMS AND CONDITIONS

Jun 27, 2012

**All payments must be made in full to CCC. For payment instructions, please see information listed at the bottom of this form.**

License Number	2937220804773
Order Date	Jun 27, 2012
Publisher	American Institute of Physics
Publication	Physics of Fluids
Article Title	Study of discrete test filters and finite difference approximations for the dynamic subgrid-scale stress model
Author	F. M. Najjar, D. K. Tafti
Online Publication Date	Apr 1, 1996
Volume number	8
Issue number	4
Type of Use	Thesis/Dissertation
Requestor type	Student
Format	Electronic
Portion	Figure/Table
Number of figures/tables	1
Title of your thesis / dissertation	Surface Mass Transfer in Large Eddy Simulation (LES) of Langmuir Turbulence
Expected completion date	Aug 2012
Estimated size (number of pages)	145
Total	0.00 USD

#### Terms and Conditions

American Institute of Physics -- Terms and Conditions: Permissions Uses

American Institute of Physics ("AIP") hereby grants to you the non-exclusive right and license to use and/or distribute the Material according to the use specified in your order, on a one-time basis, for the specified term, with a maximum distribution equal to the number that you have ordered. Any links or other content accompanying the Material are not the subject of this license.

1. You agree to include the following copyright and permission notice with the reproduction of the Material: "Reprinted with permission from [FULL CITATION]. Copyright [PUBLICATION YEAR], American Institute of Physics." For an article, the copyright and permission notice must be printed on the first page of the article or book chapter. For photographs, covers, or tables, the copyright and permission notice may appear with the Material, in a footnote, or in the reference list.
2. If you have licensed reuse of a figure, photograph, cover, or table, it is your responsibility to ensure that the material is original to AIP and does not contain the copyright of another entity, and that the copyright notice of the figure, photograph, cover, or table does not indicate that it was reprinted by AIP, with permission, from another source. Under no circumstances does AIP, purport or intend to grant

## Appendix H: (Continued)

Rightslink Printable License

<https://s100.copyright.com/App/PrintableLicenseFrame.jsp?publisherID...>

- permission to reuse material to which it does not hold copyright.
3. You may not alter or modify the Material in any manner. You may translate the Material into another language only if you have licensed translation rights. You may not use the Material for promotional purposes. AIP reserves all rights not specifically granted herein.
  4. The foregoing license shall not take effect unless and until AIP or its agent, Copyright Clearance Center, receives the Payment in accordance with Copyright Clearance Center Billing and Payment Terms and Conditions, which are incorporated herein by reference.
  5. AIP or the Copyright Clearance Center may, within two business days of granting this license, revoke the license for any reason whatsoever, with a full refund payable to you. Should you violate the terms of this license at any time, AIP, American Institute of Physics, or Copyright Clearance Center may revoke the license with no refund to you. Notice of such revocation will be made using the contact information provided by you. Failure to receive such notice will not nullify the revocation.
  6. AIP makes no representations or warranties with respect to the Material. You agree to indemnify and hold harmless AIP, American Institute of Physics, and their officers, directors, employees or agents from and against any and all claims arising out of your use of the Material other than as specifically authorized herein.
  7. The permission granted herein is personal to you and is not transferable or assignable without the prior written permission of AIP. This license may not be amended except in a writing signed by the party to be charged.
  8. If purchase orders, acknowledgments or check endorsements are issued on any forms containing terms and conditions which are inconsistent with these provisions, such inconsistent terms and conditions shall be of no force and effect. This document, including the CCC Billing and Payment Terms and Conditions, shall be the entire agreement between the parties relating to the subject matter hereof.

This Agreement shall be governed by and construed in accordance with the laws of the State of New York. Both parties hereby submit to the jurisdiction of the courts of New York County for purposes of resolving any disputes that may arise hereunder.

**If you would like to pay for this license now, please remit this license along with your payment made payable to "COPYRIGHT CLEARANCE CENTER" otherwise you will be invoiced within 48 hours of the license date. Payment should be in the form of a check or money order referencing your account number and this invoice number RLNK500807899.**

**Once you receive your invoice for this order, you may pay your invoice by credit card. Please follow instructions provided at that time.**

**Make Payment To:  
Copyright Clearance Center  
Dept 001  
P.O. Box 843006  
Boston, MA 02284-3006**

**For suggestions or comments regarding this order, contact RightsLink Customer Support: [customer@copyright.com](mailto:customer@copyright.com) or +1-877-622-5543 (toll free in the US) or +1-978-646-2777.**

**Gratis licenses (referencing \$0 in the Total field) are free. Please retain this printable license for your reference. No payment is required.**